Chapter 5
Hierarchical self-assembly

In the previous chapter, the assembled structures are of first-order in the sense that their morphology is mainly determined by the length scale of individual building blocks. Higher-order structures are observed in molecular and biological systems such as rod-coil molecules, liquid crystals and proteins when first-order structures grow into another length scale. For example, stacking polar tilted smectic layers formed by bent-core liquid crystals twist into a chiral superstructure, called the B4 phase. In this chapter, we investigate the hierarchical self-assembly of T-shaped rod-coil molecules, and extend to their nanoscale analogs, namely laterally tethered rods, aiming at designing higher-order structures such as spiral scrolls and helical structures, which have not previously observed in soft matter systems. Notably, these structures are able to reconfigure quickly and robustly in response to the environmental condition, suggesting a host of applications including reconfigurable nanomaterials, nano-actuators, drug delivery and sensors.

5.1 Spiral scrolls

The study in this section was initially performed in collaboration with Lee's group at Yonsei University, Korea and published in Reference [155]. We briefly present the most important experimental findings and the contribution of our simulation study. The simulation model and method is subsequently discussed, followed by the key results and discussion. We show that a bilayer sheet formed by laterally tethered nanorods scrolls into tubular super-structures with a spiral arrangement. By changing the effective interactions between the rods and the tethers, reversible transformations between distinctive spiral morphologies can be induced in a non-conventional way.

5.1.1 Introduction

It is well known that tubular nanostructures acquire a variety of unique mechanical and electro-optical properties that can be utilized in functional nanomaterials, electromagnetic sensors and energy storage. Inspired by recent advances in synthesizing carbon nanotubes, numerous practical approaches have been proposed to achieve control over the fabrication of hollow tubular structures at nanometer scales. For example, molecular building blocks are judiciously tailored such that they are able to stack into hollow cylindrical structures via non-covalent interactions such as hydrogen bonds[[156, 157]. For tubules at greater length scales, recent efforts usually involve rolling up a pre-assembled sheet-like structure under appropriate environmental conditions. In this regard, inorganic crystalline sheets[158–160], bi-metallic thin films[161, 162], assemblies of amphiphilic molecules[163–166], shape amphiphiles[167], block copolymers[168, 169], peptides[170], and lipid membranes[171] are employed as starting materials. Theoretical works have shown that membranes with in-plane anisotropy scroll into a tubular phase[172–178]. Selinger et al. proposed a model membrane of which the free energy functional contains additional terms representing the effects of anisotropic elasticity and molecular chirality[172]. The complex interplay of these two parameters was further shown to play key roles in the transition between helical cylindrical and twisted ribbons[173, 174]. Bowick et al. simulated a tethered triangular lattice membrane with different bending stiffness coefficients in x and y directions and observed a strong transition from a flat sheet to a tubular structure[175]. Liquid crystalline elastomer membranes are also reported to form nematic and SmC tubules, respectively, due to the spontaneous breaking of in-plane isotropy[176, 177]. For solid-state thin films, the tensile imbalance caused by the lattice mismatch between two surfaces is the primary driving force that results in the rolling tendency to minimize the elastic energy[161, 179]. Meanwhile, sheet-like assemblies of amphiphilic molecules, shape amphiphiles and lipid membranes tend to scroll to reduce the exposure of solvophobic areas. Chen and co-workers showed that para-terphenylen-1,4”-ylenebis(dodecanamide) (TB) molecules consisting of a central rigid rod-like terphenylene segment, two secondary amido functional groups, and two flexible alkyl chains, self-assemble into nanosheets by $\pi - \pi$ stacking of terphenylene units and intermolecular hydrogen bonding between amido functional groups[165]. The sheets subsequently roll up to form nanotubes or stack into multi-layered sheets depending on the concentration of TB in tetrahydrofuran (THF). We consider these tubular structures higher-order assemblies because their characteristic dimensions, i.e. length and radius, are much greater than the dimension of assembling molecules.

Even more interesting is the ability of these hierarchically assembled structures to reconfigure in response to changes in temperature, pH or light. For instance, Lee et al. showed

that hepta-(p-phenylene) rods grafted by hydrophilic oligoether dendrons and hydrophobic branched heptyl chains at opposite midpoints in a selective solvent assemble into a bilayer sheet coated with the hydrophilic tethers[166]. The bilayer sheet, within which the rod segments pack into a nematic order, scrolls into a tubular structure upon heating, and reverts to a flat state upon cooling reversibly. This was attributed to the oligoether chains being dehydrated above and hydrated below the lower critical solution temperature (LCST), respectively. Giulieri and coworkers demonstrated that single-chain fluorinated amphiphiles derived from dimorpholinophosphate assemble into different hollow tubular bilayer-based morphologies when dispersed in water, ethanol/water mixtures and dimethylformamide[163]. The hollow tubules transform reversibly into vesicles upon heating or flattened tubules upon aging depending on the solvent condition and components. Lim et al. proposed a model actuator made from the self-assembly of gold-polypyrole nanorods. In their work, a sheet formed by gold-polypyrole nanorods converts was shown to adopt different bending curvatures in response to changes in humidity, temperature and light due to the expansion and contraction of the polypyrole segments. The whole structure then acts like an actuator with a controllable opening/closing motion[167].

5.1.2 Self-assembly of T-shaped rod-coil molecules

In 2009, Hong and coworkers studied the self-assembly of T-shaped rod-coil molecules in bulk, reporting the formation of two types of tubular structures with different morphologies (Figure 5.1).[1] The rod-coil molecules under consideration are composed of a penta-p-phenylene conjugated rod with a poly(propylene oxide) (PPO) coil laterally attached through an imidazole linkage (Figure 5.1(a)). Rod-coil molecules based on a lateral chain are known to self-assemble into bilayer structures[18, 48]. The stiff rod layers are separated by the amorphous layers of the lateral coils. Within the layers, the local packing of the rods is ordered in a P_2 symmetry or disordered depending on the coil length. More interestingly, the authors observed that the layered structures after assembled continue to roll up into tubules with a diameter of 80-100nm (Figure 5.1(c-d)).

Rod-coil molecules **1** and **2**, and their analogues **3** and **4** with longer PPO chains, show an ordered state. Small angle X-ray scattering reveals that **1** and **2** assemble into a layered structure with a primary spacing of 3.5 and 4.6 nm, respectively. These dimensions correspond roughly to the laterally extended coil length in **1** and **2**, respectively, suggesting that

[1]This section is adapted from Reference [155] D.-J. Hong, E. Lee, H. Jeong, J. Lee, W.-C. Zin, T. D. Nguyen, S. C. Glotzer, M. Lee, Solid state scrolls from hierarchical self-assembly of T-shaped rod-coil molecules, *Angewandte Chemie International Edition*, 48, 9, 1664, 2008.

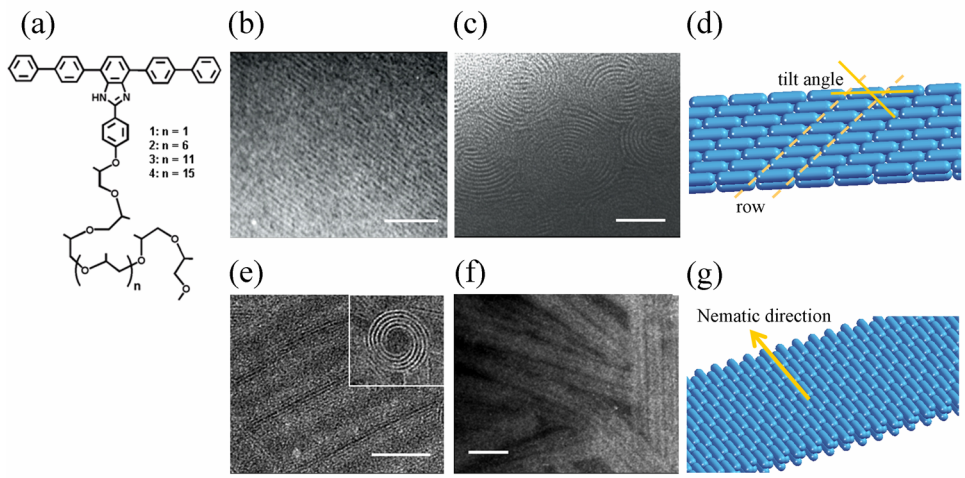

Figure 5.1 Experimental results produced by Lee group. (a) Molecular structure of molecules **1**, **2**, **3** and **4**. (b-c) TEM micrographs of the tubular structures formed by **2**. (b) The image of a layered structure confined in the scrolls, revealing an ordered array of alternating light colored PPO layers and dark aromatic layers. (d) Illustration of a bilayer sheet formed by **1** and **2** showing a P_2 packing with rows (or sublayers as defined in Reference [129]) and the tilt angle of rods within a row. (c) The cross-sectional image along the scrolled lamellar sheet axis. (e-f) TEM micrographs of the tubular structures formed by **3**. (e) A side-view snapshot shows the multilayered structure with an interlayer distance of the tube wall of about 6.2nm. The cross-sectional image shows scrolls with a spiral arrangement (inset). (f) The image of solution-cast thin film of **3** negatively stained with uranyl acetate solution shows well-ordered tubular structures. Scale bars in (b-c) are 50nm, in (e-f) are 100nm. (g) Illustration of a bilayer sheet formed by **3** and **4** with the nematic direction of the rods.

the rod segments within the domains are parallel to the layer planes. The existence of a sharp peak in the scattering pattern at an intermediate angle suggests that the rod segments in **1** and **2** organize into rows with a height of 1.76 nm within a layer. Considering the calculated rod length of 2.2 nm, this dimension indicates that within each row the rods are tilted at an angle of 37°. In contrast to conventional layered structures, the layered structure here form scrolls with a nearly uniform diameter, as revealed by the transmission electron microscopy (TEM) images in Figure 5.1(b-c). The cross-section view reveals the formation of scrolls with a spiral arrangement of alternating light coil and dark rod layers with scroll diameters ranging from 80 to 100 nm (Figure 5.1(c)). Additional information on the structural dimensionality was obtained by 2-D X-ray diffraction with an annealed sample of **2** exhibiting macroscopic orientation. The local packing of the molecules within the assembled structures is revealed by X-ray beams directed perpendicular to the principle axes of the scrolls. The results at intermediate and wide angles suggested that the rod segments crystallize into a P_2 pattern and that the sheet folds along the separation between rows (Figure 5.1(d)).

Rod-coil molecules **3** and **4** with longer PPO chains also self-organize into a layered structure (Figure 5.1(d-e)). The small-angle X-ray diffraction shows three sharp equidistant

reflections, indicative of a layered structure with a lattice constant of 6.2 and 7.2 nm for **3** and **4**, respectively. These dimensions suggest that the layer structure arises due to segregation of the lateral PPO chains from the stiff aromatic segments. Within the layers, the rod segments are again organized within the layer planes. The lower transition temperatures together with smaller enthalpy changes compared to those of their analogues with a short PPO chain indicate that the rod segments within the layers of **3** and **4** are aligned with overall less order than **1** and **2**. The existence of a sharp peak in the diffraction pattern at an intermediate angle suggests that the rod segments in both molecules organize into rows with a height of 1.52 nm. Considering the calculated rod length of 2.2 nm, this dimension indicates that the rods tilt at an angle of 47°, suggesting that the rows interleave (Figure 5.1(g)).

Using a coarse grained model and Brownian dynamics simulations, we have shown that the key factor that leads to the formation of these tubular structures is the bulkiness of the coils. As the coil length increases, the attractive van der Waals interaction between the coils becomes stronger, so does the excluded volume interaction between them. For the molecules with a short coil (**1** and **2**) the coil-coil attraction dominates, causing the bilayer sheet fold on itself, leading to a tubular structure with a filled core. Additionally, since the rod segments are energetically favored to maintain their side-by-side contacts within a P_2-like crystalline packing, the sheet can only fold along the separation between the sublayers, as observed in experiments. For the molecules with a longer coil (**3** and **4**), the excluded volume interaction between the coils becomes more pronounced, preventing the folding sheet from collapsing in the core of the tubular structure. Because the longer chains compete for more free volume by lowering the grafting density of the anchoring points on the bilayer sheet, the rods are shifted along their long axis into a nematic-like ordering. As such, the most energetically favorable direction for the sheet to scroll is along the nematic direction of the rods.

These fascinating results inspire us to extend our simulation model by investigating other possibilities to assembling super-structures from hierarchical assembly. We demonstrate that by varying effective interaction schemes between the rod segments and the flexible tethers a bilayer sheet pre-assembled by laterally tethered rods can form spiral scrolls[180] and helical structures[76], neither of which has been reported for soft matter systems.

5.1.3 Model and simulation method

Model

We start with a minimal coarse-grained model of laterally-tethered nanorods similar to that used in Reference [18]. The rods consist of $N_R = 5$ spherical beads with diameter σ placed

at a center-center distance of σ. The center bead is linked with the tether via a finitely extensible nonlinear elastic (FENE) spring. The tethers are modeled as linear chains of N_T spherical beads with diameter σ, bonded via FENE springs. Unlike in Reference [18], here we combine the rods into rigid pairs and connect them with FENE springs to create a flexible bilayer (Figure 5.2(b)). The motivation for us to bind the rods permanently by spring is due to several reasons. First, the rod segments are always energetically favored to pack side by side to maximize their contacts, and if necessary, shift along their axial direction to allow the tethers to gain additional conformational entropy[18]. Second, experiments have shown that once the sheets are formed, they remain under scrolling both in solution[165, 166] and in the bulk state[129], suggesting that the rod binding is sufficiently stronger than solvophobic forces to sustain the sheet under different solvent conditions[129, 165, 166]. And finally, using springs allows for the local re-organization of the rods in the presence of thermal fluctuations and the excluded volume interaction between the tethers. Or in other words, the entropic effects of the tethers can be incorporated into the local packing of the rods by means of the bonds. This bonding scheme has been successful in reproducing the behavior of the bilayer sheets formed by T-shaped rod-coil molecules in Reference [129]. We infer from experiments that even when the coil length is the same on both sides of the sheet, there should be a sufficiently strong tension imbalance (as compared to thermal fluctuations) to initiate the scrolling process. Without any loss in generality, we choose different tether lengths on each surface of the sheet to mimic this imbalance: the longer tethers on one surface consist of two beads ($N_T = 2$) unless stated otherwise, and the shorter tethers on the other surface consist of one bead.

We utilize empirical potentials that are successful in capturing the relevant physics of block copolymers, surfactants and colloidal particles to model the effective interaction between species. To model the aggregation of a species (i.e. rods or tethers), for example, when the solvent is poor for that species, the attraction between the beads of that species is modeled by the Lennard-Jones potential, which incorporates the short-range attraction and excluded volume interactions. For species that does not aggregate, for example, when the solvent is good for that species, the interaction between the beads of that species is modeled by the repulsive Weeks-Chandler-Andersen (WCA) potential. The interaction between the rods and the tethers is always modeled by the WCA potential to represent their immiscibility. In our simulations, the potential energy well depths are chosen to be identical for rod-rod, tether-tether and rod-tether interactions $\varepsilon_{NP-NP} = \varepsilon_{NP-T} = \varepsilon_{T-T} = \varepsilon$. The natural units for these systems are the diameter of a bead, σ, the mass of a bead, m, and the Lennard-Jones well depth, ε. The time scale is defined as $\tau = \sigma\sqrt{m/\varepsilon}$ and the dimensionless temperature is $T^* = k_B T/\varepsilon$.

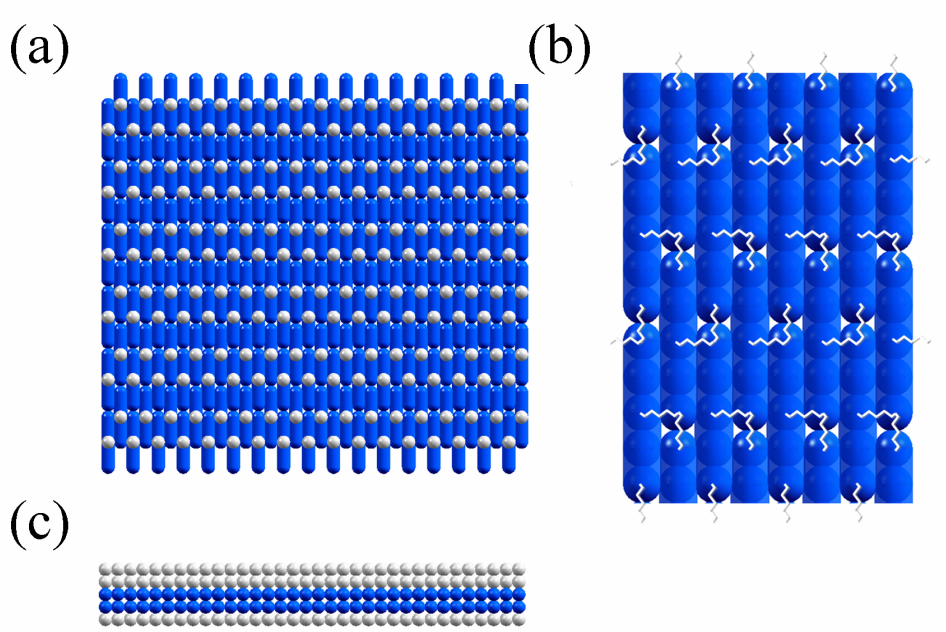

Figure 5.2 Model bilayer sheet: (a) Side-view; Rods are in blue and tethers are in gray. (b) Bonding scheme with springs in white color. Tethers are not visualized. (c) Top-view

Simulation method

We use molecular dynamics with the Nose-Hoover thermostat chains to simulate the bilayer sheet in the NVT ensemble. The rotational degrees of freedom of the rod pairs are incorporated using the equations for rotation of rigid bodies with quaternions. The rigid body motion in the NVT ensemble is updated by the symplectic time-reversible integrator[86]. Using Nose-Hoover thermostats allows us to incorporate hydrodynamic interactions into the motion of the particles, and thus to sample the dynamics of the system. The equation of motion of the tether beads and the rod pairs are integrated by the velocity Verlet scheme with a time step $\Delta t = 0.002\tau$. The sheets are initialized at their most stretched configuration in a large simulation box of which all the dimensions exceed the length of the sheets and equilibrated at constant temperature. For each interaction scheme and sheet aspect ratio we run several independent simulations with different random number seeds to ascertain that the final structures are reproducible. Final structures are determined by observing fluctuations in the system potential energy of less than 5% and a morphology that does not substantially change over a time scale of $\approx 50 \times 10^6$ time steps which exceeds the relaxation time at equilibrium. We investigate the model bilayer sheets with the length:width ratios of 100:4, 120:4, 140:4, 180:4, and 200:4, measured in rod pairs. Test simulations on sheets with greater widths, that is, 100:8 and 140:16, show that the morphologies are invariant with the sheet width. Our simulations are conducted using LAMMPS, an open source parallel

molecular dynamics code[71]. We have contributed in part to the implementation of the rigid body integrator using the Nose-Hoover thermostat chains in LAMMPS.

5.1.4 Results and discussion

The driving force for the bending of the bilayer sheet is the net difference between the attractive forces coming from both sides of the sheet[172, 178]. Beyond that, the effective interaction between the rods and the species determines the geometrical properties such as the core diameter and the spacing between adjacent turns. Our supplementary simulations indicate that these geometrical parameters are almost invariant with the width and length of the sheet under consideration. For cases A and B, where the scrolls have an empty core, we investigate the variation of the interior radius and spacing between turns with respect to temperature and the length of the longer tethers on one side of the sheet.

Table 5.1 Geometry parameters of spiral scrolls in studied solvent conditions. Standard deviations are obtained from 10 independent measurements

Case	Effective interactions	Core diameter, σ	Turning spacing, σ
A	R-R attractive T-T non-attractive	8.36 ± 0.85	6.9 ± 1.51
B	R-R attractive T-T attractive	7.67 ± 0.79	4.2 ± 1.09
C	R-R non-attractive T-T attractive	4.4 ± 0.47	3.4 ± 0.48

The evolution of the flat sheet into spiral scrolls is characterized by the average maximum cylindrical curvature of the sheet defined as:

$$\bar{C} = \frac{1}{n} \sum_{i=1}^{n} C_i \tag{5.1}$$

where C_i is the local curvature at each point on the sheet centerline; n is the number of points in the innermost turn. The maximum curvature varies from zero for a flat sheet to a nonzero value corresponding to the innermost turn of the spiral scroll. Since the curvature of the sheet monotonously decreases from the scroll center, the core diameter is related to the maximum curvature by $D = 2/\bar{C}$. Table 5.1 shows the geometrical properties of the scrolls in all the cases studied at $T^* = 2.5$.

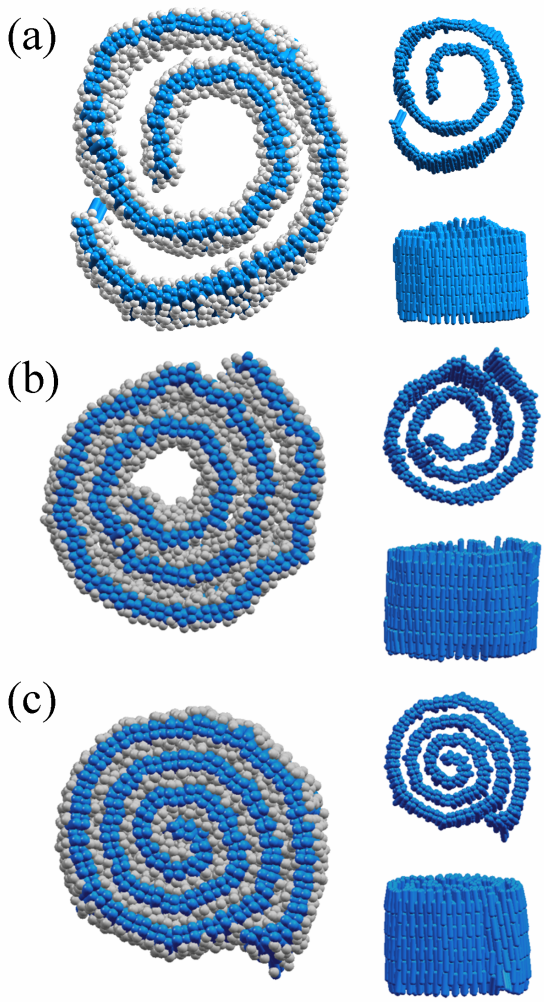

Figure 5.3 Spiral scrolls formed in three cases listed in Table 5.1. Left: Top-view. Right: top-view and side-view with tethers not shown. (a) Case A; (b) Case B; (c) Case C.

Case A: R-R attractive and T-T non-attractive

This effective interaction scheme is equivalent to the case in which the tethered rods are in a selective solvent that is poor for the rods but good for the tethers. The sheet forms into a spiral scroll with an empty core and multiple loose turns (Figure 5.3(a)). With the interaction range of 2.5σ, the attraction between the rods allows the sheet to bend toward the surface where the rods are connected via springs. In this case, the presence of the springs on one side of the sheet mimics and, to some extent, amplifies the net imbalance in the surface tension due to the effects of thermal noises that disturb the flat configuration. This is in agreement with recent experiments on rolled-up flat sheets with equivalent surfaces under thermal fluctuations[166]. The curvature of the sheet in this case is the smallest as compared to the previous cases because of the lack of the attraction between the tethers and

the collective attraction between the rods on two surfaces of the sheet.

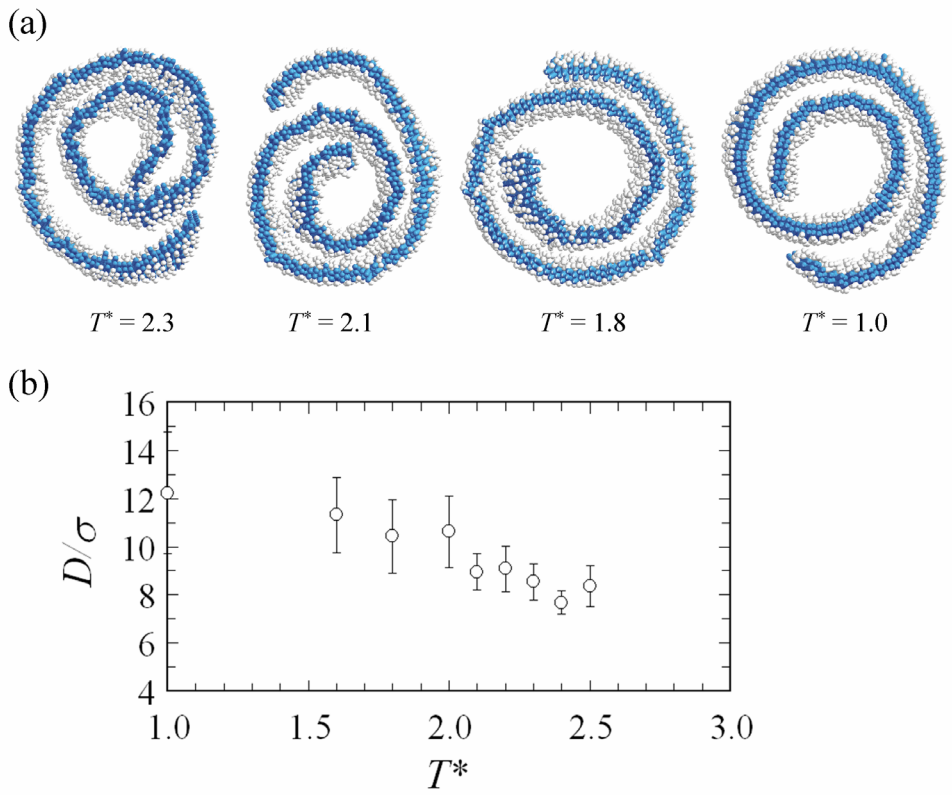

Figure 5.4 Spiral scrolls formed when R-R are attractive and T-T non-attractive (Case A) for $N_T = 2$. (a) Representative snapshots at different temperatures. (b) Core diameter as a function of temperature. Error bars are obtained from the distribution of the curvatures measured at the innermost turn at each temperature.

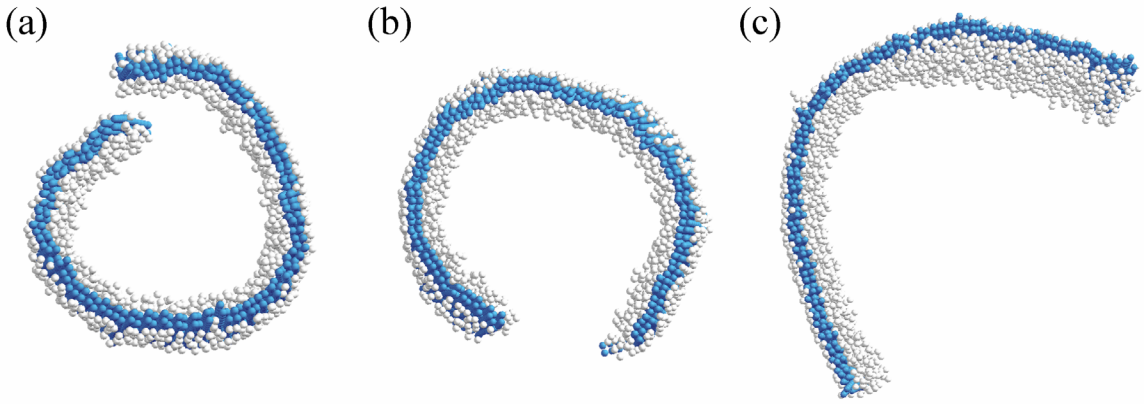

Figure 5.5 Resulting structures with different tether lengths when R-R are attractive and T-T non-attractive (Case A): (a) $N_T = 4$, (b) $N_T = 5$ and (c) $N_T = 6$.

The core diameter is dependent upon temperature as shown in Figure 5.4. As temperature increases, the effective attraction strength between the rods decreases and the maximum

curvature occurring at the inner turns tends to be lowered. However, the relative change in the core diameter in respond to temperature is not significant given large fluctuations large at low temperatures (Figure 5.4(b)). This is because the difference between the attractions coming from the longer tethers on one side and from the rods on the other side does not change noticeably with temperature.

We also vary the tether length on one side of the sheet and observe that the exclude volume interaction between the tethers strongly influences the bending of the sheet. The longer the tethers get, the stronger they straighten out the sheet, reducing the maximum curvature and opening the scroll. This trend suggests that if the polymeric tethers can be adjusted upon a change in the environment, e.g. via temperature or pH, the scroll would mimic an open-close motion, which can be utilized in drug delivery and biosensing. This is consistent with the findings reported in Reference [166] where the bilayer sheet of rod-coil molecules folds/unfolds upon heating and cooling. We note that the response of the sheet to the changes in the tether length also resembles the behavior of the micron-sized biphasic rods where one of the compartments shrinks or expands as temperature is decreased or increased, respectively.

Case B: R-R attractive and T-T attractive

The effective interactions between the rods and the tethers in this case resemble those in a neat system or in the bulk state[24]. The tethers attempt to increase their contacts to minimize the system potential energy, causing the sheet to curve toward the side with longer tethers. However, since the rods also try to maximize their side-by-side contacts, their attraction coming from both sides offsets the bending effects due to the longer tethers. The adopted curvature of the sheet is therefore greater than that in the previous case where the tethers are non-attractive. At the center of the scroll, both the tether excluded volume and the competing attraction of the rods from the other surface prevent the sheet from being further tightened. Consequently, the sheet forms a spiral scroll with an empty core and multiple tight turns (Figure 5.3(b)). The distance between adjacent turns is smaller than that in the previous case, due to the attraction between the tethers coming from both surfaces.

The formation of the spiral structure is shown in Figure 5.6. It is interesting to note that the sheet first curves from both ends, forming two scrolls with opposite directions. The presence of two scrolls is unstable and one of the scrolls, numbered as (1) in Figure 5.6, becomes dominant and unfolds the other (2). The dominating scroll is the one that acquires the maximum curvature in the inner turn faster than the other at the earlier stage (e.g. at $t = 10^6\tau$ in Figure 5.6). The same dynamics is observed from other simulation runs with

different initial conditions, suggesting that one spiral scroll is a stable state of the sheet.

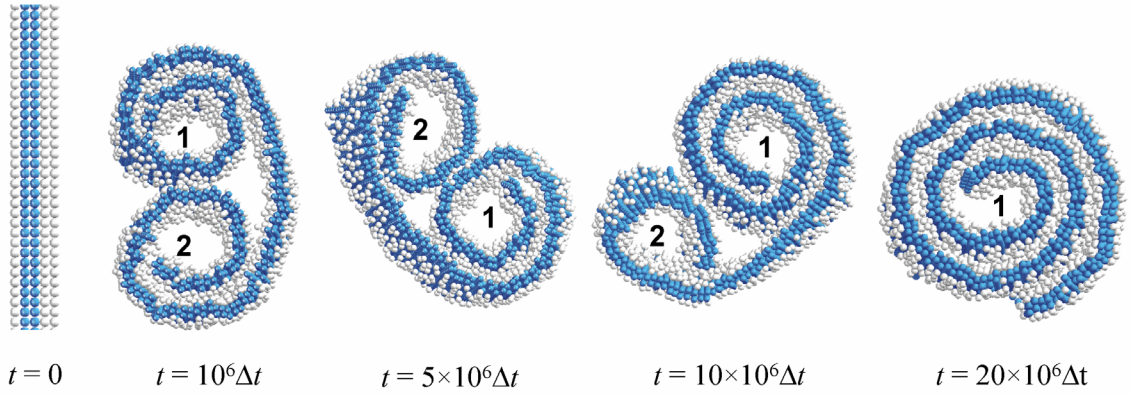

Figure 5.6 Time evolution of the bilayer sheet in Case B when R-R are attractive and T-T attractive for $N_T = 2$ at $T^* = 2.5$. The scrolls are distinguished by their indices to recognize their time evolution.

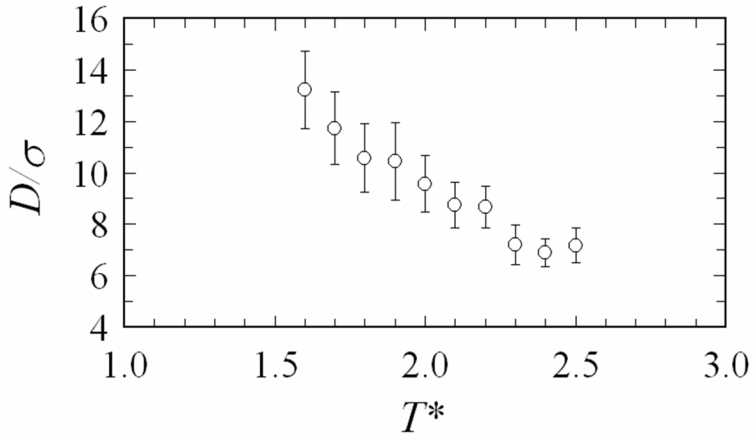

Figure 5.7 Core diameter of spiral scrolls formed when R-R are attractive and T-T attractive for $N_T = 2$ as a function of temperature. Error bars are obtained from the distribution of the curvatures measured at the innermost turn at each temperature.

As shown in Figure 5.7, the dependence of the core diameter on temperature is more noticeable than that in Case A (cf. Figure 5.4(b)). When the tether length is increased, the core diameter increases because of the packing frustration of the tethers (Figure 5.8). However, since the attraction between the tethers also increases, the maximum curvature of the scrolls is greater than those obtained in Case A given the same tether length.

Case C: R-R non-attractive and T-T attractive

The tethers attempt to increase their contacts to minimize the system potential energy, causing the sheet to curve toward the side with longer tethers. Since the rods are non-attractive, the difference in the attraction of the tethers from two surfaces in the primary driving force

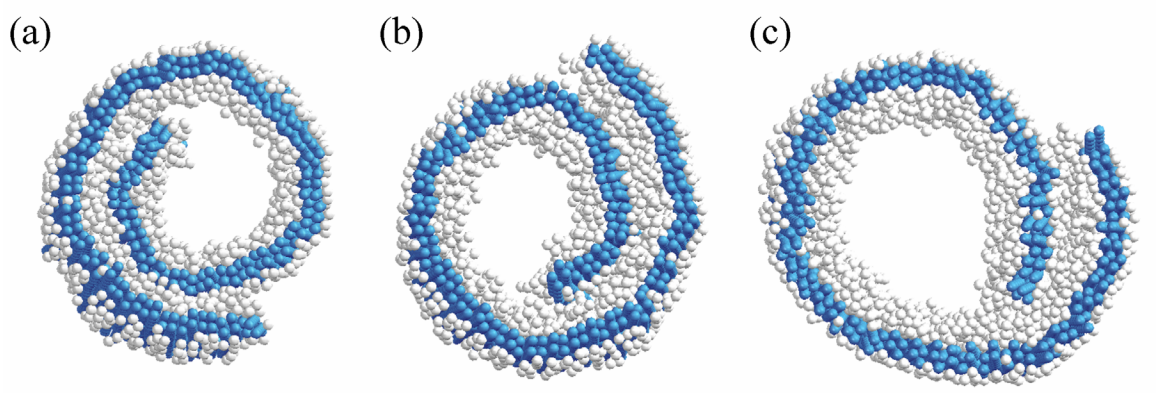

Figure 5.8 Resulting structures with different tether lengths when R-R are attractive and T-T attractive: (a) $N_T = 4$, (b) $N_T = 5$ and (c) $N_T = 6$.

that bends the sheet. As a result, the sheet can adopt the maximum curvature at the center of the scroll until the packing frustration of the tethers dominates. The core diameter is approximately twice the tether length $(4.4\pm0.47)\sigma$. The tethers between adjacent turns also attract each other; therefore, there is no gap between turns and the spacing is approximate the total length of the tethers from two surfaces $(3.4\pm0.48)\sigma$. The sheet then forms a spiral scroll with a filled core with multiple tight turns (Figure 5.3(c)).

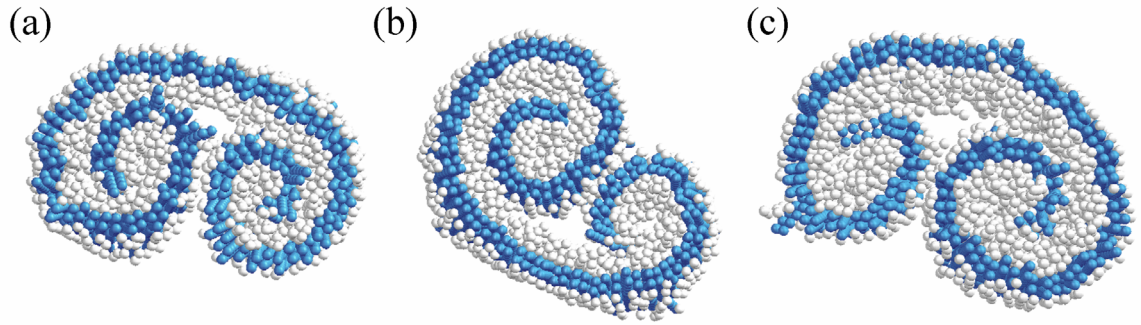

Figure 5.9 Resulting structures with different tether lengths when R-R are non-attractive and T-T attractive: (a) $N_T = 4$, (b) $N_T = 5$ and (c) $N_T = 6$.

The sheet curves from both ends and two spiral scrolls with opposite directions meet at the middle of the sheet (Figure 5.9). Similar to the previous cases, the core diameter increases with the excluded volume of the tethers. Because there is no competing force from the rods, the attraction of the tethers in the core, which is much stronger than thermal fluctuations, prevents the two spiral scrolls from merging into one. These are kinetically trapped configurations with a higher potential energy than the energy minimizing structure shown in Figure 5.3(c). An approach to help the structure escape from the kinetic traps and reach the energy minimum is to start from the stable, energy minimizing morphology

obtained in Case B and switch the effective interaction between the rods to non-attractive. Such interaction-switching induced transformation will be discussed below.

Reversible transformation

Interestingly, we observe that when the effective interaction scheme is toggled from one to another, the spiral scrolls transform accordingly. Instead of initializing the sheet at the flat morphology, we start with an equilibrated spiral scroll under a specific condition, and subsequently switch to using other effective interactions between the rods and the tethers. The scroll spontaneously responds to the environmental change and transforms to the corresponding morphology. The duration to complete the transformation is in the order of 10^6 time steps, which is remarkably faster than that required when starting from the flat sheet (see Figure 5.6). Of practical importance is that the transformation processes between the morphologies are reversible, suggesting that the scrolls are at equilibrium in each interaction scenario. This striking feature enables the application of nano-actuators or nano-springs in which the nanostructures are able to reconfigure in a controllable way.

The reversible transformation between the spiral scrolls suggests the pathways between hierarchically assembled structures, allowing for achieving energy minimizing structures without kinetic traps. Starting from the scroll obtained from Case B (Figure 5.3(b)), we switch the rod-rod interaction from attractive via the Lennard-Jones potential to non-attractive via a Weeks-Chandler-Andersen potential while keeping the tether-tether interaction attractive. The interaction scheme is now switched to Case C. The scroll tightens such that the core is filled with the tethers as shown in Figure 5.3(c). As discussed earlier, by doing this, the resulted scroll ends up with an energy minimizing configuration, which is inaccessible if starting from a flat configuration. When the rod-rod interaction is reverted, the spiral scroll recovers the empty core as in Figure 5.3(b). Similar reversible transformation can be induced between the scrolls formed in Case A and Case B and between those in Case A and Case C. While the switching between Case A and Case B adjusts the gap between turns, the switching between Case A and Case C opens and closes the core. These morphological changes are potentially applicable to microfluidic devices, nano-filtration, and drug delivery.

5.1.5 Conclusion

We have shown that bilayer sheets formed by nanorods attached by a flexible chain at its middle point scroll into spiral tubular structures. It is the liquid crystalline packing of the rods

determined by the tether bulkiness that governs the scrolling axis of the sheet. Depending on the effective interaction between the rods and the tethers, the resulting scrolls have different geometrical properties. Temperature and tether length are also influential factors that control the bending ability of the sheet. One key finding is the ability of the scrolls to reconfigure under a switch in the species interaction, allowing for a change in their macroscopic properties. This reconfigurability allows for establishing non-conventional, kinetic traps-free pathways connecting super-structures that are not directly available from self-assembly. Our findings suggest that hollow one-dimensional nanostructures, which might have been shown to have interesting optical and mechanical properties, can be assembled from the self-assembly of nano-building blocks across multiple length scales, and that the reconfigurability of such structures can be achieved via a simple change in the environment. In the following section, we will show a similar behavior of another hierarchically assembled structure from laterally tethered rods with a different rod packing pattern that form distinct helical superstructures.

5.2 Helical structures

We show that a model bilayer sheet assembled by laterally-tethered nanorods fold into distinct helical morphologies at moderate temperatures under different solvent selectivity conditions. The crystalline packing of the rod segments in the sheet plays a vital role in guiding the scrolling direction of the sheet. Similar to spiral scrolls reported in the previous section, the helical structures can also reversibly transform from one morphology to another by toggling the solvent condition. This model serves both to inspire the fabrication of laterally tethered nanorods for assembling helices at nanometer scales and as a proof-of-concept for engineering switchable nanomaterials via hierarchical self-assembly.[2]

5.2.1 Introduction

Fabrication of functional structures at nanometer and micrometer scales using bottom-up techniques such as directed- and self-assembly has gained increasing interest among the materials community in recent years. A popular approach to engineering a target structure involves designing building blocks such that their anisotropic interactions give rise to the desired microphase separation and local packing. Toward this end, shape molecules [131], block copolymers[181], amphiphilic peptides[170] and DNA- and polymer-functionalized

[2]This section is adapted from Reference [76] T. D. Nguyen, S. C. Glotzer, Switchable helices formed by hierarchical self-assembly of laterally tethered nanorods, *Small*, 5, 18, 2092-2096, 2009.

nanoparticles[5, 182–184] are popular building blocks in engineering ordered, functional nanostructures. However, it is challenging to control the self-assembly of many building blocks into higher-ordered structures from isotropic states because the system may become easily trapped in deep energy minima. A promising solution to help overcome this obstacle is to guide the assembly path by preparing intermediate pre-assembled patterns such that they can naturally fold into target structures[8, 165, 185]. With this approach the final structures are no longer limited to classical surfactant-based morphologies, but can be more diverse in shape and scale. For example, Ciszek et al. demonstrated that assemblies of amphiphilic gold-polypyrrole nanorods on intentionally designed two-dimensional footprints, when released from the template, can form various desired higher-ordered structures including hemispheres, open spheres and capsules at the same environmental conditions[8]. Recent computational and experimental studies have shown that laterally-tethered nanorods in selective solvents[18] and T-shaped rod-coil molecules in the melt[129] self-assemble into bilayer sheets of P_2 symmetry in which the rod segments are organized into crystalline, in-plane sublayers. The bilayer sheets subsequently scroll into spiral multilayered tubules with an outer diameter of $\approx$ 100nm under melt conditions[129].

Helical structures are commonly found at molecular scales. Examples include natural biological molecules and synthetic polymers. However, little progress has been made to control the formation of helical structures at mesoscopic scales. It has been shown that helical structures spontaneously appear in chain-like molecules most likely because of the presence of directional hydrogen bonds at proper positions[186–188]. More importantly, the formation of local hydrogen bonds, i.e. between neighboring monomers, should be faster and more favorable than non-local bonds[189]. Discrete building blocks can also form helices if their interactions are sufficiently anisotropic that a helical arrangement is the most energetically favored[156, 190]. Most attempts to date require decorating molecular building blocks with sticky or polar patches to induce directional non-covalent bonds[156, 170] or introducing lateral substituents at some specific positions on chain-like supramolecules to help guide the folding process[186, 191]. The assembled helical structures are static in the sense that we cannot dynamically tune their geometrical parameters, e.g. radius and pitch, once they are formed. For nanoparticle and colloidal systems, despite the increasingly expanded library of anisotropic building blocks[25], there have been few reported to self-assemble into helices. For instance, Yin et al. reported that spherical colloids can assemble into helices with predefined handedness in V-shaped grooves by means of capillary forces[192]. Price et al. proposed a method for fabricating metal helical nanostructures using a phospholipid microtubule template coated by oppositely charged polyelectrolytes in which the metal nanoparticles are electrostatically bound to the helical template through a

negatively charged catalyst[193]. Vanapalli and coworkers introduced a method for active assembly of spherical particles into a zigzag morphology a two dimensional helix in confined rectilinear microchannels[126].

Herein we propose an alternative to assemble nanoscale helical structures from experimentally available building blocks, i.e. laterally-tethered nanorods and their analogs, without any confinement. We demonstrate the formation of three distinct helices that differ in pitch and radius from sheets assembled by laterally-tethered nanorods depending on the solvent selectivity. Moreover, we show that the helices spontaneously transform from one stable helix to another when the solvent condition is dynamically changed. Specifically, when a solvent that is poor for rods is switched from good to poor for tethers and vice versa while maintaining solvent-rod immiscibility, the helices transform accordingly from one morphology to another. A similar phenomenon is observed when we change a solvent that is good for tethers from good to poor for rods while maintaining solvent-tether miscibility. When a solvent that is poor for tethers is switched from good to poor for rods, we also observe an expected change in the helix morphology, but the reverse transformation is prohibited, requiring an intermediate state.

5.2.2 Model and simulation method

Model

We use a minimal model of laterally-tethered nanorods similar to one used in our previous work[18, 129]. An example of a model bilayer sheet is shown in Figures 5.10(a-b). The rods consist of three spherical beads with diameter σ placed at a distance σ apart. The center bead is linked with the coil via a finitely extensible nonlinear elastic (FENE) spring[124]. The tethers are modeled as linear chains of spherical beads with diameter σ, bonded via FENE springs. We combine the rods into rigid pairs, and subsequently, connect them with FENE springs to create a permanent and flexible bilayer. The rod pairs are arranged into a P_2 symmetry packing with parallel sublayers as in References [18, 129] and the tethers extend out of the sheet surface. We use a bonding scheme illustrated in Figure 5.10(c) to maintain the sublayers during a simulation run. The bonds connecting rods in the same sublayers represent the side-to-side attraction between the rods within sublayers, and those connecting rod ends represent the end-to-end attraction between the rods from different sublayers. For laterally-tethered nanorods and their molecular analogs, e.g. T-shaped rod-coil molecules, the crystalline ordering of the rods within sublayers is favored over other arrangements because both the rod contacts and the free volume of the lateral tethers are maximized.

Experiments have shown that once the sheets are formed, they are well-maintained under scrolling[129]. We hypothesize that the rod binding is much stronger than solvophilic forces, and hence can sustain the sheets under different solvent conditions. The bonds are therefore introduced to mimic the P_2 symmetry packing of the rods and to retain the sheets during simulations while taking into account thermal fluctuations. This bonding scheme has been used to successfully reproduce the behavior of the bilayer sheets formed by T-shaped rod-coil molecules [129]. We therefore surmise that our model is valid as long as the local short-ranged attractions between the rod pairs are sufficiently strong to maintain the sublayers with a certain freedom of the rods within.

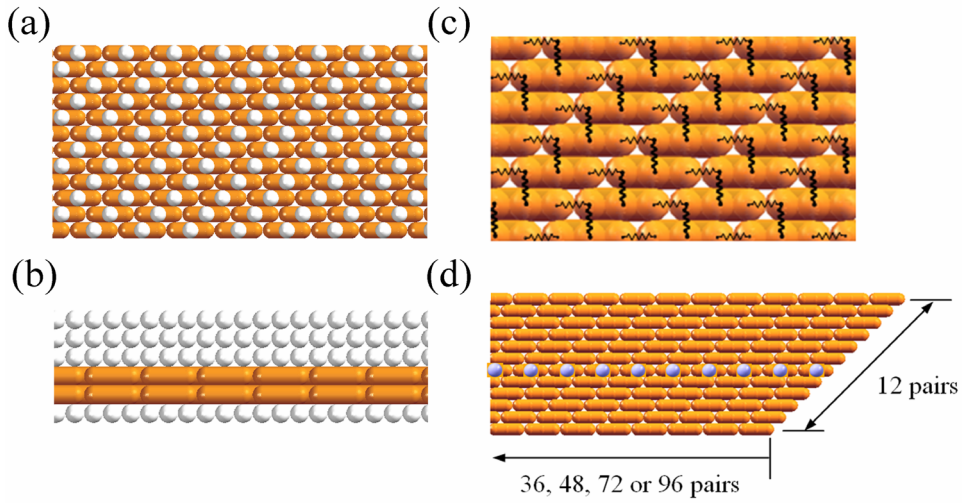

Figure 5.10 A portion of the model bilayer sheet used for the simulations. (a) Side view. (b) Top view: the rods in a pair are rigidly grouped. Longer tethers consist of three beads. (c) Bonding scheme: only the rods in the bottom layer in (b) are bonded. (d) The backbone of the sheet used for calculating helical order parameter H_4 consists of highlighted spheres. Bold springs represent - interactions. Light springs represent end-to-end attractions. The dimensions of the sheet are measured in rod pairs. The tethers are removed for clarity in (c-d).

To help guide the bending of the sheet toward one side, we choose different tether lengths on each surface of the sheet: the longer tethers on one surface consist of three beads, and the shorter tethers on the other surface consist of one bead. It is important to note that we only bond the rods on the surface with longer tethers; otherwise the sheet cannot bend because of the balance in the stiffness of its two surfaces. This is realistic despite excluded volume arguments because the packing frustration of the longer tethers is reduced by the rod tilt within the P_2 packing of the sublayers. Under each solvent condition, we also run simulations with different lengths of the longer tethers to investigate the dependence of helix geometry on tether bulkiness.

The adjustable environmental conditions include various parameters such as temperature, pressure, ionic strength or pH of the solution and solvent selectivity. Previous simulations

have investigated the effects of thermodynamic parameters, e.g. temperature and pressure, on the phase behavior of tethered nanoparticle systems at different concentrations [18, 33, 34, 129]. In this study, we focus on solvent selectivity because it can be readily controlled by experiments, and more importantly, generalized to other external effects in terms of effective interactions between the species in the system. To take into account the solvent selectivity, we utilize empirical potentials that are successful in capturing the relevant physics of block copolymers, surfactants and colloidal particles[52, 123]. If the solvent is poor for a species aggregation of that species will occur. To model the aggregation, the interaction between the beads of that species is modeled by the 12-6 Lennard-Jones potential truncated and shifted to zero at the cutoff distance of 2.5σ to incorporate the short-range attraction and excluded volume interactions. If the solvent is good for a species, aggregation will not occur, and thus the interaction between the beads of that species is modeled by the softly repulsive Weeks-Chandler-Andersen (WCA) potential capturing only short range repulsion and excluded volume. The interaction between the rods and the tethers is always modeled by the WCA potential to represent their immiscibility. Similar to the previous section, the potential energy well depths are chosen to be identical for rod-rod, tether-tether and rod-tether interactions $\varepsilon_{NP-NP} = \varepsilon_{NP-T} = \varepsilon_{T-T} = \varepsilon$.

Simulation method

We use Brownian dynamics (BD) to simulate the model bilayer sheets in three dimensions. We investigate the model bilayer sheets with aspect ratios 36:12, 48:12, 72:12 and 96:12, measured in rod pairs. The sheets are initialized at their most stretched configuration in a large simulation box of which all the dimensions exceed the length of the sheets, and relaxed for a sufficient number of time steps ($\approx 5 \times 10^6$) under athermal condition in which the interactions between all species are non-attractive. The sheets are subsequently equilibrated with the chosen interactions at constant temperature $T = 1.0\varepsilon/k_B$. For each solvent condition and sheet aspect ratio, we run several independent simulations (with different random number seeds) to ascertain that the final structures are reproducible. Final structures are determined by observing fluctuations in the system potential energy of less than 5% and a morphology that does not substantially change over a time scale of ≈ 50 million time steps which exceeds the relaxation time at equilibrium. Our simulations are conducted using LAMMPS, an open source parallel molecular dynamics code[71]. It takes approximately 8 days to complete $\approx 60 \times 10^6$ time steps for a 96:12 sheet on two dual-core Apple G5 (2.0 GHz, 2 GB RAM) myrinet-connected nodes. All the results presented are for sheets with longer tethers consisting of three beads unless otherwise indicated.

5.2.3 Results

We observe the spontaneous formation of helical structures in all solvent selectivity conditions studied. For a given set of interactions, the bilayer sheets fold into helices with the same chirality, pitch and radius for all investigated aspect ratios. Simulation snapshots (Figure 5.11) reveal that the helical morphology substantially varies with the solvent selectivity. Table 5.2 gives a summary of the geometry of the helices formed in our simulations. The small standard deviations in the pitch and radius relative to the average values indicate well-defined helical structures in all cases.

Table 5.2 Geometric parameters of the helices formed in three solvent conditions. The pitches and radii are averaged over 10 measurements along the backbone of the sheets and aspect ratios. The errors are the standard deviation from the average values

Case	Effective interactions	Core diameter, σ	Radius, σ
A	R-R attractive T-T non-attractive	77.9 ± 0.91	10.2 ± 1.48
B	R-R attractive T-T attractive	34.7 ± 0.82	10.4 ± 0.73
C	R-R non-attractive T-T attractive	20.3 ± 0.51	3.8 ± 0.65

To characterize the helical structures, we use an order parameter that is commonly used to represent the net helical growth in chain-like molecules[194], as defined by:

$$H_4 = \left(\frac{1}{n-2} \sum_{i=2}^{n-3} \mathbf{u}_i \right)^2 \tag{5.2}$$

where $\mathbf{u}_i$ is the unit vector proportion to $(\mathbf{r}_i - \mathbf{r}_{i-1}) \times (\mathbf{r}_{i+1} - \mathbf{r}_i)$, where $\mathbf{r}_i$ is the position of the ith monomer and n is the length of the sheet, measured in rod pairs. Here we define the monomers as the center bead of rods that lie in the center row parallel to the longer edge of the sheet (Figure 5.10(d)). The time evolution of H_4 in different simulation runs illustrated in Figure 5.12 shows the dynamic behavior of helix formation, indicating a noticeably sharp transition to helical states in Case B and Case C. The small absolute value of H_4 in the helical state for Case A is due to the large pitch as compared to the radius of the helix, as illustrated by the backbone shape in Figure 5.11. As shown in Figure 5.13, a typical helix forms spontaneously from curling at the two ends of the sheet. Only one handedness is observed, as imposed by the rod orientation in sublayers. Defects may occur if the sheet length does not match the number of helical turns.

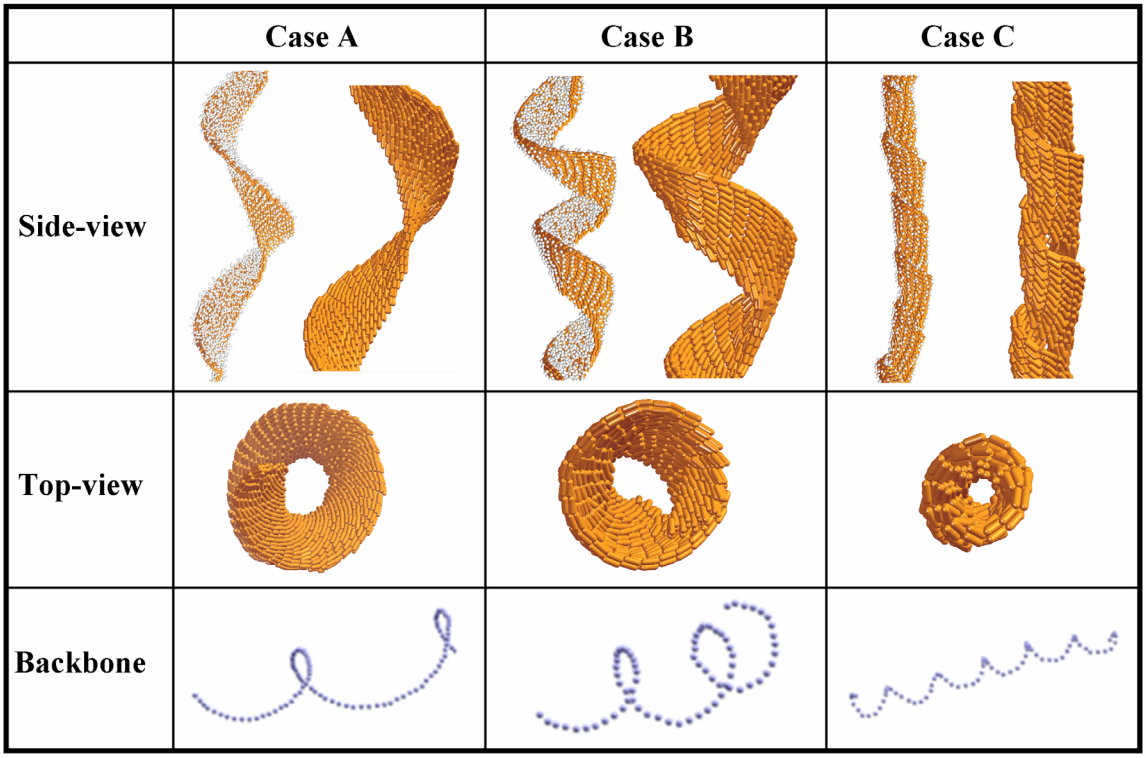

Figure 5.11 Helical structures formed under three solvent conditions, as indicated in Table 5.2. (A) Case A. (B) Case B. (C) Case C. In the zoomed-in side view and top-view image, the tethers are not shown for clarity.

Case A: Solvent good for tethers and poor for rods

When the solvent is good for the tethers and poor for the rods, the rods are attractive to each other while the tethers are not. Previous simulations showed that laterally-tethered nanorods assemble into bilayer sheets under these conditions[18]. When released into a large volume, the sheets spontaneously scroll into helical structures (H_A) as depicted in Figure 5.11. To maximize the free volume of the long tethers on one surface, the sheet bends toward the opposite surface with shorter tethers. Meanwhile, the rod pairs reorient within the sublayers to maximize their contacts and reduce the tether grafting density on both sides of the sheet. The rod pairs close to the center of the helix are nearly parallel to the scrolling axis, aligning with the rod pairs from adjacent sublayers. The sheet forms an open helix with a large pitch as shown in the backbone image in Figure 5.11(left column). These results suggest that we can tune the helix geometry by changing the entropic effects of the tethers through their bulkiness or grafting density. For example, additional simulations demonstrate that if we increase the length of the longer tethers to four, five or six beads, the pitch will increase accordingly while the radius does not change significantly (Table 5.3).

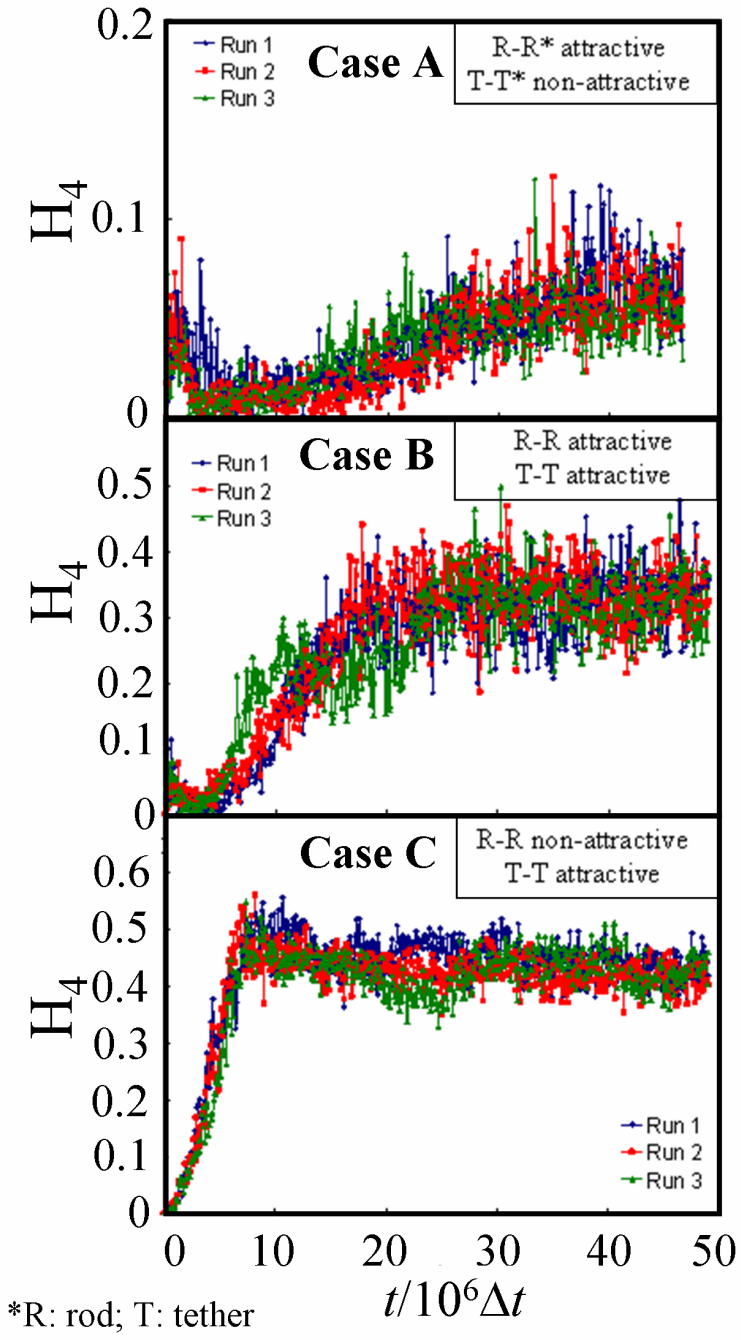

Figure 5.12 Representative time evolution of the helical order parameter H_4 of the backbone of a 72:12 bilayer sheet in three different runs in three solvent conditions.

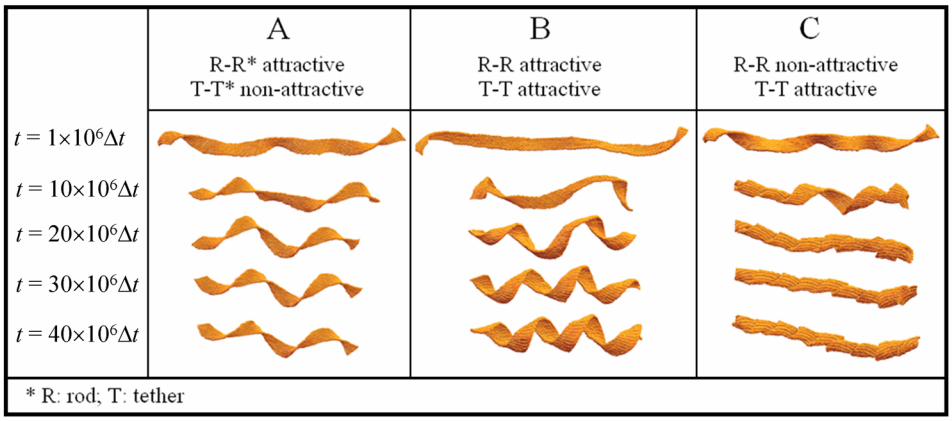

Figure 5.13 An example time evolution of a 96:12 bilayer sheet in three solvent conditions.

Table 5.3 Geometric parameters of the helices formed in three solvent conditions with different longer tether lengths, l_T. The pitches and radii are averaged over 10 measurements along the backbone of the sheets and aspect ratios. The errors are the standard deviation from the average values.

	Case A		Case B		Case C	
l_T, σ	Pitch, σ	Radius, σ	Pitch, σ	Radius, σ	Pitch, σ	Radius, σ
4	84.4±0.42	13.3±0.28	36.6±0.89	10.6±0.84	19.8±0.94	4.8±0.48
5	91.3±0.26	12.5±0.78	30.6±0.39	10.6±0.33	19.1±0.47	5.2±0.39
6	94.8±0.58	12.3±0.83	26.7±0.55	9.9±0.49	19.8±0.41	5.5±0.22

Case B: Solvent poor for tethers and rods

When the solvent is poor for both species, rods attract rods and tethers attract tethers. The interactions between the rods and tethers in this case resemble those in a melt, which result in P_2 symmetry packing of rods within bilayer sheets[129]. In contrast with Case A, the net attraction between the long tethers is larger than that between the shorter ones, favoring the bending of the sheet towards the long tether side. Since bending along the rod direction is highly restricted by the increase in the grafting density of the tethers, the sheet tends to fold along the sublayer directions instead. The sheet therefore curves into a helical structure (H_B) with a smaller pitch as compared to H_A (Figure 5.11, middle column). Moreover, the attraction between the long tethers and the immiscibility between rods and tethers result in the short tethers on the outer surface, consistent with a geometric packing factor analysis[51]. The side view image further shows that the sheet slightly twists to reduce the grafting density of the long tethers. Though the tethers are attractive their aggregation is limited by the strong attraction between the rod pairs, which comes collectively from both sides of the sheet, and by the excluded volume of the long tethers. As a result, the sublayers cannot fold tightly on each other but instead must adopt a curvature that accommodates these competing

forces. Additional simulations show that the radius of the helices is almost invariant as the length of the longer tethers is increased. This indicates that the bending of the sheet is strongly influenced by the net attraction of the rod pairs within the sheet. As the tether length increases, the attraction between longer tethers becomes stronger, pulling the helical turns closer together, and hence reducing the helix pitch (Table 5.3).

Case C: Solvent poor for tethers and good for rods

When the solvent is poor for the tethers and good for the rods, the rods are non-attractive while the tethers are attractive. It should be clarified that this solvent selectivity does not support the self-assembly of sheets from precursor tethered nanorod building blocks, and thus may be considered only after the sheet is already formed, e.g. under either solvent conditions described above. Under these conditions, the sheet then folds tightly into a helical structure (H_C) as shown in Figure 5.11(right column). Similar to Case B, the attraction between the long tethers leads to the folding of the sheet along the sublayer separations. However, since the rod pairs are non-attractive the sheet can bend more tightly as compared to Case B, until densely packed in the interior. Additional simulations reveal that the helical pitch is relatively independent of the tether length and approximates the width of the sheet, whereas the interior radius can be tuned through varying the long tether length (Table 5.3).

5.2.4 Discussion

Of particular importance is the driving force for the spontaneous formation of helical structures in our bilayer sheet model at the initial stage. Sabeur et al. demonstrated that a stretched hydrophobic chain easily falls into a helical state as a local energy minimum if hydrodynamic effects are sufficiently screened[195]. In our simulations, these necessary conditions are fulfilled. First, since the model bilayer sheet is somewhat analogous to a linear but flat homopolymer where the sublayers are sequentially connected via springs it is reasonable that the instability of the initial stretched configuration of the sheet triggers the helix formation. Second, the difference in the tether lengths on the two surfaces drives the sheet to bend and fold toward one side, mimicking the hydrophobic effects in chain-like molecules. Third, hydrodynamics is certainly suppressed in our BD simulation method due to the uncorrelated random forces acting on the beads. Since the helices are reproducibly formed at a much higher temperature ($T = 1.0\varepsilon/k_B$) as compared to homopolymers[195], we argue that the latter condition can be relaxed because at that temperature the system is mainly diffusive, and thus the role of hydrodynamic interactions becomes negligible. It

follows that our simulations can reasonably describe the dynamics of the system without hydrodynamic interactions. The ability of helices to form at such a high temperature may be due to the crystalline packing of rods within sublayers, which help direct the chirality of the sheet, as compared to the isotropic nature of homopolymers.

The scrolling of a bilayer sheet or membrane can also be explained by elasticity theory. There are a body of theoretical models pursuing this approach, showing that the sheet should adopt the optimal curvature to minimize the internal elastic free energy[172, 196–199]. The general idea underlying these theoretical model is to incorporate the orientational ordering and/or chirality of the particles into the elastic free energy functional. For example, using the Helfrich-Prost model, Oda et al. demonstrated that a membrane with a crystalline ordering of the particles, similar to our bilayer sheet model, folds into a helical structure with a cylindrical curvature, like H_B[198]. A thorough review on this approach is given in Reference [172].

Because the helical states in all solvent conditions studied are robust under the bombardment of implicit solvent molecules, it is reasonable to state that they are separated from other local energy minima by barriers at least greater than the thermal energy, k_BT. Intriguingly, we observe that it is possible to switch between these helical states by varying the solvent selectivity. Starting with a helical structure already formed under a given condition, we change the interaction potentials between species to represent the target solvent condition. Our simulations reveal that the helices H_A and H_B can easily transform into each other, as can H_A and H_C. The only exception is that while H_B can be changed into H_C, the reverse direction is impossible, at least computationally. The reversible transition from H_A to H_B and H_C results from the fact that, unlike in the latter cases, the non-attractive tethers in H_A tend to segregate to maximize their free volume. When the interactions between the tethers are switched from non-attractive to attractive or vice versa, the sheet easily evolves without being trapped in the intial configuration. In Case B and Case C, however, the tethers are always attractive and tend to aggregate to maximize their contacts. Consequently, when the structure is initialized in H_C, it immediately becomes trapped in this state even when the rods turn from non-attractive to attractive. We also notice the negligible difference in the system potential energy between H_B and H_C in the solvent condition of Case B, i.e. less than 0.5ε per bead. A direct transition from H_C to H_B is therefore entropically prohibitive and cannot occur in our simulations. However, the transition from H_C to H_B might be carried out indirectly through H_A, for example,. transforming H_C into H_A, and subsequently to H_B by varying the solvent selectivity appropriately. This is an example of designing a reversible pathway to switch from one structure to another by judiciously adjusting external conditions.

The folding process of the bilayer sheet into helical structures is essentially kinetically

driven, similar to that of pre-assembled 2-D patterns into hemispheres and open-spheres[8]. Consequently, the initial stretched configuration of the bilayer sheets is critical to the formation of the helices. Despite the isotropic interactions in our minimal model, the chirality of the final structures arises due to the P_2 symmetry packing of the rod pairs which helps to guide the folding direction of the sheet. However, the anisotropic effect of the liquid crystalline sublayers on the folding direction can be diminished if the number of the rod pairs in each sublayer is smaller than a certain value, and the sheet behaves like a chain-like molecule. For example, additional simulations indicate that 48:6 and 48:8 bilayer sheets cannot form regular helices but instead form a worm-like morphology with locally helical segments in Case A and Case B. Other factors that require further elaborate investigations outside the scope of this paper involve the rod aspect ratio and relative strengths of interactions between rods and tethers. These parameters are likely to play important roles in controlling the curvature, pitch and radius of the helices. Our results also suggest that a simplified two-state model may be constructed to describe the transition from extended bilayer (described as a semiflexible membrane) to the scrolled state. In such a model, the P2 packing of the rods that controls the handedness and pitch could be included in a continuum description via an anisotropic elasticity term.

5.2.5 Conclusion

We proposed a model bilayer sheet formed by laterally-tethered nanorods and their analogs that reproducibly forms regular helical structures with a unique handedness. Depending on the solvent selectivity, distinct helical morphologies spontaneously emerge. When the solvent is good for the tethers and poor for the rods, the sheet twists into a helix with a large pitch. When the solvent is poor for both species, the sheet folds along the sublayer separations, resulting in a helix with a smaller pitch and larger interior radius. When the solvent is poor for the tethers and good for the rods, the sheet forms a helix with the interior filled by the tethers. Under a given solvent condition, we demonstrate that the helical structure can be further tuned by adjusting the tether length on one side of the sheet. This work can be used to guide the synthesis of helical structures at nano- and micro-scales from pre-formed sheet-like assemblies. We further show that a helical morphology can be spontaneously switched from one structure to another when the solvent condition is dynamically changed. The model bilayer sheet therefore can serve as a proof-of-concept for fabricating switchable nanomaterials.

Chapter 6
Reconfigurable self-assembly

The reconfiguration of hierarchically assembled structures in the previous chapter suggests that it is possible to design sophisticated nanostructures from particular pre-assembled structures by judiciously changing the effective interaction between the building blocks. In this chapter, we look at the ability of pre-assembled structures to reconfigure via a rather novel approach, i.e. shifting the building block geometry. We demonstrate that when the rod segments are shortened the square grid structure assembled by laterally tethered rods reconfigure into a bilayer sheet structure, and vice versa. We extend the idea of the shape-shifting particles to investigate the reconfiguration of ordered structures in a 2-D lattice, showing various possibilities of assembling nanostructures that are inaccessible otherwise. The biology mimicking reconfigurable assembly inspires a new route towards engineering functional nanostructures.

6.1 Reconfigurable assemblies of laterally tethered nanorods

Reconfigurable nanostructures represent an exciting new direction for materials. Applications of reversible transformations between nanostructures induced by molecular conformations under external fields can be found in a broad range of advanced technologies including smart materials, electromagnetic sensors, and drug delivery. With recent breakthroughs in synthesis and fabrication techniques, shape-changing nanoparticles are now possible, providing a new and exciting ”knob” for self-assembly and phase transformations in addition to the usual thermodynamic parameters and external fields. Here we investigate via molecular simulation a transformation between two thermodynamically stable structures self-assembled by laterally tethered nanorods whose rod length is switched between two values. Building blocks with longer rods assemble into a square grid structure while those with short rods form bilayer sheets with internal smectic A ordering at the same thermodynamic conditions. By shortening or lengthening the rods over a timescale short relative to

the system equilibration time, we observe a transformation from the square grid structure into bilayer sheets, and vice versa. The reconfiguration between two morphologically distinct nanostructures induced by dynamically switching the building block shape serves to motivate the fabrication of shape-changing nanoscale building blocks as a new approach to the self-assembly of reconfigurable materials.[1]

6.1.1 Introduction

It is well known that certain organic supramolecules and liquid crystals exhibit conformational changes under external stimuli such as temperature, pressure, stress, solution pH, and electric or magnetic fields[8, 101, 131, 166, 191, 200–204]. Such microscopic changes can lead to macroscopic structural transformations, which in turn result in significant variation in materials properties such as elastic modulus, thermal conductivity, bioactivity and electromagnetic resonance[131, 202, 203]. For example, Kim et al. reported thermally responsive capsule structures with 25nm diameter pores in a shell formed by the hierarchical self-assembly of double tethered rod amphiphiles[191]. The hydrophilic oligo-(ethylene oxide) coils at one end of the rods shrink upon heating or expand upon cooling, resulting in a reversible closed/open gating motion of the nanopores. Recently, Lee et al. further demonstrated a reversible transformation between two dimensional sheets and tubular structures assembled by laterally grafted rod amphiphiles, also upon heating[166]. These transformations, however, are not between equilibrium states, but are instead strongly pathway dependent, and thus the resulting structures depend on the initial state of the material. The resulting structures therefore may become trapped in local energy minima and are stable under thermal fluctuations. Taking advantage of these kinetic effects, various experimental studies have progressed in engineering higher-order structures that are inaccessible under self-assembly from isotropic states. Ciszek et al. demonstrated that two dimensional flat sheets assembled by amphiphilic rod-like peptides on a template fold into different hollow, sphere-like morphologies depending on the initial sheet pattern[8]. Upon drying, the polymer tethers attached to one end of the rods contract, forcing the flat sheet to curve to reduce the exposure of its hydrophobic surfaces. Our previous simulations predict that flat bilayer sheets of P_2 symmetry assembled by laterally tethered rod-like nanoparticles and their molecular analogs[18, 129] scroll into distinct helical structures, which can transform from one morphology to another by switching the selective solvent conditions[76]. Switching the solvent condition changes the rod-rod, rod-tether, and tether-tether interactions, allowing the

[1] This section is adapted from Reference [77] T. D. Nguyen, S. C. Glotzer, Reconfigurable assemblies of shape changing nanorods, *ACS Nano*, 4, 5, 2584-2594, 2010.

sheet to fold or unfold reversibly in most cases. In those studies, solvophobic forces guide the system towards a certain target structure. However, since the resulting structures are not necessarily at equilibrium, the assembly pathway is unreliable relative to that between equilibrium structures because it depends on kinetics and initial states.

Experiments, theories and simulations reported in the literature have shown that for rod-coil molecules[184, 191, 205–207], block copolymers[51, 181, 208], and tethered nanoparticle shape amphiphiles[15, 17–21, 34–36, 38, 74, 209], the volume fraction and geometry of the constituent components play key roles in the morphology of the assembled structures. For instance, depending on the volume fraction of rod and coil segments, rod-coil molecules in an aqueous medium form cubic ordered micelles, tetragonally- or hexagonally-packed columns, or lamellar structures[184]. In a solvent good for the tethers and poor for the rods, end-tethered rods assemble into hexagonally-packed cylinders with a helical twist if the rod length is comparable to the tether extended length[17, 19]. The helical twist is diminished if the rods are shorter than the tethers due to the entropic effects of the tethers[19]. In previous self-assembly simulations, transitions from isotropic states to ordered structures focus primarily on equilibrium structures. The systems are initially relaxed at high temperature or dilute concentration, and then cooled or compressed gradually. At each temperature or pressure step, the systems are equilibrated until some order parameter, e.g., the system potential energy, becomes stable. The influences of volume fraction and shape anisotropy of the constituent components on assembled structures are therefore usually studied by conducting independent simulations[15, 17–21, 34–36, 38, 74, 207, 208] or experiments[129, 181, 210] on different building blocks and molecules. Ryu and coworkers have reported various hierarchically assembled nanostructures based on rod-coil molecules with different topologies. Numerous simulations on polymer-tethered nanoparticle building blocks[15] including spheres[34–36], rods[17–19, 207], cubes[20, 74] and V-shaped nanoparticles[38] as well as theory[209] have also emphasized the significance of shape anisotropy with regards to the phase behavior and local packing of shape amphiphiles.

However, there have been few studies on how a dynamic change in the building block geometry or conformation, particularly at nanometer length scales, would lead to predictable morphological transformations between assembled structures[8, 166, 191, 211–215]. Polypeptide-based block copolymers, for example, have been recently shown to be potential candidates for stimuli-responsive building blocks[211–215]. Gebhardt et al. demonstrated that the polypeptide rod segment in poly(butadiene)-poly(L-lysine) block copolymers undergoes a reversible conformational α-helix-coil transition in response to a change in pH and temperature. It has also been shown experimentally that colloidal gold nanorods can be shortened or morphed into other shapes such as spheres, bent rods, twisted rods or ϕ-shapes

by using laser pulses with different wavelengths and widths[12, 13, 216]. Yoo et al. synthesized polymeric particles that are able to switch shape in response to changes in temperature, pH and chemical additives[217]. Given the variety of diverse nanocolloid shapes that is now possible[25], fabricating particles from materials that allow a reversible shape change upon application of an external trigger, such as light, would create enormous possibilities for a new class of reconfigurable materials. Polymeric nanorods comprised of an anisotropically crosslinked gel, for example, could be made to swell or contract lengthwise, lengthening and shortening the rod, respectively. Other more complex geometry changes may also be envisioned[218, 219].

In this section, we investigate the spontaneous transformation between two equilibrium structures that each result from the self-assembly, at melt densities, of two types of laterally-tethered nanorods that differ only in their rod length. The building blocks with longer rods assemble into a 3D columnar square grid structure while those with shorter rods form bilayer sheets at the same number density and reduced temperature. By shortening or expanding the rods of the assembled structures quickly relative to the system re-equilibration time, we show that the square grid structure reconfigures rapidly to bilayer sheets, and vice versa. We show that kinetic effects do not prevent the system from evolving between these two structures in either direction, suggesting an experimentally viable approach to nanoparticle shape-induced reconfigurability in these systems. From this model system of building blocks with switchable shape, we aim to inspire the fabrication of switchable nanomaterials from laterally tethered nanorods and their analogs.

6.1.2 Model and simulation method

Model

We use a minimal model of laterally-tethered nanorods similar to one used in our previous work[18, 76, 129] that captures the essential physics of the studied systems (Figure 6.1) including the geometry of the rods and the flexibility of the laterally attached tethers. The rods consist of five spherical beads with diameter σ placed at a center-center distance of 1.0σ for longer rods and 0.5σ for shorter ones. The center bead is linked with the tether via a finitely extensible nonlinear elastic (FENE) spring. The tethers are modeled as linear chains of three spherical beads with diameter σ, bonded via FENE springs. We utilize empirical potentials[15] that are successful in capturing the relevant physics of rod-coil molecules, block copolymers and surfactants[220]. To model the aggregation of the rods and that of the tethers, the interactions between the rod beads and between the tether beads

are modeled by the 12-6 Lennard-Jones potential truncated and shifted to zero at the cutoff distance of 2.5σ to incorporate the short-range attraction and excluded volume interactions. Immiscible species tend to segregate; therefore, the rod-tether interaction is modeled by the softly repulsive Weeks-Chandler-Andersen (WCA) potential to capture their immiscibility. In our simulations, the potential energy well depths ε are chosen to be identical for rod-rod, tether-tether and rod-tether interactions: $\varepsilon_{R-R} = \varepsilon_{R-T} = \varepsilon_{T-T} = \varepsilon$. The natural units for these systems are the diameter of a bead, σ, the mass of a bead, m, and the Lennard-Jones well depth, ε. The time scale is defined as $\tau = \sigma\sqrt{m/\varepsilon}$ and the dimensionless temperature is $T^* = k_B T/\varepsilon$. For block copolymer and nanoparticle systems, a typical example of these parameters is σ = 5nm; $m = 10^{-21}$kg; ε = 50kJ/mol and τ = 0.5ns.

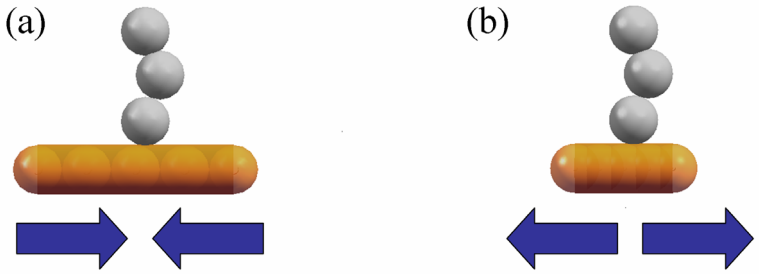

Figure 6.1 Laterally-tethered nanorods with (a) a 5σ long rod segment and (b) a 3σ long rod segment studied computationally in this work. Rod beads are in yellow, tether beads are in white color. Arrows indicate the directions of (a) shortening and (b) lengthening the rods.

Simulation method

Brownian dynamics (BD) is used to simulate the self-assembly of tethered nanorods in a melt-like condition in three dimensions. In BD, the random and drag forces in the equation of motion of each bead serve as a momentum non-conserving thermostat for the system, and hence our simulations sample the NVT ensemble where N is the total number of beads, V is the box volume, and T is temperature. Details of this method can be found in Chapter 2. For self-assembly simulations, we use a similar procedure to that used in our previous phase diagram mapping simulations[17, 18, 36, 38] to sample the system at a number density of $N/V = 0.8$, which is sufficiently high to reproduce a melt-like condition. We cool the system from an initial temperature of $T = 2.5\varepsilon/k_B$, corresponding to a disordered state, by decreasing T step by step with $\Delta T = 0.1\varepsilon/k_B$. At each temperature step, we equilibrate the system until we observe fluctuations in the system potential energy U less than 5% and a morphology that does not substantially change over a time scale of $\approx 20 \times 10^6$ time steps. We also heat and cool the systems with different schedules to ascertain that the cooling paths do not bias the assembled structures. By following this procedure, we seek to find

equilibrium assembled structures and obtain a consistent estimate of the disorder-order temperature for our particular systems. Once the assembled structures are stabilized at temperatures lower than the disorder-order transition, we perform the rod shortening or lengthening by sliding the rod beads along the rod director while maintaining the rod center of mass. To simplify our shape changing procedure in the present study we assume that: (1) the rod shortening/lengthening rate is uniform for all building blocks, (2) the building block symmetry is conserved, and (3) the interactions between rods are fixed during shortening and lengthening. The rods are shortened or lengthened every 10 time steps until the target length is reached. We use different shape-changing rates of $2 \times 10^{-2}\sigma$, $2 \times 10^{-3}\sigma$, $2 \times 10^{-4}\sigma$, and $2 \times 10^{-5}\sigma$ every 10 time steps, to ascertain whether any kinetic effects due to rod lengthening/shortening influence the transformation processes. To ensure that finite size effects are avoided with regards to assembled structures and disorder-order temperature, we run test simulations on several system sizes of N_B = 500, 1000 and 2000 building blocks, corresponding to N = 4000, 8000 and 16000 beads, respectively. For each system size, we also run simulations with different random number sequences for the thermostat and initial configuration, and initial velocity profiles to avoid any artifacts of the random number generator. During the simulation, the number of beads (N), box volume (V), and interaction strengths (ε) between species are held fixed. We choose to show the data for N_B = 2000 and the rod lengthening/shortening rate of $2 \times 10^{-3}\sigma$ every 10 time steps as our representative results in the following sections. Our simulations are conducted using LAMMPS, an open source parallel molecular dynamics code[71], with a LAMMPS extension we developed for this work that allows three-dimensional rigid bodies to change their geometry during simulations.

6.1.3 Results and discussion

We observe upon cooling at fixed volume fraction the formation of a square grid structure and bilayer sheets from the thermodynamic self-assembly of laterally-tethered nanorods for longer and shorter rods, respectively. Our results are in good agreement with previously reported experiments on geometrically analogous rod-coil molecules, which observe both these phases[205, 206]. Since we ascertain that the simulated structures are equilibrium structures, this suggests the experimental structures are thermodynamically stable. Starting from an equilibrium assembled structure (either square grid or bilayers), we shorten or lengthen the rods, respectively, to the target length and monitor the morphological transformation to the other structure. We compare the timescale of the order-order transformation induced by rod shortening and lengthening with that of the self-assembly from isotropic

states.

Self-assembly of longer rods

At a number density of 0.8, we observe that laterally-tethered nanorods in which the rod has length 5.0σ undergo a disorder-order transition from an isotropic state to a 3D square grid structure at $T \leq 2.2\varepsilon/k_B$ (Figure 6.2(a-b)). This morphology may also be called the tetragonal columnar phase because the tethers aggregate into columns, which are separated by a square grid of rods. Similar tetragonal morphologies have been observed computationally in systems of di-tethered nanospheres[35, 36] and experimentally with amphiphilic dumbbell-like and rod-coil molecules with a comparable aspect ratio of rod-coil segments; however in the latter the structure of the stacked rods between tether columns was not known[205, 206]. The formation of columnar structures stems from the lateral constraint between the tether and the rigid part of the building block and their relative lengths according to a geometrical packing analysis[34, 51].

Simulation snapshots reveal how the rods arranged into a square grid pack into bilayer ribbons as the structure extends into the third dimension to maximize their contacts and offset randomly along the axial direction (Figure 6.2(b)) to mitigate the conformational entropy loss of the adjacent tethers. The structure can be characterized by the radial rod-rod correlation distribution $g_{R-R}(r)$ given in Figure 6.2(c) in which the sharp first peak at 1.0σ indicates the side-by-side rod separation and the small second peak in the vicinity of 2.0σ shows the rod packing in linear bilayer ribbons. The two broad peaks at 5.0σ and 10.0σ represent the distances between parallel ribbons, respectively.

Self-assembly of shorter rods

Laterally tethered nanorods for which the rod has length 3.0σ assemble into bilayer sheets for $T < 2.0\varepsilon/k_B$ at a number density of 0.8 (Figure 6.3(a)). Sheet-like (lamellar) structures have been shown to be thermodynamically stable for block copolymers and shape amphiphiles at a sufficiently high concentration and certain relative volume fractions of the immiscible constituents[18, 206]. The formation of sheet-like structures again can be explained by a geometrical packing analysis based on the relative lengths of the rods and the tethers[18, 51]. By forming bilayer sheets, the rods maximize their contacts and allow the laterally-attached tethers to maximize their free volume. Interestingly, when $T < 1.5\varepsilon/k_B$ the rods within each sheet arrange into smectic sublayers with P_2 symmetry due to stronger side-by-side, as compared to end-to-end, attraction interactions between rods

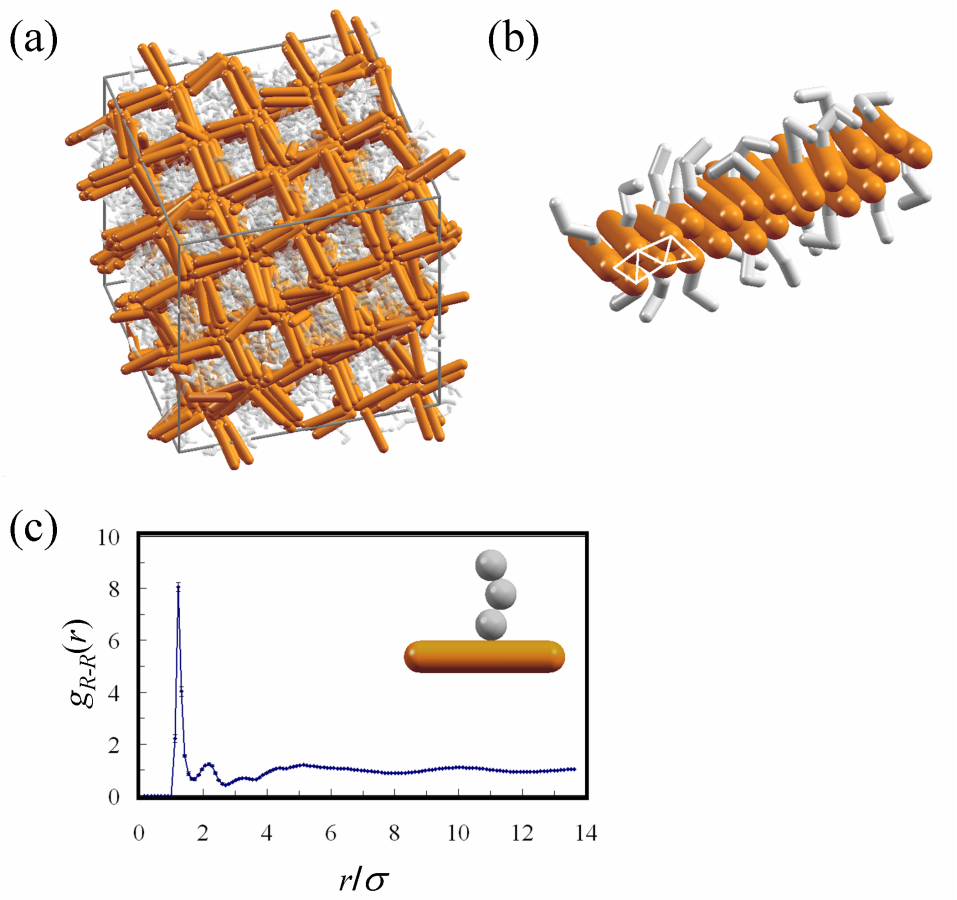

Figure 6.2 (a) Simulation snapshot of a columnar square grid structure formed by laterally-tethered nanorods with a 5σ long rod. Rods are visualized as smooth for clarity of local packing of the rods. (b) A portion of a bilayer ribbon extracted from the structure shown in (a). (c) Radial rod-rod correlation function averaged over 10 snapshots taken every 10^6 time steps. Error bars indicate the standard deviation from the average values.

(Figure 6.3(b)). The P_2 symmetry packing of the rods within bilayer sheets was predicted in previous simulations by Horsch et al. of a solution of laterally-tethered solvophobic rods with the same rod-tether length ratio[18]. Recently, Hong and coworkers observed the formation of scrolled bilayer sheets with similar rod packing pattern in a solid melt of laterally grafted rod molecules[129]. We thus conclude that two key ingredients for the emergence of the rod bilayers and the crystalline P_2 symmetry packing within each bilayer are (i) the immiscibility between the rods and the tethers and (ii) the attraction between the rods. In our model, the attraction energy per unit rod length is greater in the shorter rod than in the longer rod with the same number of beads, compensating the entropy loss of tightly packed (but attractive) tethers, and allowing for an almost zero tilt angle of the rods within the smectic sublayers, i.e., smectic A ordering. The simulation snapshot (Figure 6.3(a)) further indicates that the average distance between adjacent bilayers is approximately twice

the extended length of the tethers. Consequently, the coupling between adjacent bilayers is weak so that the sublayer axial directions in bilayers are uncorrelated. We also note that the cross-section of the bilayers is similar to that of the ribbons in the columnar square grid structure (Figure 6.2(b)); this will play a role later when we examine the transformation between the two structures. The radial rod-rod correlation function in Figure 6.3(c) shows a sharp peak at a distance of 1.0σ indicative of the side-by-side rod packing, a split second peak at 2.0σ and 2.3σ characteristic of a crystalline packing of the rods in bilayers, and a third peak at 3.0σ corresponding to the distance between smectic sublayers.

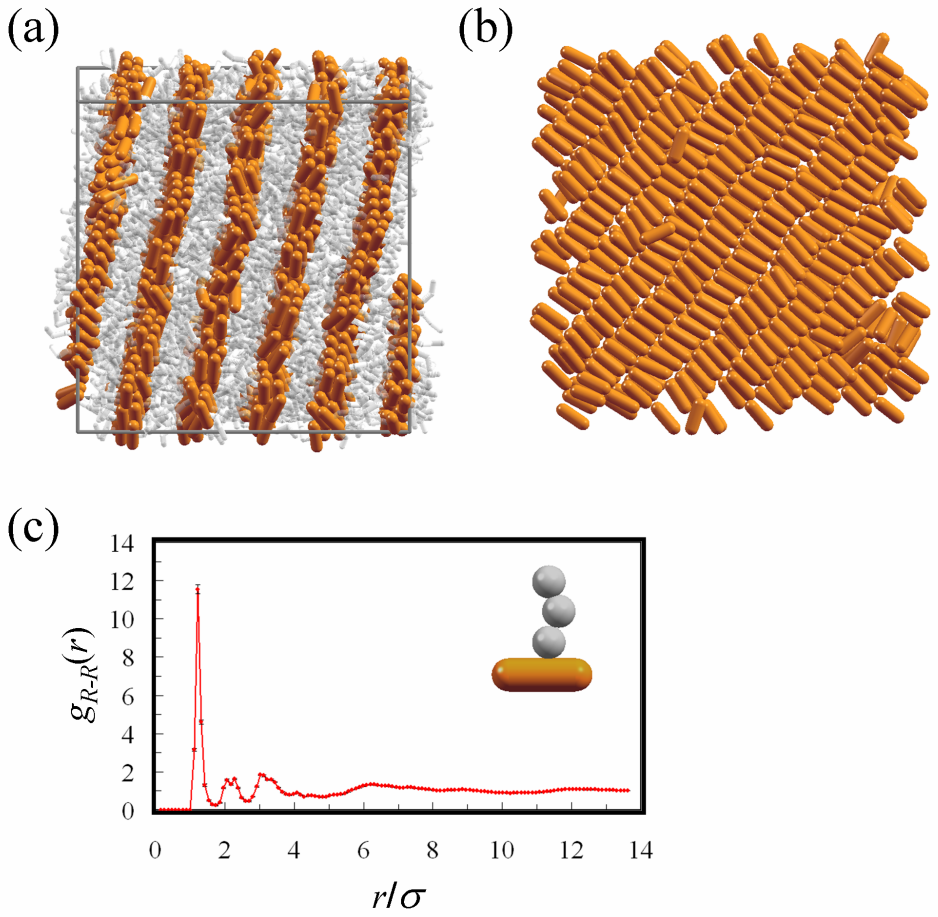

Figure 6.3 (a) Simulation snapshot of bilayer sheets formed by laterally tethered nanorods with a 3σ long rod. Rods are visualized as smooth for clarity of local packing of the rods. (b) Top view of a single bilayer sheet extracted from the structure shown in (a). The tethers are removed for clarity. (c) Radial rod-rod correlation function averaged over 10 snapshots taken every 10^6 time steps. Error bars indicate the standard deviation from the average values.

Reconfigurability between ordered structures

For the purposes of comparing the self-assembly from initially disordered states of the ordered structures presented above with reconfiguration between ordered structures, we define an assembled structure as a structure formed by cooling the system from isotropic states, and a transformed structure as one formed from a different ordered structure after the rods are lengthened or shortened rapidly. At temperature $T = 1.4\varepsilon/k_B$, which is below the disorder-order transition temperatures for both structures, we shorten and lengthen the rod both from assembled structures and from transformed structures to ascertain that the resulting structures are neither kinetically arrested nor metastable, and that the transformation is reversible. The morphological evolution from the square grid structures to bilayer sheets and vice versa is monitored by the change in $g_{R-R}(r)$ and the system potential energy U. A transformation is considered complete if the fluctuations in these quantities are less than 5-10%. We found no significant difference in the final structures in terms of structural and energetic characteristics between starting from an assembled square grid structure versus starting from a transformed structure, indicating that the transformed structures are also thermodynamically stable and at equilibrium, as are the assembled structures.

Shortening rods Starting with the square grid structure formed by rods of length 5σ, we shorten the rods to 3σ, over 10,000 time steps. As shown in Figure 6.1.4(a, left) the system potential energy drops from the value corresponding to the square grid structure, that is, $(4.67\pm0.01)\varepsilon$/bead, to that corresponding to the bilayer sheets assembled from short rods, that is, $(3.57\pm0.01)\varepsilon$/bead. Figure 6.4(b, left) shows $g_{R-R}(r)$, which demonstrates that the transformation into bilayer sheets completes within $\approx 20\times10^6$ time steps. After rod shortening, the square grid structure becomes unstable because the tether columns are no longer separated by the bilayer ribbons, and tethers in adjacent columns are free to interact with each other. The ribbons, however, remain due to the stronger side-by-side attractions between the rods as indicated by the first shape peak in $g_{R-R}(r)$. The ribbons subsequently merge into larger sheets, becoming smectic sublayers within each sheet. In certain runs, we observe defects in the transformed bilayer sheets in which several smectic sublayers (previously ribbons) misalign with the rest, presumably due to imperfections in the starting structures.

Lengthening rods The rod segments are expanded from 3σ to 5σ, over 10,000 time steps starting with stable bilayer sheet structures. The long rods subsequently attempt to re-arrange themselves to increase their contacts, leading to the corruption of the bilayer sheets. The system potential energy jumps to the value corresponding to the square grid

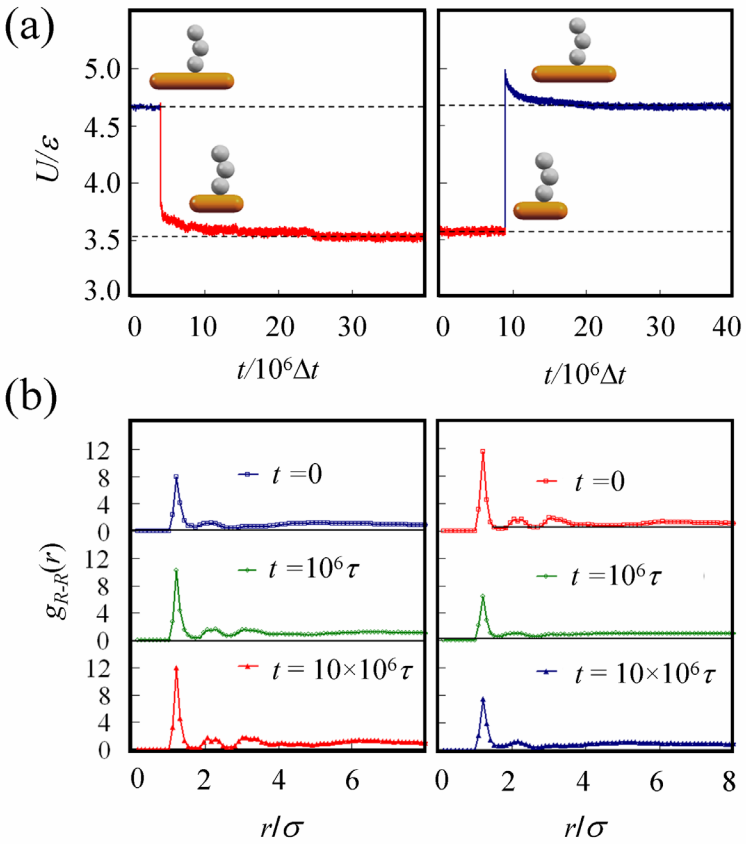

Figure 6.4 (a) Per particle potential energy and (b) radial rod-rod correlation functions during the transformation processes. The rod shortening and lengthening processes are illustrated by the images in the left and right columns, respectively.

structure obtained from self-assembly of long rods, that is, (4.67±0.01)ε/bead. The transformation process completes after $\approx 20 \times 10^6$ steps as determined by the small fluctuations in U (Figure 6.4(a, right)) and $g_{R-R}(r)$ (Figure 6.4(b, right)). During equilibration, the split in the second peak and third peak of $g_{R-R}(r)$ vanish, implying that the smectic sublayers no longer exist; however, the presence of the first sharp peak indicates that the side-by-side rod packing persists. The smaller value of $g_{R-R}(r)$ at the first peak indicates a lower probability of finding side-by-side neighbors and also suggests that the sheet-like aggregates of the rods disappear. We also note that the time evolution of $g_{R-R}(r)$ occurs in the reverse direction as compared to when the rods are shortened.

The driving force for the reconfiguration between the columnar square grid structure and bilayer sheet structure originates from the minimization of the system free energy, which involves the simultaneous maximization of energetically favored rod-rod and tether-tether contacts and conformational entropy of the flexible tethers. However, unlike self-assembly processes in which initial configurations are typically isotropic states, shape-changing in-

duced transformation processes of the type studied here proceed from ordered states, which might suffer unfavorable kinetic effects hindering or preventing the formation of target structures. By shortening and lengthening the rods on a time scale much shorter than the system equilibration time, which is on the order of 40×10^6 steps at $T = 1.4\varepsilon/k_B$ and $\Delta t = 0.002\tau$, we aim at reproducing experimental conditions to examine if kinetic effects due to rod lengthening/shortening would prohibit the formation of target structures in practice. In fact, with different shape changing rates, i.e. $2 \times 10^{-2}\sigma$, $2 \times 10^{-3}\sigma$, $2 \times 10^{-4}\sigma$, and $2 \times 10^{-5}\sigma$ every 10 time steps, the transformations all complete within the system relaxation time, and the system smoothly reconfigures to its new equilibrium, ordered state. Such a process is necessary for shape-induced transformation to be a reliable and predictable way to reconfigure materials' structures.

Intermediate rod lengths

Since a change in the rod length gives rise to such a significant transformation in the symmetry of the structures, it is reasonable to investigate whether there may exist an intermediate rod length between 3σ and 5σ at which the system undergoes an order-order transition between structures with one- (in the case of sheets) and two- (in the case of grids) dimensional periodicity. We perform independent self-assembly simulations with intermediate rod lengths of 3.25σ, 3.375σ, 3.5σ and 4.0σ (Table 6.1). While rods of length 3.25σ assemble into bilayer sheets, rods of length 3.375σ, 3.5σ and 4.0σ form stretched honeycomb, honeycomb (Figure 6.5(a)) and pentagonal grids (Figure 6.5(b)), respectively. The critical rod length for the transition from sheets to grids therefore falls inside a small window from 3.25σ to 3.375σ. It is interesting to note the sensitivity of the assembled structure to small changes in the aspect ratio of the rods. On the other hand, this also implies that polydispersity in the rod length could have negative effects on the assembled structures. For example, as a rough estimation from Table 6.1, the tolerance in the rod length is 8% polydispersity for assembling bilayer sheets, and 4% polydispersity for assembling honeycomb structures.

As predicted by theory and simulations and confirmed by experiments, the volume fraction of constituent components of rod-coil molecules[184, 191, 205–207], block copolymers[51, 181, 208] and shape amphiphiles[15, 17–21, 34–36, 38, 74, 209] determines the assembled morphology at a given concentration. Consequently, one may argue that decreasing the rod length while keeping the tether length fixed is equivalent to keeping the rod length fixed while increasing the tether length, and vice versa. Although this holds true for amphiphilic end-tethered rod systems, the anisotropic nature of the laterally-tethered

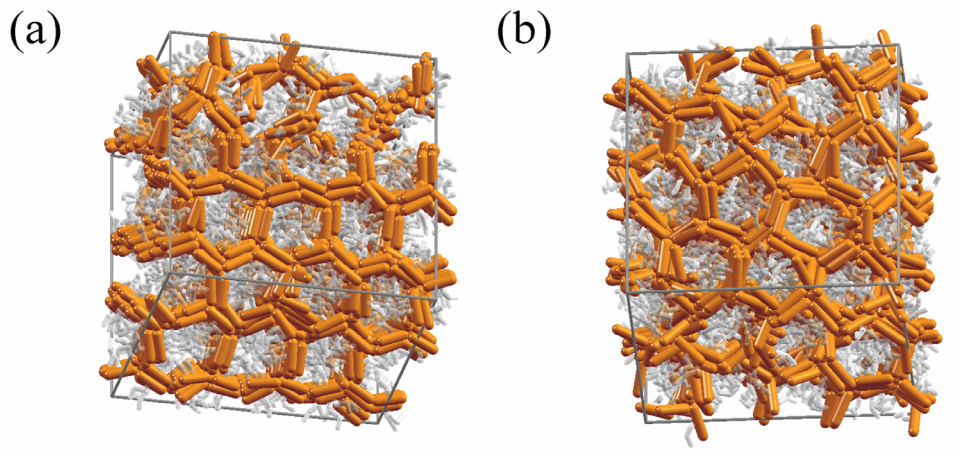

Figure 6.5 (a) Honeycomb grid structures formed by rods of length 3.5σ. (B) Pentagonal grid structures formed by rods of length 4.0σ.

rods causes an asymmetric phase behavior with respect to the constituent volume fraction. While a small change in the rod length can lead to a significant morphological transition, a much larger variation in the tether length is required for such a transition. Simulations with rod length 5σ indicate that the tether length should be increased from 3σ to 10σ to induce a transformation from the columnar square grid structure to bilayer sheets. Moreover, since the increase in the tether length adds more mobility to the system, the disorder-order temperature is lowered, and thus the transformation may not occur at constant temperature as opposed to a small increase in the rod length. We attribute such asymmetric phase behavior to the building block anisotropy caused by the rigid rod segment. Since it is evident that the rods form bilayer ribbons in both structures, we argue that the rod length, which is related to the ribbon width, helps guide the aggregation of the ribbons while maximizing the entropy for the tethers. Meanwhile, the entropic effects of the flexible tethers on the ribbon aggregation only become significant when the variation in the tether length is sufficiently large. For instance, additional simulations indicate that for longer rods, the tether should be as much as three times longer, i.e. consisting of 9 beads, to induce the formation of bilayer sheets. In their recent simulations of bolaamphiphilic liquid crystals with a lateral flexible chain, an analog of our model laterally-tethered rod, Crane and coworkers also showed that while the columnar phases form with a tether length of 3 beads, the lamellar phases only emerge when the chain length is greater than 11 beads[207]. It is therefore instructive that the responsiveness of laterally-tethered rod systems to the rod length is greater than to the tether length.

Table 6.1 Assembled structures formed with different rod lengths and the dimensionality of the periodicity of the structures.

Rod length, σ	Assembled structure	Dimensionality of periodicity
3.0	Bilayer sheets	1
3.23	Bilayer sheets	1
3.375	Stretched honeycomb grid	2
3.5	Honeycomb grid	2
4.0	Pentagonal grid	2
5.0	Square grid	2

Timescales for self-assembly versus transformation

It is useful to compare the dynamics of the transformation process to that of the self-assembly process starting from isotropic states to ascertain whether a given ordered structure forms more easily via transformation or self-assembly. To do this, in addition to $g_{R-R}(r)$ and U, we use the shape matching algorithms proposed by Keys et al.[221] to derive an order parameter that distinguishes between the bilayer sheet and square grid structures. The general procedure for calculating the order parameter is as follows. First, we choose the final self-assembled structures as reference states. Second, we extract a pattern representative of each reference state by choosing a suitable length scale. The cutoff window of interest is chosen to be $[4.0\sigma;5.0\sigma]$ to capture the distance between the rods belonging to parallel bilayer ribbons in both structures. The bond order diagrams of the reference structures (Figure 6.6) show that within that cutoff window the extracted patterns of the reference columnar square grid structure and bilayer sheets are clearly distinguishable. Subsequently, the Fourier shape descriptor of the extracted patterns of the reference states is determined. Similarly, the Fourier shape descriptor of subsequent snapshots during self-assembly and transformation is determined and compared with that of the reference states. The matching between the shape descriptors is used as the order parameter: the closer the order parameter is to unity, the more the structure approaches the reference state. As shown in Figure 6.7, the evolution of the system towards the target structures in the self-assembly process from isotropic states is compared with that in the counterpart transformation process at $T = 1.4\varepsilon/k_B$. The snapshots at different times in the right column show that the transformed systems approach the target states faster than self-assembly from isotropic states (Figure 6.8). This is presumably because of the presence of aligned rod bilayer ribbons in both ordered configurations, as indicated by the sharp first and second peaks of $g_{R-R}(r)$. While it takes self-assembly processes a certain amount of time to form these ribbons from isotropic states, the transformation processes proceed from the ribbons immediately after the rods

change length. Thus for these particular ordered states, and for this particular building block, for which there is a common substructure within both target structures (the ribbons), transformation is more efficient than assembly from a disordered state. For transformations between other order states that share no common substructures, whether self-assembly or reconfiguration is faster is an open and interesting question to be pursued in subsequent work.

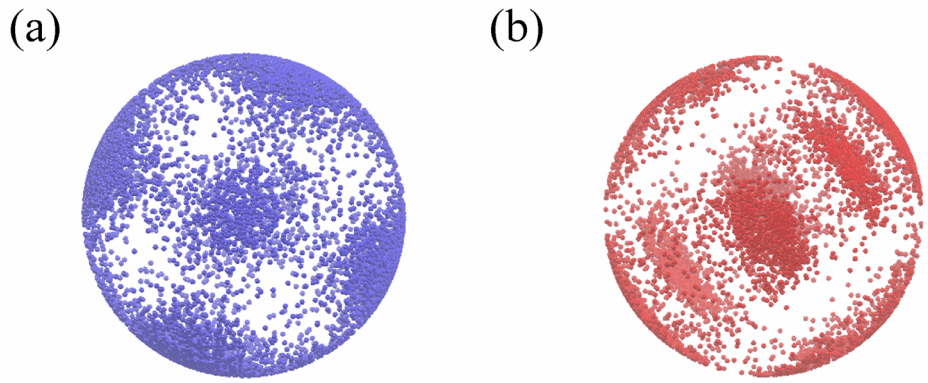

Figure 6.6 Bond order diagram of (a) the square grid structure and (b) bilayer sheets within the cutoff range of $[4.0\sigma; 5.0\sigma]$.

6.1.4 Conclusion

While reconfigurability can easily be found in biological systems and certain liquid crystals, few examples, if any, are available for traditional synthetic materials, especially those based on nanoparticles. In this work, the reconfigurability between two ordered structures assembled by laterally-tethered nanorods serves to inspire the fabrication of next generation nanomaterials able to reconfigure in response to a dynamic change in the building block shape. The kinetic effects due to rod lengthening/shortening are shown not to obstruct the evolution of the system towards equilibrium, but instead expedite the formation of the target structures over the self-assembly process from disordered states. Although the experimental viability of a reversible rod shortening and lengthening procedure has not yet been demonstrated in the literature, we envision that such shape-shifting can be controlled at nanometer scales through the use of, e.g., anisotropic crosslinking within an organic rod made of a polymer gel, or in a similar manner to tuning the conformation of polypeptide-based building blocks[211–214] or melting nanorods using femtosecond or nanosecond laser pulses[12, 13, 216]. Despite the simple shape change considered here, the approach is applicable to more interesting shape changes that involve changes in symmetry and/or topology.

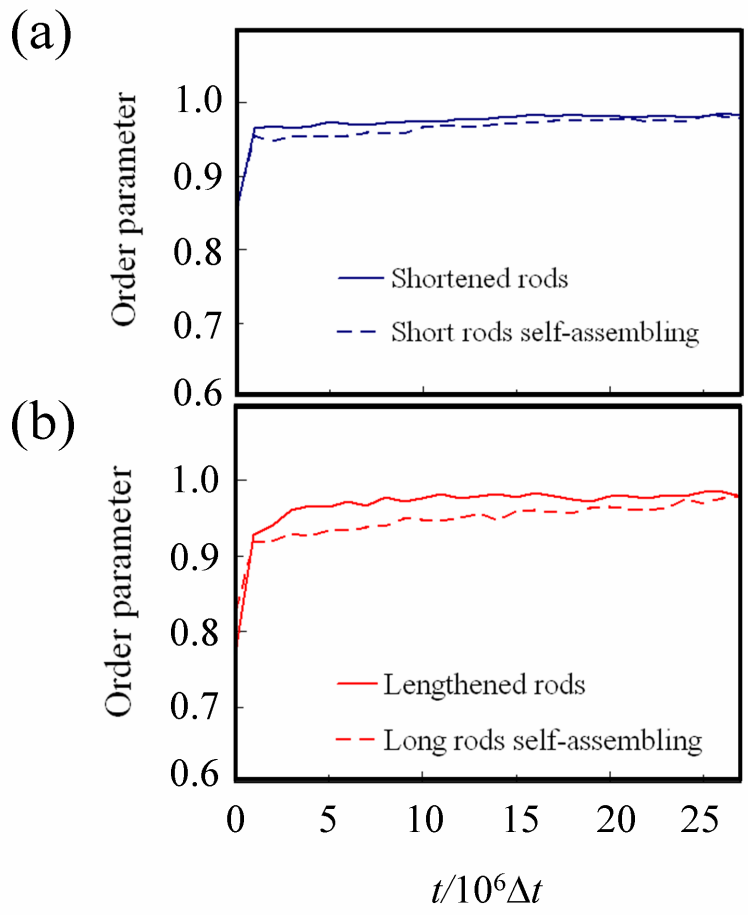

Figure 6.7 Comparison of (a) self-assembly of short rods from isotropic states and order-order transformation induced by shortening rods; and (b) self-assembly of long rods from isotropic states and order-order transformation induced by lengthening rods.

6.2 Self-assembly and reconfigurability of shape-shifting particles

We have investigated the reconfigurability of two-dimensional ordered structures assembled by particles capable of changing their shape. Using molecular dynamics simulations, we show that when particles undergo shape transformations the initially ordered structure would reconfigure into another ordered structure with surprisingly short relaxation time, or into a much denser disordered structure than accessible through self-assembly alone. These results suggest that reconfigurable building blocks can be used to assemble reconfigurable materials and that shape shifting can be a promising mechanism to engineer assembly pathways to ordered and disordered structures.[2]

[2]This is an adapted version of Reference [222] T. D. Nguyen, E. Jankowski, S. C. Glotzer, Self-assembly and reconfigurability of shape-shifting particles, *preprint*.

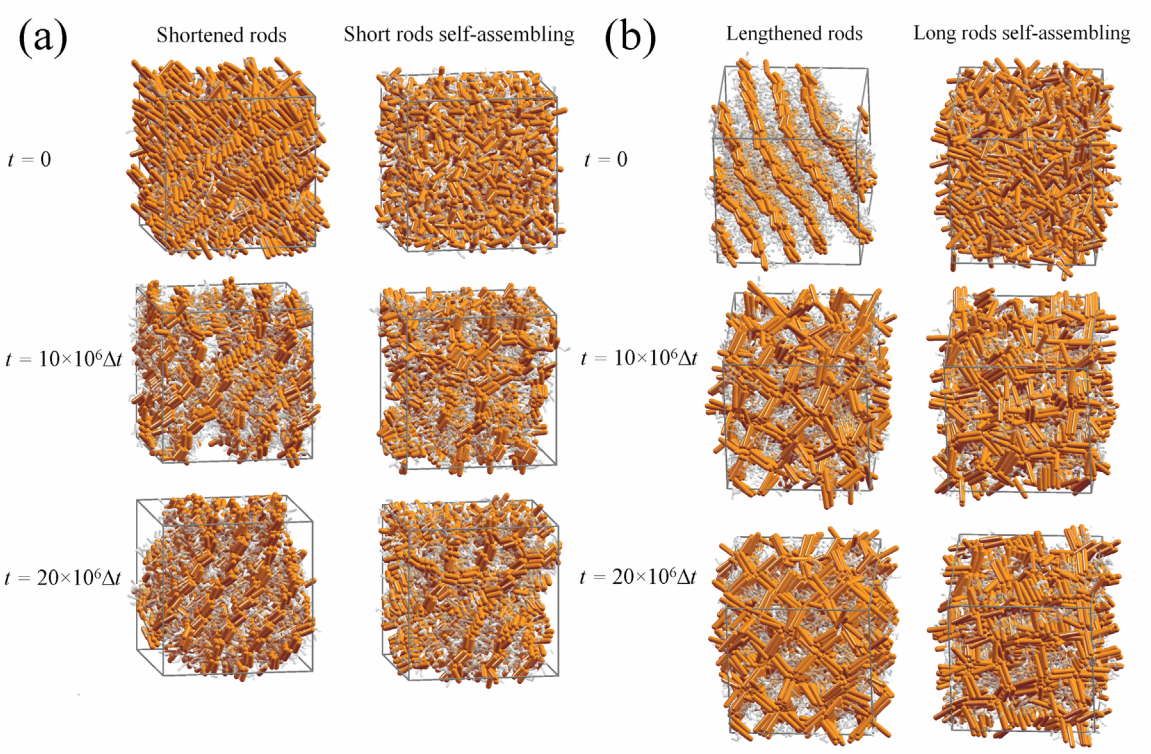

Figure 6.8 System snapshots of (a) shortening rods and self-assembly of short rods; (b) lengthening rods and self-assembly of long rods.

6.2.1 Introduction

Next generation materials will be distinguished by their ability to adapt in novel ways both on demand and to environmental cues to perform important functions. The ability of materials to carry out molecular recognition, autonomous sensing and reporting, and to change properties when needed, all require that intrinsic building blocks be able to reconfigure from one structure to another. While adaptability is ubiquitous in biological systems, few if any examples of this ability can be found in traditional synthetic materials. For instance, it is well known that proteins, the basic building blocks of biology, are the canonical switchable particle with a configuration that is entirely dependent upon solvent pH, the presence of ligands, and the presence of other proteins. Numerous studies have recently been conducted in attempts to mimic such protein-like switchability in nano- and micro-scale systems with implications to adaptive, functional materials. An interesting model of switchable self-assembling objects was developed recently by Bishop et al.[223] They studied the formation of hexamers of triangular robotic pucks, which are able to move on an air hockey table and detach from/attach to other pucks. Klavins et al. utilized this model to demonstrate how switchable components can be used to direct the assembly of a

target structure[224, 225].

Today's materials are primarily static: once formed they retain the same structure throughout their lifetime. Only recently have techniques become available to consider the synthesis and fabrication of dynamically switchable materials, that is, materials whose structure can dynamically reconfigure between two or more states. Materials self-assembled from shape-changing building blocks could be among the first experimentally realized materials in this class. For example, experiments have shown that colloidal gold nanorods can be shortened or shifted to other shapes such as spheres, bent, twisted or ϕ-shaped by using laser pulses with different wavelengths and widths[12, 13, 216]. As the colloidal particles change shape from rod-like to spherical, their packing pattern transforms from nematic to triangular lattices accordingly. The transformations, however, were irreversible. Kim et al. reported thermally responsive capsule structures with 25nm diameter pores on the shell formed by hierarchical self-assembly of double tethered rod amphiphiles. Upon heating or cooling, the hydrophilic oligo-(ethylene oxide) coils at one end of the rods shrink or expand, respectively, resulting in a reversible closed/open gating motion of the nanopores[191]. They also demonstrated a reversible transformation between two dimensional sheets and tubular structures assembled by laterally grafted rod amphiphiles upon heating via a similar mechanism[166]. Alternatively, polypeptide-based block copolymers can also be used as stimuli responsive building blocks due to the ability of the polypeptide segments to adapt various conformations[211, 213, 214]. Gebhardt et al. demonstrated that the polypeptide rod segment in the poly(butadiene)-poly(L-lysine) block copolymers undergoes an α-helix-coil transition in response to a change in pH and temperature[214]. By the time this thesis is written preliminary experiments in Lahann group have shown that biphasic rods are able to reversibly change into various shapes, e.g. bows, lemons or vikings upon heating and cooling. Given the variety of diverse nano- and colloidal particle shapes now available[25], fabricating particles from materials that allow a reversible shape change upon application of an external stimulus, such as a laser pulse, could enable the assembly of a vast number of reconfigurable materials. For example, polymeric nanorods comprised of an anisotropically crosslinked gel could be made to swell or contract lengthwise. Other more complex geometry changes may also be envisioned.

While it becomes evident that the morphology of assembled structures strongly depends upon the comprising building block topology[8, 15, 17–21, 34–36, 38, 74, 75, 105, 156, 184, 205, 209], little is known regarding the response of those structures as the building blocks undergo a shape transition. In the previous section, we have shown that when the rod segments are abruptly shortened or lengthened, the assembled structure reconfigures between a rectangular grid and bilayer sheets[77]. Here we extend the study, seeking to develop an

intuitive and systematic framework for investigating assemblies of nano- and micro- building blocks whose shape can dynamically shifted using external stimuli. Using a model rigid particle that can transform into arbitrary shapes during a simulation, and perform a series of simulations, we study a set of switching scenarios to elucidate the relationship between the shape shifting and resulted structural reconfigurability. The particles are initialized in a pre-assembled two-dimensional ordered structure, and then uniformly transformed into different shapes. We demonstrate that by shifting the building block geometry (1) expected structures can be assembled more efficiently and with fewer defects than self-assembly from disordered states; (2) unexpected ordered structures can emerge; and (3) ordered, reconfigurable structures can be assembled. These results serve to inspire novel approaches to the fabrication of adaptive nanomaterials as well as to engineering assembly pathways to structures which are inaccessible via traditional assembling methods.

6.2.2 Model and simulation method

Model

We develop a generic coarse-grained model interacting with empirical pair-wise interactions, similar to those commonly used to model systems of molecules, nanoparticles and colloids[25]. Each model particle is composed of N_B coarse-grained spherical beads, frozen into rigid bodies. Unlike in previous studies[17–21, 34–36, 38, 74, 75], however, these rigid particles are transformed into various shapes during simulations by gradually translating the constituent beads of a particle in the body-fixed coordinates towards target geometries while keeping them rigidly connected. The particles are transformed at the same rate along the same path with respect to the particle body-fixed coordinates. This is to model how the actual building blocks often react to the environment changes such as pH, ionic strength or directional external field. Figure 6.9 shows the initial two-dimensional ordered structures assembled by spheres (Figure 6.9(a)) and rods (Figure 6.9(b)) studied in this work. We choose these structures as initial states since they are ubiquitously observed in experimental assemblies of spherical and rod-like particles on a flat interface. For spherical particles, constituent beads (N_B = 4, 5 and 7) are initially placed on top of each other; meanwhile, for rod-like particles (N_B = 4), the center-center distance between adjacent beads is equal to the bead diameter, σ. The target shapes shown in Figure 6.10 can be divided into two categories: convex (squares, rhombuses, pentagons) and non-convex shapes, which include rod-like (L-shaped, hockey sticks, zigzags) and branched (cross-shaped, T-shaped, Y-shaped) particles.

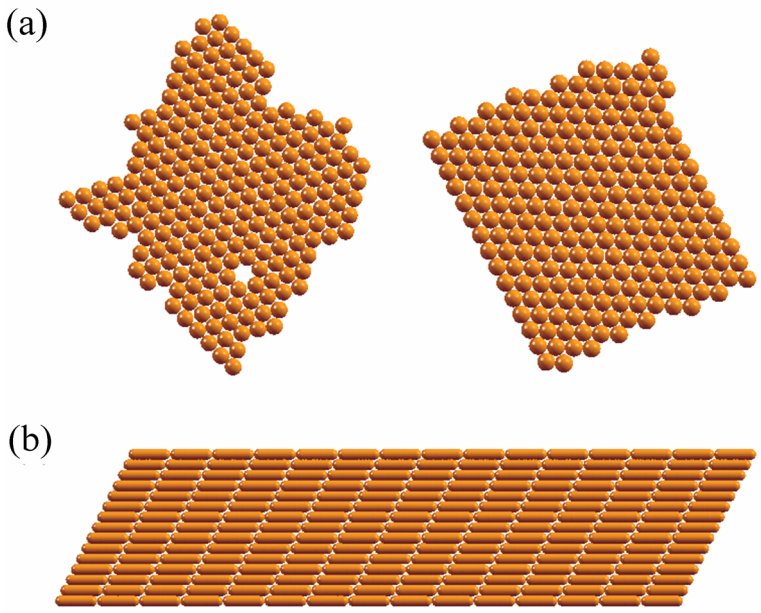

Figure 6.9 Initial ordered structures: (a) spheres packing in a triangular lattice; (b) rods packing in a smectic-like structure.

The interaction between constituent beads from different particles is modeled by a site-site 12-6 Lennard-Jones potential, truncated and shifted to zero at the distance of 2.5σ. The anisotropic nature of the interaction between particles is inherently incorporated into the particle geometry without any explicit modification in the force field. The interaction strength (ε) between beads is fixed during the shape shifting process. Since we seek to understand the role of particle shapes in determining resulted structures, a sufficiently large value of ε that prevents the structures from melting is adequate. As shown later, a value of ε greater than $1.2k_BT$ is sufficient to induce the aggregation of particles into clusters. The data shown below is obtained for $\varepsilon = 4.0k_BT$, or equivalently, $T^* = 0.25$ and the transformation rate of $10^{-5}\sigma$ every 10 time steps unless stated otherwise.

Simulation method

We use Brownian dynamics, a stochastic molecular dynamics method as described in Chapter 2, to simulate the evolution of an isothermal system of particles on a two-dimensional surface with periodic boundary conditions. At each time step, the beads in each particle are moved together as a rigid object. We vary the transforming rate, or equivalently, the number of time steps to complete the shape transformation, and perform multiple independent runs to verify the robustness of our results. After the particles adopt target geometries, the simulations run until the structure reaches an apparently stable state. The system sizes are

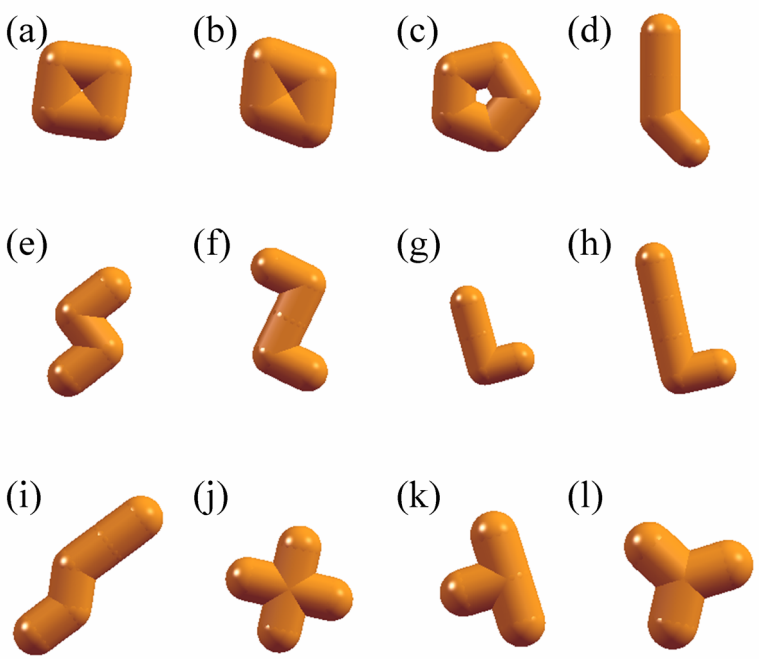

Figure 6.10 Target shapes for shape-shifting from spheres and rods. Convex shapes: (a) square; (b) rhombus; and (c) pentagon. Non-convex shapes: (d) hockey sticks H4; (e) zigzag Z4; (f) zigzag Z5; (g) L-shaped L4; (h) L-shaped L5; (i) sheared zigzag SZ5; (j) cross-shaped; (k) T-shaped; and (l) Y-shaped particles Y4. The trailing number indicates the number of spheres in each particle.

small enough to achieve equilibration in a reasonable amount of time and large enough to avoid finite size effects in the local structures. A typical simulation consists of $N_P = 225$ particles, each containing $N_B = 4$, 5 or 7 beads. We perform simulations of particles in their target shapes from disordered states at instantaneous temperature to compare the resulting structures and those obtained from shape shifting. In these simulations, we attempt to overcome kinetic traps by frequently annealing the system. Our simulations are conducted using LAMMPS[71], using a LAMMPS extension we developed for this work that allows three-dimensional rigid bodies to change their geometry during simulations.

Free energy calculations

To investigate the thermodynamic stability of the ordered structures resulting from shape shifting as compared to those predicted by BUBBA for the target shapes at a given temperature, we perform the lattice-coupling-expansion method[57, 226, 227] to calculate the excess free energy of the structures under consideration with respect to their reference Einstein crystals. The potential energy used for thermodynamic integration in the coupling stage

is[226, 227]:

$$\tilde{U}(\mathbf{r}^{N_P}, \mathbf{Q}^{N_P}, \lambda) = U(\mathbf{r}^{N_P}, \mathbf{Q}^{N_P}) + \lambda \sum_{i=1}^{N_P} \left(k_t (\mathbf{r} - \mathbf{r}_{i0})^2 + k_r \sin^2 \theta_i \right) \tag{6.1}$$

where N_P is the number of particles, k_t and k_r are the translational and rotational spring constants, respectively. The external potential is composed of translational and rotational terms. The translational term couples the particle center of mass with a lattice site. The rotational term biases the particle orientation towards a preferential direction in the crystal. During the coupling stage, λ is varied from 0 to 1 to transform from the original structure to a structure in which the particles are tethered to the lattice sites and their orientation is constrained to the preferred orientation. θ_i is the angle from the orientation of the particle i from their preferred orientation, extracted from the change in the quaternion from the original orientation: $\Delta\mathbf{Q} = \mathbf{Q}^{-1}\mathbf{Q}_0$ where $\mathbf{Q}_0$ and $\mathbf{Q}$ are the original and instant quaternions, respectively. The Helmholtz free energy change in the coupling stage is given by[227]:

$$\Delta F_1 = \int_0^1 \left\langle \frac{\partial \tilde{U}}{\partial \lambda} \right\rangle_\lambda d\lambda = \int_0^1 \left\langle \sum_{i=1}^{N_P} \left(k_t (\mathbf{r} - \mathbf{r}_{i0})^2 + k_r \sin^2 \theta_i \right) \right\rangle_\lambda d\lambda \tag{6.2}$$

Once the coupling stage is completed, the particles (and their lattice sites) are brought away from each other by a box size expansion. During the expansion stage, the parameter γ is gradually increased from 1 corresponding to the initial box length until the virial vanishes. The free energy change in the expansion stage is given by[57]:

$$\Delta F_2 = \int_1^\infty \left\langle \sum_{i=1}^{N} \sum_{j>i}^{N} -\mathbf{f}_{ij} \cdot \mathbf{r}_{ij}^0 \right\rangle_\gamma d\gamma \tag{6.3}$$

where $\mathbf{r}_{ij}^0$ is the initial separation between two atoms i and j. The excess free energy difference between the original ordered structure and the Einstein crystal is then determined by the sum of ΔF_1 and ΔF_2: $\Delta F = F - F_{Ein} = -(\Delta F_1 + \Delta F_2)$. During the coupling and expansion stages, the system is equilibrated at constant temperature using the Nose-Hoover thermostat. The ensemble average is performed by averaging over 20 equilibration snapshots within each step of λ and γ. The free energy of molecular Einstein crystals can be determined analytically[226, 227].

6.2.3 Results and discussion

The initial ordered configurations are prepared by either performing self-assembly simulations of spheres and rods from isotropic states or initializing these particles in ordered lattices. For the systems prepared from disordered states, the largest ordered aggregates are extracted and subsequently put in another larger simulation box where they undergo shape transformation. Our results indicate that in many cases the shape shifting not only enhances the formation of ordered structures from target shape particles over their self-assembly from disorder states, but also allows for the reconfiguration between these ordered structures and their initial structures. This enables one to design multiple-step assembly of desired ordered structures, which are unattainable from conventional assembly methods. Here we define reconfigured structures as those resulting from shifting the particle shape, and self-assembled structures as those formed by particles in the target shape from isotropic states.

Table 6.2 Resulting structures from shifting spheres and rods.

Initial shape (Initial structure)	Target shape		
	Convex	Rod-like	Branched
Spheres (triangular lattice)	Ordered	Disordered	Ordered*
Rods (smectic structure)	Ordered	Ordered	Ordered*

*Except for T-shaped particles

Efficient assembly

Table 6.2 shows that when spheres and rods pre-assembled in ordered structures are shifted into other shapes, the target particles form ordered structures in most cases. For convex target shapes, i.e. squares, rhombuses and pentagons, and symmetric branched shapes, i.e. Y-shaped and cross-shaped particles, the initial lattices switch to ordered structures, which are predictable for those particles of that shape (Figure 6.11). When these particles self-assemble from disordered states at low density, they are prone to falling into kinetic traps, resulting in a small correlation length of the ordered domains. To avoid such kinetic traps, the system should be slowly cooled and/or compressed as in experiments and conventional self-assembly simulations. Meanwhile, the re-arrangement of particles from ordered configurations as they transform to target shapes allows for the formation of ordered domains with correlation lengths comparable to that of the initial configurations. For example, when spheres in a triangular lattice grow into squares, their hexagonally packed nearest neighbors help maintain the close-packing of the lattice; meanwhile, the square shape guides the pack-

ing into a rectangular lattice (Figure 6.11(a)). Similarly, the rhombuses transformed from either spheres or rods form the same crystalline structure (Figure 6.11(b)), as do pentagons (Figure 6.11(c)). Likewise, when cross-shaped particles are either grown from spheres or transformed from rods, they easily interleave with their neighbors (Figure 6.11(d)). The local ordering of the reconfigured structures for these target shapes is identical regardless of the initial particles and configurations. T-shaped particles, however, are an exception due to their asymmetry.

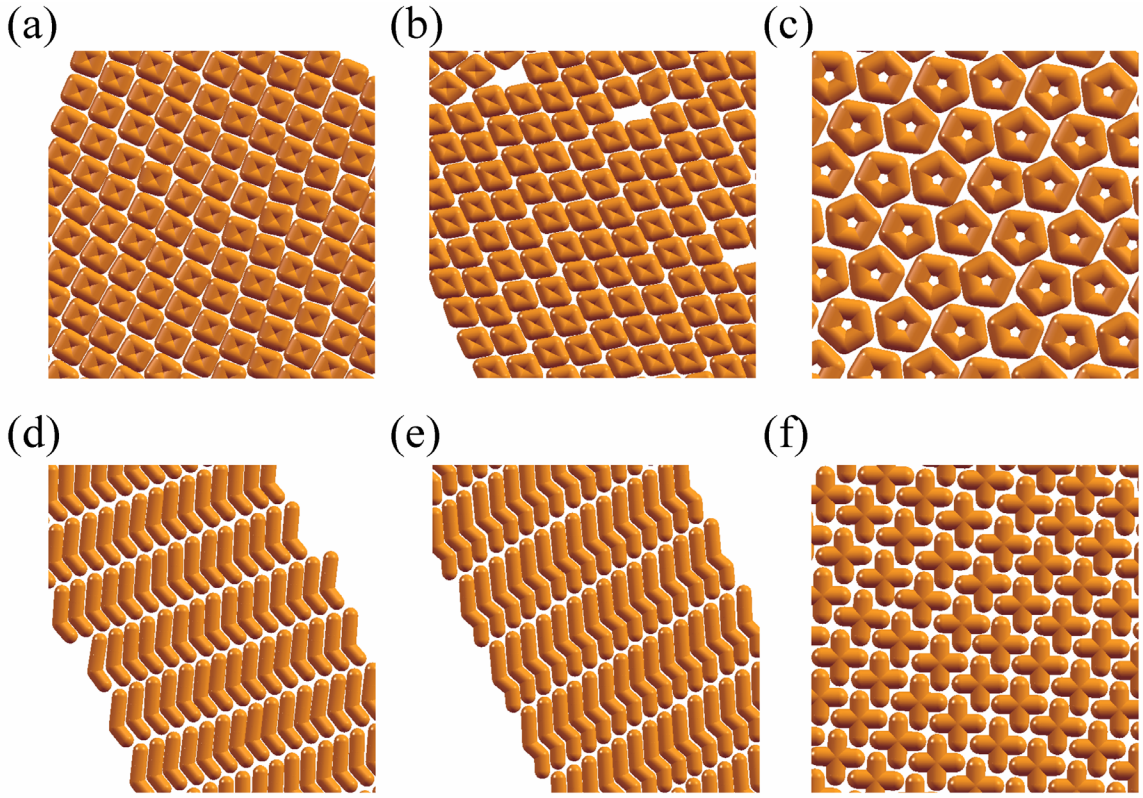

Figure 6.11 Ordered structures by shifting particle shape from (a) sphere to square; (b) rod to rhombus; (c) sphere to pentagon; (d) sphere to cross-shaped particle; (e) rod to sheared zigzag SZ5 and (f) rod to hockey H4.

Rod-like particles such as hockey sticks, zigzags and L-shaped particles rarely assemble into long range ordered structures because of their energetic anisotropy, particularly at low density or temperature. In order for these rod-like particles to read their ground state, they typically need to be driven by an external field, or gradually cooled with a significant amount of time to relax into ordered structures. However, when these anisotropic particles are transformed from rods, which are geometrically similar, the ordered structures we desire from self-assembly emerge spontaneously. For example, when hockey sticks H4 and sheared zigzags SZ5 result from bending rods, the presence of initial smectic layers guides the particles to nest with their adjacent neighbors in the same layer, leading to polar smectic

structures (Figure 6.11(d-e)). As a result, crystalline structures can emerge without any increase in pressure or decrease in temperature. We employ the general shape-matching algorithm developed by Keys et al.[221] to compare the resulted structures from shape transformation and from isotropic self-assembly with corresponding target patterns. The shape-matching order parameter S varies in [0.0; 1.0] where $S = 1.0$ indicates a perfect match. Figure 6.13(a) shows the order parameter of pentagons, hockey sticks and Y-shaped particles, representative of convex and non-convex shapes, as functions of inverse temperature. We found that for non-convex target shapes the transition into ordered structures was much sharper as they underwent shape transformation than it was for self-assembly at instantaneous temperature. Note that the shape-matching order parameters are measured at different cutoff windows depending on the length scale of interest for each structure. At higher temperatures, the difference between reconfigured and self-assembled structures is insignificant because the systems are all in isotropic states. At low temperatures, self-assembled structures from Y-shaped particles, hockey sticks ($1/T^* > 1.2$) and pentagons ($1/T^* > 2.0$ or $T^* < 0.5$) suffer from kinetic traps, and hence have more defects than the counterpart structures generated from shape-shifting. From Figure 6.13(a), we suppose that there would be a critical temperature, i.e. $1/T^* = 1.2$ for non-convex shapes and $1/T^* = 2.0$ for convex shapes in our model system, below which the shape-shifting induced reconfiguration is advantageous over self-assembly from disordered states with longer range ordering and shorter relaxation times.

When rod-like particles such as hockey sticks, zigzags, and L-shaped particles are grown from spheres, the resulted structures do not have any smectic-like ordering as they did when transformed from rods (Figure 6.12). This is because the directionality inherent to the triangular lattice of spheres does not favor the smectic ordering present in rod layers. The only visual difference between reconfigured and self-assembled structures is the local packing density of particles at instantaneous temperature. For some representative non-convex shapes (Figure 6.13(b)), the local density of reconfigured structures is remarkably higher than that in self-assembled structures at instantaneous temperature, again due to the initial close-packed configuration. These results suggest that for non-convex shapes, particularly those with highly anisotropic geometry, choosing a good candidate for the initial shape and ordered configuration, e.g. with favorable directionality, is crucial to stabilizing final ordered structures.

Preliminary experimental results from Lahann group demonstrated that submicron-sized biphasic rods can be bent into bows and deformed into "bull-head" shapes (Figure 6.14) upon raising temperature above the glass temperature of one of the polymeric compartments. Our simulations suggest that a smectic structure assembled by rods reconfigure into another

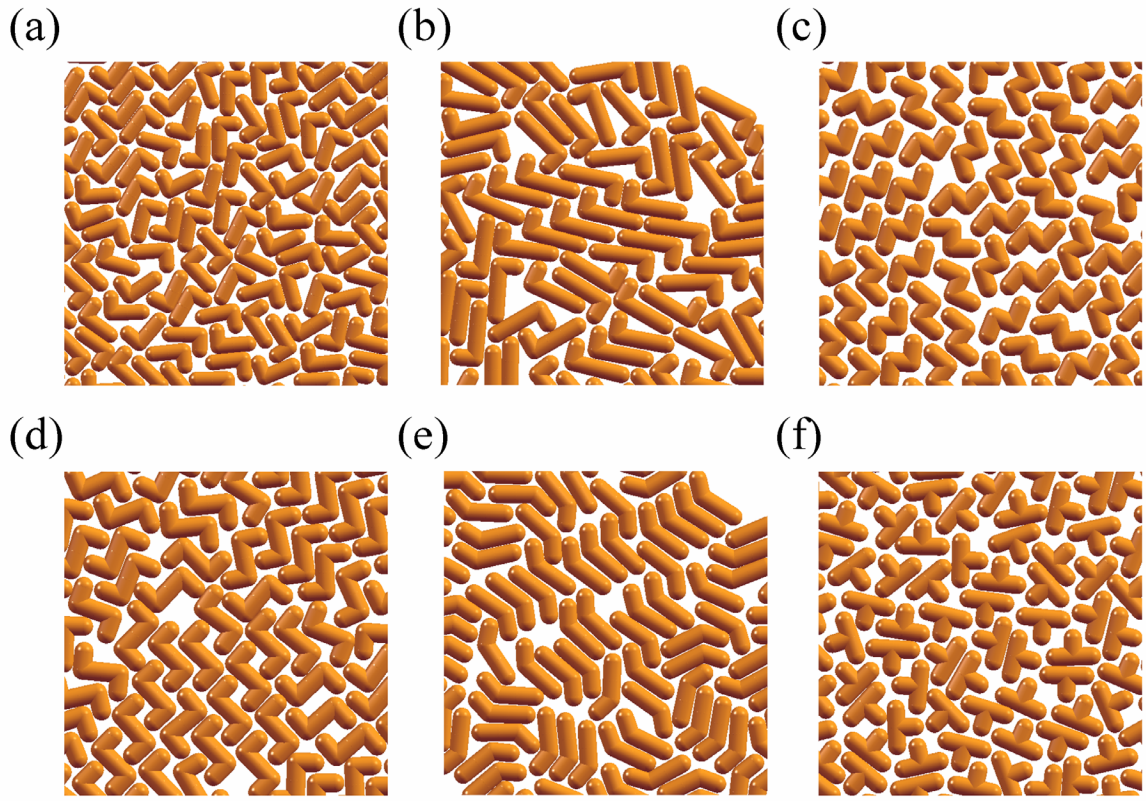

Figure 6.12 Disordered structures obtained from transforming spheres into (a) L-shaped L4; (b) L-shaped L5; (c) zigzags Z4; (d) zigzags Z5; (e) hockey sticks H4 and (f) T-shaped particles.

smectic structure when the rods are bent into bows (Figure 6.14(b)). When the bow-shaped particles instantaneously aggregate at the same temperature, the resulting structure is much less ordered (Figure 6.14(a)). In this case, the reconfigured structure is more preferred than the self-assembled counterpart both energetically and entropically. Note that when slowly cooled from disordered states, the bows assemble into the same morphology as the reconfigured structure.

When the rods are shifted to ”bull-head” shapes, the reconfigured structure is more ordered than its self-assembled counterpart at the same temperature (Figure 6.14(c-d)). The ordered structures cannot be attained via our self-assembly simulations even with a slow cooling schedule due to the highly concave geometry of the particles. This example, again, illustrates how shape shifting allows for more efficient assembly than the traditional self-assembly procedure.

When the rods are shifted to ”bull-head” shapes, the reconfigured structure is more ordered than its self-assembled counterpart at the same temperature (Figure 6.14(c-d)). The ordered structures cannot be attained via our self-assembly simulations even with a slow cooling schedule due to the highly concave geometry of the particles. This example,

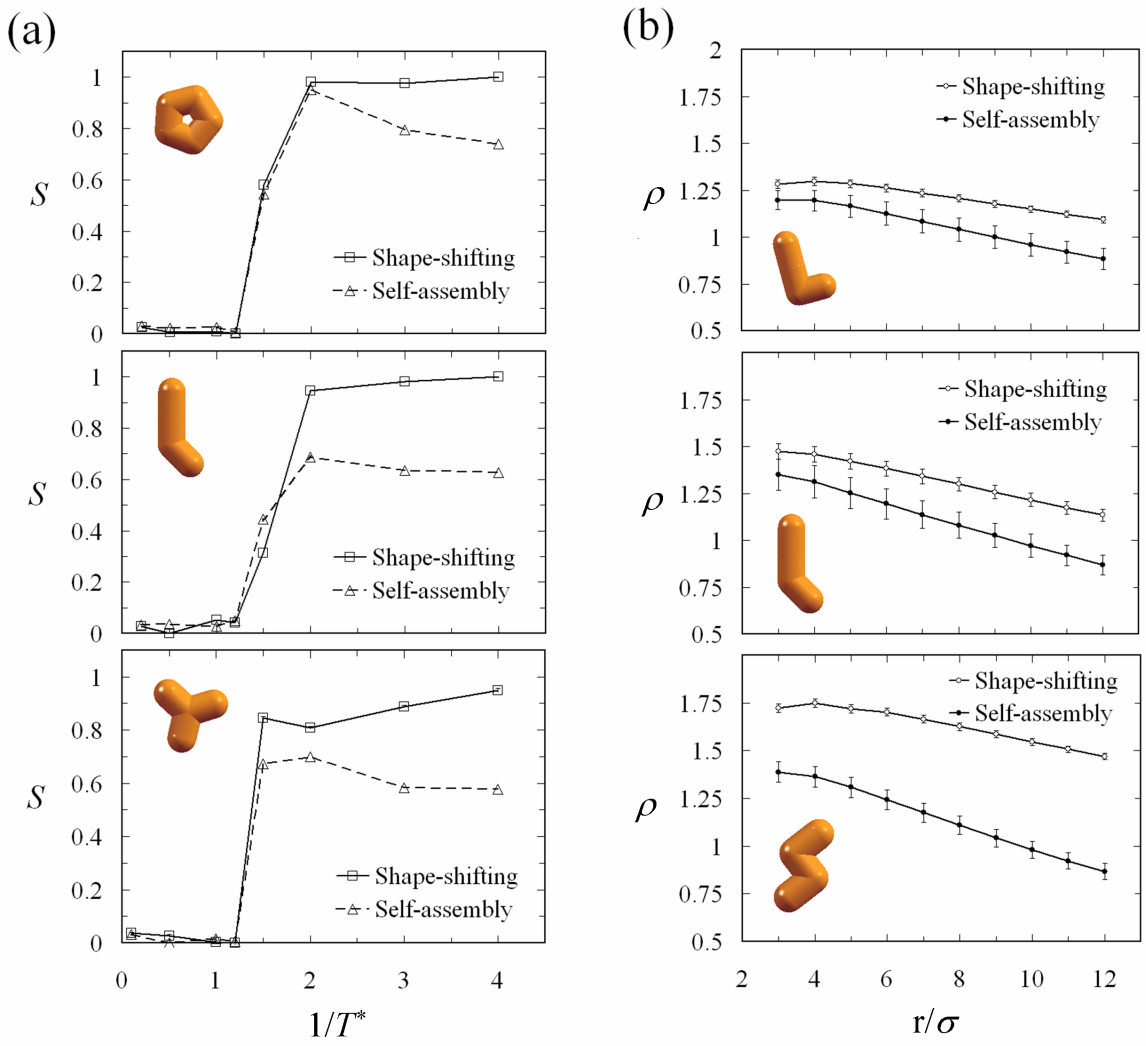

Figure 6.13 Comparison reconfigured to self-assembled structures: (a) shape-matching order parameter as function of inverse temperature; and (b) local number density ($\rho = N/F$, where N is the number of beads and F is the local circular region area, averaged over the whole sample) as function of local region size. Particles start aggregating when $1/T^* > 1.2$. The self-assembled structures are obtained from a fast quench from disordered states. The error bars are standard deviations from the mean value measured from 20 samples.

again, illustrates how shape shifting allows for more efficient assembly than the traditional self-assembly procedure.

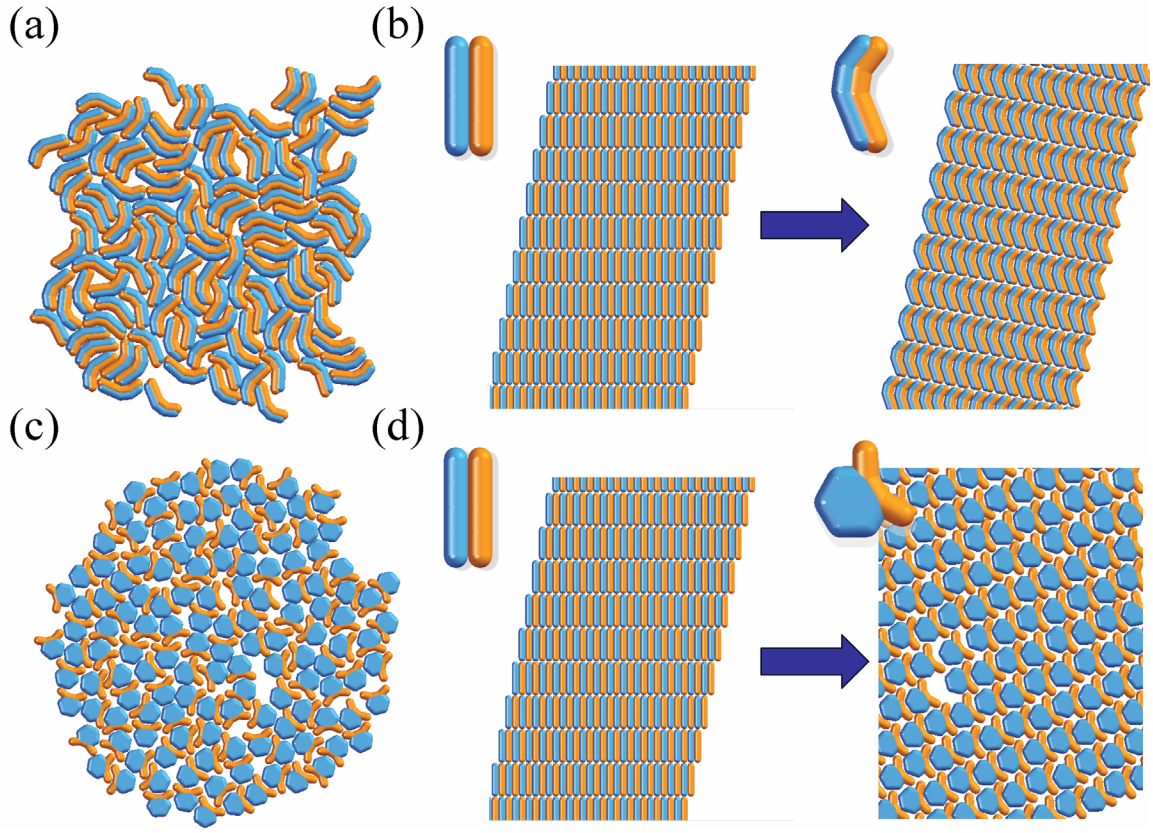

Figure 6.14 Simulations with biphasic bows and "bull-head" shapes. (a) and (c): Self-assembled structures at $T^* = 0.2$. (b) and (d): Reconfigured structures from a smectic structure of rods at $T^* = 0.2$.

Pathways to unexpected ordered structures

While the crystalline structures of convex shape particles can be achieved via self-assembly, those of non-convex particles are normally unexpected since they are either prone to kinetic traps or prohibited by an enormous number of local energy minima. We use the Bottom-Up Building Block Assembly (BUBBA) method[228] to predict energy-minimizing clusters resulting from the self-assembly of a given building block. Although these clusters are attainable by equilibrium Monte Carlo simulations, it is not clear if they emerge at nonzero temperature with thermal fluctuations. Our self-assembly simulations show that at nonzero temperature non-convex shape particles such as L-shaped L4 and L5, hockey sticks, zigzags, T-shaped, cross-shaped and Y-shaped particles nucleate into precursors of several energy minimum structures as predicted by BUBBA; yet the overall structures are disordered.

Instead, we attempt to produce those motifs by transforming spheres and rods into target shapes. In most cases, the target ordered structures form with a much longer correlation length as compared to self-assembly (Figure 6.14). For instance, the zigzags Z4 and Z5 pack into the target structure when transformed from rods (Figure 6.15(a-b)). For hockey sticks H4 (Figure 6.15(c)), BUBBA predicts that the energy minimizing structure contains a mixture of mirror-image motifs, which are energetically identical, suggesting that the assembled structure is likely to be racemic. By shifting rods to hockey sticks, the reconfigured structure is ascertained to have a uniform handedness. Figure 6.15(d) shows that the target structure for Y-shaped particles can be achieved from both growing spheres and transforming rods. There are certain exceptions: the L-shaped particles obtained by bending the rods form closed packed (Figure 6.15(e)) and porous ordered patterns (Figure 6.15(f)) depending on the length ratio of the branches, L4 or L5, respectively. Both structures have higher potential energies than their BUBBA-predicted counterparts, indicative of kinetically trapped configurations; however, they are stable and reproducible in our simulations. Similar to hockey sticks, the L-shaped particles exhibit a uniform handedness in the reconfigured structure, which is not observed in self-assembly simulations. The porosity in the structure formed by L-shaped particles L5 results from the particle roughness with spherical beads attempting to pack efficiently with their neighbors. As it turns out, by judiciously shifting the building block geometry, one can achieve desired ordered structures, which are inaccessible to traditional assembly methods.

We compare the excess free energy of reconfigured structures and of energy minimizing structures predicted by BUBBA with respect to their reference Einstein crystals for several shapes (Figure 6.16). As shown in Figure 6.16(a-b), there is no remarkable difference in the excess free energy between the reconfigured structures formed by shapes L4 (Figure 6.15(c)) and H4 and (Figure 6.15(e)) and their energy minimizing counterparts for $T^* = 0.2 - 0.4$. This suggests that the ordered reconfigured structures are as thermodynamically stable as energy minimizing structures in this temperature window. For $T^* > 0.4$, these reconfigured structures are less stable than their energy minimizing counterparts.

For L5 shapes (Figure 6.16(c)), the excess free energies of reconfigured structures and energy minimizing structures are within statistical errors, indicating that these structures are equally thermodynamically stable. It is noteworthy that while the energy minimizing structures for L4 shapes (Figure 6.16(a), bottom-right) and L5 shapes (Figure 6.16(c), bottom-right) are almost identical, a slight difference in the aspect ratio of the particles could affect the thermodynamic stability of reconfigured structures. The calculations for other cases are underway.

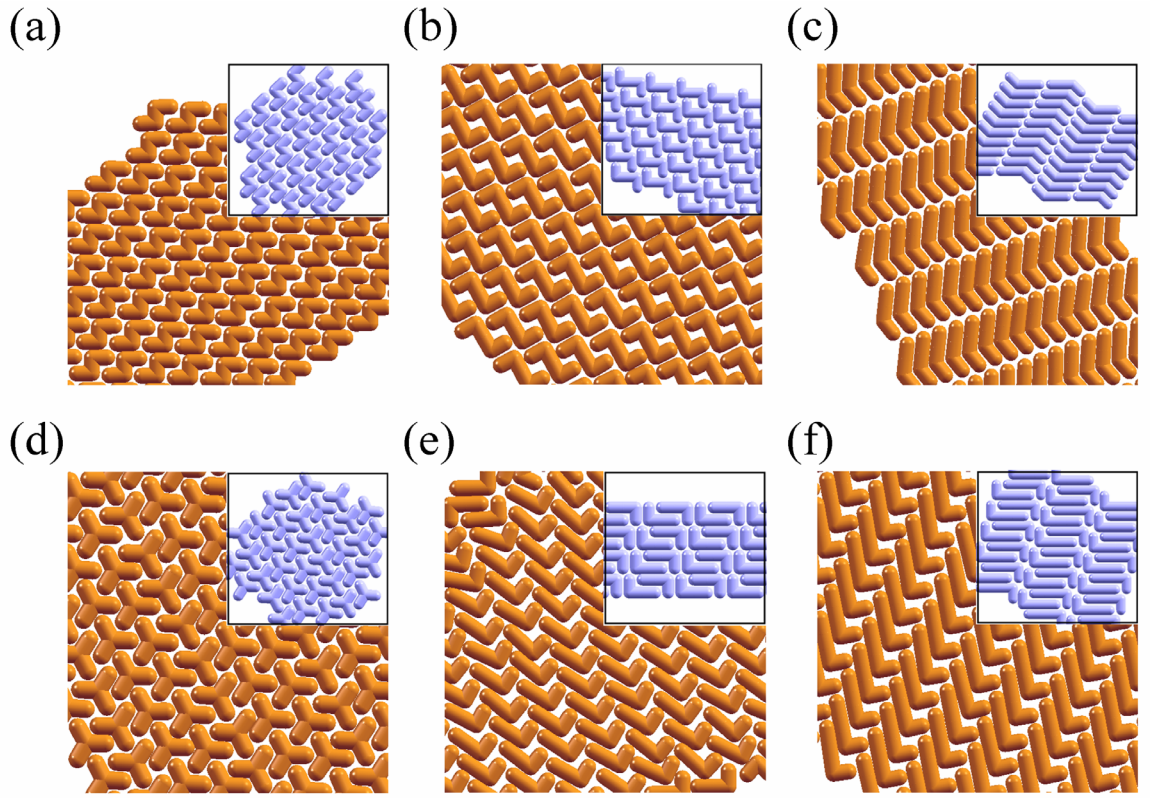

Figure 6.15 Ordered structures obtained by shape shifting and predicted by BUBBA (inset): (a) zigzags Z4; (b) zigzags Z5; (c) hockey sticks H4; (d) Y-shaped particles Y4; (e) L-shaped particles L4; and (f) L-shaped particles L5.

Reconfigurability between ordered structures

When the particles in Figure 6.10 are transformed into spheres the triangular lattice is always recovered regardless of the transformation pathway. We find that direct reconfiguration between ordered structures is reversible when the particle shape is shifted between convex particles such as squares, rhombuses and pentagons. For backward transformation to rods from rod-like particles such as hockey sticks, L-shaped and zigzags, the particles should be straightened up such that their major axis is kept consistent with the layer direction (Figure 6.17(a)); otherwise, the resulting rods, though aligning with their nearest neighbors, do not exhibit any long range ordering (Figure 6.17(b)). Reversible reconfigurations are also found for the shape shifting between convex and non-convex shapes, for example, between square and Y-shapes, between hockey sticks and zigzags, and between pentagons and crosses. The reconfigurability between ordered structures hence enables us to perform multi-step shape shifting based upon current experimental capabilities. For example, if the rods cannot be transformed into zigzags directly, we can first transform the rods into hockey sticks, resulting in a biaxial smectic structure as shown in Figure 6.15(c, middle). Subsequently, the hockey

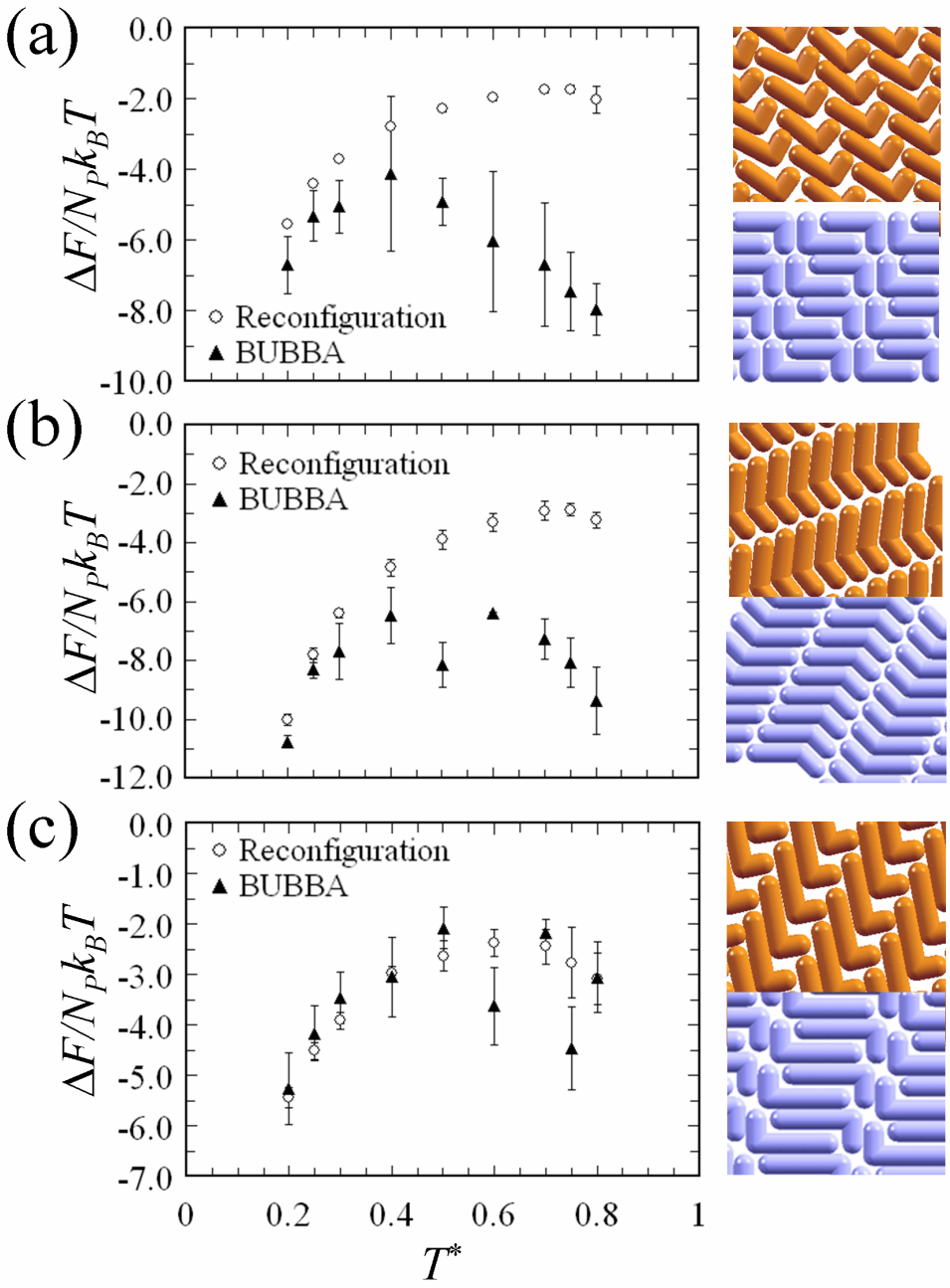

Figure 6.16 Excess free energy of the reconfigured structures (top right) versus energy minimizing structures (bottom right) with respect to the reference Einstein crystals. Error bars are obtained after five independent samples. In each sample, the excess free energy is averaged over 20 uncorrelated snapshots. (a) L4; (b) H4 and (c) L5 shapes.

sticks are bent at the longer end, turning into zigzags, which now form the ordered structure as expected (Figure 6.17(c, right)).

The shape shifting can either alter the close-packed packing pattern or toggle between a close-packed and a porous configuration, which might yield bulk materials with interesting optical and mechanical properties. As spheres grow into squares and cross-shaped particles, the initial triangular lattice is switched to a P1 symmetry lattice and rectangular lattice, respectively (Figure 6.11(a) and (d)). The P_2 symmetry packing is replaced by a rhombic packing when rods are transformed to hockey sticks and L-shaped particles; and the patterns simultaneously turn from uniaxial to biaxial smectic. Figure 6.17(d) shows the pattern reconfiguration occurring in an example of shape shifting in series: rods-squares-Y-shaped particles Y4-spheres. The reconfiguration from a close-packed to a porous morphology can be induced by adjusting the particle aspect ratio. For example, consider the structures formed by Y-shaped particles with different branch lengths (Figure 6.17(e)): as the branches are shortened or expanded, the resulting structures become close-packed or porous, respectively, reminiscent of the opening and closing of a membrane. Unlike the porosity observed with L-shaped particles L5 (Figure 6.15(f)), which is caused by the particle bumpiness, the pore size here is twice as large as a spherical bead.

Of significant practical importance, we find that the time required for these structures to reconfigure in response to particle shape change is very short compared to the time required to assemble either structure from isotropic states. Our simulations show that after the shape shifting finishes, the order-order reconfiguration completes within 5×10^6 time steps, remarkably faster than the relaxation time required for self-assembly from disordered states, which is on the order of $\approx 50 \times 10^6$ time steps. Analogous phenomena could account for the short timescales of some biological assemblies, in which proteins adopt different conformations depending on their local environment. More complicated pathways can be further envisioned by shifting into shapes that easily form ordered structures, e.g. spheres and Y-shaped particles, connecting several ordered structures. In parallel with this work, we have proposed a novel methodology to design assembly pathways to increase the self-assembly propensity of strongly interacting building blocks[31]. This methodology can serve to guide the multi-step, shape-changing induced reconfigurations en route to engineering pathways to functional nanostructures.

Shape-shifting induced reconfiguration: a kinetics-dependent process

It is important to address three crucial factors that help determine the formation of target structures in most studied cases; the initial ordered structures, the pathway towards a target

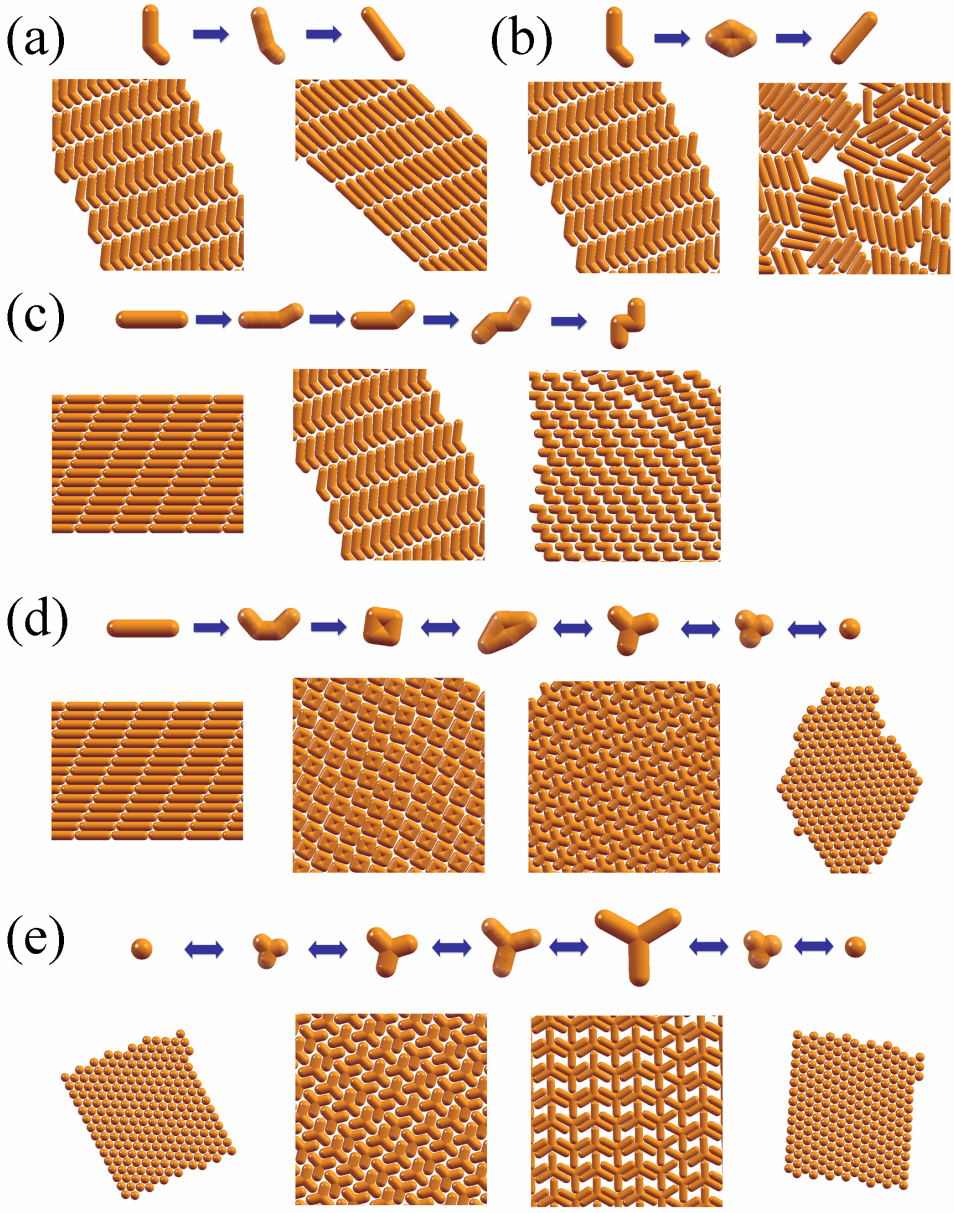

Figure 6.17 Reconfigurability between ordered structures in sequence: (a) ordered structure obtained when zigzags Z4 are straightened into rods; (b) disordered structure obtained when zigzags Z4 morph into rods through a convex shape; (c) a multi-step shape-changing transformation from rod-hockey-zigzag Z4; (d) switching between packing patterns in the sequence of rod-square-Y-shaped Y4-sphere transformations; and (e) reversible structural morphology change as a opening-closing effect between sphere-Y-shaped Y7 particle with different branch lengths; The shape shifting pathways are illustrated by snapshots of intermediate shapes from left to right. The arrows indicate shape shifting directions.

shape and the transformation rate. The initial ordered structures, such as a triangular lattice of spheres or a smectic structure of rods, play a very important role in the ordering of final structures. Unlike self-assembly from isotropic states, the evolution of the system is biased towards the target structures by the initial configurations of original building blocks. The crystalline ordering of spheres and rods, which includes the lattice spacing and directionality, helps guide the packing of transformed particles. For example, the smectic layers of rods allow the transformed hockey sticks and L-shaped particles to easily pack with adjacent neighbors, leading to biaxial smectic phases (Figure 6.11(f), Figure 6.14(e-f)); meanwhile, those grown from spheres do not exhibit any long range ordering. When Y-shaped particles are grown from spheres in a triangular lattice, their three branches are favored to nest with those coming from their six nearest neighbors to form the target configuration (Figure 6.14(d)). Since spheres and rods always self-assemble into a triangular lattice and a smectic-like structure, respectively, on a flat surface, we suppose that these two ordered structures are good candidates as starting points for shape-shifting processes.

The second factor comes from the pathway to transform a particle into a non-convex target shape. Although in principle, there are various ways to transform a particle shape into one another; our results indicate that the pathway should be judiciously and intentionally chosen in order to achieve a long range ordering in the target structure. Specifically, their orientation relative to neighboring particles should be consistent with the local packing of the target structure during transformation. Pathways that do not satisfy this condition often give rise to structures with a shorter range ordering, or disordered structures (Figure 6.15(a-b)). For example, in order to form the ordered structure with zigzags (Figure 6.15(a-b)) the rods should be simultaneously bent at two ends in opposite directions to maintain layering. If it is impossible to induce such a direct transformation between two shapes, a pathway can be constructed by carrying out multi-step shape transformations as mentioned earlier (cf. Figure 6.17(c)).

The third important factor is the transformation rate, which can affect the long range ordering of non-convex target particles. If the particle transformation time is comparable to the system's relaxation time, the influence of the initial ordered structures is significantly reduced. The system evolves in the same manner as the self-assembly of target particles. If the transformation rate is too fast, the target particles form locally ordered clusters with their neighbors, but the clusters are disordered because the energy required to re-arrange them into a longer range ordering is much greater than thermal fluctuations. We observed that the transformation rate less than $10^{-4}\sigma$ per time step were required to form the ordered structure of Y-shaped particles from rods. For faster rates, the number of defects in the resulted structures increases and the correlation length decreases remarkably.

The significance of these three factors demonstrates that the shape shifting induced transformation is highly kinetics-dependent and is thus a non-equilibrium process. Though the resulting structures may be either energy minimizing or kinetically trapped, the configurations generated via shape shifting are more predictable and reproducible provided that the shape transformation pathways are well controlled. For convex target particles such as squares, rhombuses and pentagons, the dependence of resulting structures on the transformation rates and pathways are less significant. This is due to the fact that the convex geometry favors the tiling of space, and hence the particles have a close-packed configuration. In these cases, the quality of the initial ordered structure play an important role in stabilizing a long range ordering in the close-packed configuration.

6.2.4 Conclusion

Although the shape of particles plays a key role in determining the formation of, and the local packing in assembled structures, only recently has the possibility to dynamically change the shape of particles on timescales much shorter than required for self-assembly. We proposed a framework to investigate the effects of particle shape shifting on the self-assembly and reconfigurability of resulting structures. The particle model used in this study is a basic model for a large number of shape-changing nanoparticles, colloids, gel-based particles, peptides and other stimuli-responsive building blocks. By shifting the particle shape dynamically, one can induce reconfiguration between ordered structures. The resulting structures have longer range ordering, and with shorter relaxation time compared to those attained through traditional self-assembly. The initial ordered configuration of rods and spheres, the transformation pathway, and rate are shown to be critical to the order-order transition in most studied cases. We further showed that, in principle, a pathway to a desired ordered structure, given an initial ordered structure, can be constructed by performing a series of shape changing steps; such methods can be used to engineer pathways to previously inaccessible regions of phase space. The reconfigurability of assembled structures in our model, mimicking that of biological systems, serves to inspire novel approaches to the fabrication of next-generation functional nanomaterials. Despite the simple shape change considered here, the simulation model and methodology are applicable to more interesting shape changes in 3D, which are the focus of our future study.

6.3 Directed assembly of magnetic Janus particles

In the previous sections, we showed that the reconfigurability of assembled structures can be induced by toggling the solvent selectivity or by shifting the building block geometry. After such an abrupt change, the building blocks continue self-assembling as governed by thermodynamic driving forces. Here we focus on reconfigurable structures obtained via assembly directed by an external potential. We demonstrate that magnetic Janus particles with an off-center magnetic dipole moment in a gradient magnetic field assemble into a two-dimensional lattice whose local density can be tuned by the transverse gradient and particle magnetic dipole strengths. We find that the Janus particles align their magnetic compartment towards the strong-field region. This gradient induced alignment, caused by the asymmetry of the Janus particles, allows for the structure to reconfigure in response to changes in the field direction. This work is a collaboration with the Lahann group at the University of Michigan, and will be reported in Reference [229].

6.3.1 Introduction

Biphasic colloidal particles, often called Janus particles, have attracted a significant attention over the last decade due to their potential applications in photonic materials[191], emulsion stabilization[230], and imaging probes[7]. These exotic building blocks represent another dimension of anisotropy by which the particle surface is patterned with two separate chemically distinct regions, for example, hydrophilic-hydrophobic, magnetic-nonmagnetic, or metallic-polymeric. Depending on the chemistry and geometry of these domains, the interaction between the particles may become highly directional, giving rise to novel structures such as staggered chains[231, 232], FCC and BCC crystals, diamond-like networks[233], kagome lattices[234], which are often only observed at atomic or molecular scales. In addition to an enormous body of experimental studies, numerous computational efforts have been made to get further insights into the aggregation behavior of the Janus particles as well as to control over their assembly process towards target motifs or complicated structures[15, 27, 28, 155, 235–237].

There are two popular approaches to synthesizing Janus particles: indirect surface modification and direct dual-supplied droplet formation. The indirect methods often involve three stages: first, the particles are deposited onto a planar substrate or a spherical interface of a wax (oil)-water emulsion. to mask one hemisphere; second, the unmasked hemisphere is put under a chemical or physical treatment; finally, the particles are released from the substrate (or interface)[238, 239]. The resulting Janus particles are mostly spherical in

shape due to the surface free energy minimization occurring in the first step. The direct method requires the combination of two parallel coflowing streams of polymeric solutions in microfluidic devices[232], electrified jetting[7, 9], or spinning disks[230]. The shape of the Janus particles produced by these methods can be controlled by the flow rates or channel geometry. Additionally, it has been shown that direct methods allow for loading additional materials such as fluorophores, dyes, nanoparticles, cells, or colloids into one of particle hemispheres, giving rise to multifunctional Janus particles. For example, using a microfluidic device, Yuet et al. synthesized superparamagnetic Janus particles with nonmagnetic poly(ethylene glycol)-diacrylate (PEG-DA) solution in one hemisphere, and PEG-DA with Fe_3O_4 in the other. Using electrohydrodynamic co-jetting, Lim and coworkers have shown that by putting gold nanocrystals[9] into one of two streams, they can make micrometer-sized Janus particles with only one hemisphere conductive. Other successful approaches to synthesize have also been reported, for example, via the reaction-induced phase separation of two materials, surfactant microphase separations, or selective crosslinking from bulk self-assembled morphologies[240]. Detailed reviews on the synthesis and assembly of Janus particles can be found elsewhere[238, 240].

With the ability to fill the Janus compartments with a wide range of materials, it is natural to imagine that these particles can be manipulated via external stimuli such as light, electric field or magnetic field. The directed assembly and switchability of the Janus particles are of significant interest in biological applications. Smoukov et al. demonstrated that the assembly of magnetic Janus particles made by a polystyrene sphere coated with a thin iron film on one hemisphere can be directed by a magnetic or an AC electric field[231]. The particles aggregate into linear chains so that the magnetic hemispheres from adjacent particles touch each other forming a metallic stripe in the middle of the chain. Depending on the magnetic dipole moment of the particles, which increases with the thickness of the metallic layer, non-magnetic parts from one side of the chain can touch or stay far apart, resulting in a double chain or a staggered chain, respectively. Yuet and coworkers showed that the Janus particles occupy a triangular lattice under a uniform magnetic field perpendicular to the substrate, and form chainlike structures as the field is applied in-plane with the substrate[232]. The morphology of the chainlike structures depends on the coverage fraction of the magnetic hemisphere. Recently, Lahann group have shown that by magnetic micron-sized Janus particles can be synthesized with one compartment containing magnetite (Fe_3O_4) nanoparticles. Upon application of a spatially variant magnetic field perpendicular to the substrate, the particles become magnetized and assemble into two-dimensional ordered structures with a highly uniform alignment of the magnetic hemispheres. This alignment allow for a switching behavior of the assembled structure in response to a change in the field direction.

Furthermore, the particle density is spatially variable and can be tuned by changing the gradient strength. This tunable density gradient suggests potential applications in optical cloaking materials if the particle size can be scaled down to several hundreds of nanometers. Here we have performed computer simulations to understand the role of the field gradient and the particle magnetic dipole moments in achieving control over the particle alignment and density.

6.3.2 Model and simulation method

Model

To study the directed assembly of the poly(lactic-co-glycolic acid) (PLGA) Janus particles we develop a coarse-grained model as shown in Figure 6.18. The green-red sphere represents the excluded volume of the whole particle. We assume that the magnetite nanocrystals are homogeneously distributed in the red hemisphere, thus the induced dipole moment is located at the center of mass of the red hemisphere; and the distance between the particle center of mass and the dipole vector (blue) is 0.1875σ where σ is the particle diameter.

Figure 6.18 Model magnetic Janus particle. The red hemisphere represents the magnetic compartment containing magnetite nanoparticles. Left: Side view. The blue arrow indicates the induced magnetic dipole **m** not coincident with the particle center and aligning with the field vector. Right: Top view. The orientation vector **u** is in the x-y plane and perpendicular to the field vector.

The micron-sized particles are subject to (1) excluded volume interactions, (2) dipole-dipole interactions, (3) magnetic field, and (4) friction. Unlike in equilibrium self-assembly, the dynamics of the system in the presence of an external field plays a vital role in the formation of assembled structures. We match the order of magnitude of relevant forces so that the dynamics in our model is consistent with that in experiments.

The excluded volume interaction between red-green spheres is modeled by the Weeks-

Chandler-Andersen potential, which is commonly used for modeling colloidal particles:

$$U_{WCA}(r) = 4\varepsilon\left[\left(\frac{\sigma}{r}\right)^{12} - \left(\frac{\sigma}{r}\right)^{6}\right] + \varepsilon \tag{6.4}$$

for the inter-particle distance within $r_{cutoff-WCA} = 2^{1/6}\sigma$. The energy strength ε is chosen so that the strongest magnetic force does not cause overlapping between particles under a strong field.

The dipole interaction between blue sites is given by:

$$U_m(r) = -\frac{\mu_0}{4\pi r^3}\left[3(\mu_i \cdot \hat{\mathbf{r}})(\mu_j \cdot \hat{\mathbf{r}}) - \mu_i \cdot \mu_j\right] \tag{6.5}$$

where $\hat{\mathbf{r}} = \mathbf{r}/\sqrt{\mathbf{r}\cdot\mathbf{r}}$ is the unit vector pointing from particle i to particle j. The dimensionless induced magnetic dipole is defined as $m = \mu k/\sqrt{\sigma^3 \mu B}$ with k being some scaling factor. From the magnetization hysteresis of PLGA particles, the particle dipole is in the order of $10 \times 10^{-3}\text{emu/cm}^3 \times \pi(20 \times 10^{-5}m)^3 = 10^{-14}\text{Am}^2$. Since the strength of the applied gradient field is in the order of $B = 10^{-2}\text{T}$, the field energy associated with the particle assembly is $\mu B = 10^{14}\text{Am}^2 \times 10^{-2}\text{T} = 10^{-15}\text{J}$, much greater than the thermal energy $k_B T$, i.e. $T^* = k_B T/\mu B = 1.38 \times 10 - 23\text{J/K} \times 298\text{K}/10^{-15}\text{J} = 10^{-6}$. Note: $B = \mu_0 H = 10^{-2}\text{A/m} = 10^{-2} \times 4\pi \times 10^{-3}\text{Oe}$, then $H = 4\pi \times 10^{-5}/4\pi \times 10^{-7} = 100\text{Oe}$. Therefore, we choose μB to be the energy scale instead of $k_B T$. The force between two parallel dipoles separated by a distance of σ is given by:

$$F_d(m_i, m_j, r) = \frac{3\sigma^4}{r^4} m_i m_j \frac{k^2 \mu_0 \mu B}{4\pi\sigma} \tag{6.6}$$

where $f = k^2\mu_0\mu B/(4\pi\sigma)$ is defined as the force scale. The time scale is then defined as:

$$\tau = \sqrt{M\sigma/f} = \sigma\frac{4\pi M}{k^2\mu_0\mu B} \tag{6.7}$$

To be consistent in the order of magnitude, other relevant forces should be expressed in the same force scale.

The magnetic field exerts on the magnetic part of each particle an additional force:

$$F_b(\mathbf{r}_i) = -\nabla U_B(\mathbf{r}_i) = \nabla(\mu_i \cdot \mathbf{B}) \tag{6.8}$$

where $\mathbf{B} = (B_x, B_y, B_z)$ is the field magnetic vector. In this study, we assume that only B_z varies spatially $B_z(x) = B_0 + ax$; the other two components do not. Specifically, B_z decreases linearly with the distance from a particle to the wall. Using the force scale as for the

dipole-dipole interaction, it follows that the dimensionless gradient strength is defined as:

$$g_B = \frac{4\pi a}{k\mu_0}\sqrt{\frac{\sigma^5}{\mu B}} \tag{6.9}$$

The micron size particles are also subject to a significant drag force proportional to the particle velocity:

$$F_v(\mathbf{r}_i) = -\gamma \mathbf{v}_i = -3\pi\zeta\sigma\mathbf{v}_i \tag{6.10}$$

where γ is the friction coefficient and $\zeta = 10^{-3}\text{Ns/m}^2$ is the dynamic viscosity of the solvent (water) at room temperature. Using the force scale defined above, we define the dimensionless friction coefficient as:

$$\gamma_{sim} = \frac{12\pi^2\zeta\sigma^3}{k^2\mu_0\mu B} \tag{6.11}$$

The particles are restricted between two walls by a non-periodic boundary condition in the x direction. The particles interact with the walls via the purely repulsive Weeks-Chandler-Andersen potential.

Simulation method

We use molecular dynamics to simulate a system of model PLGA particles on a two-dimensional cell. The magnetic field is perpendicular to the plane and becomes stronger along the positive direction of the x axis. The particles are restricted between two non-attractive, impenetrable walls in the x direction. The periodic boundary condition is applied in y direction. To ensure that the resulted structures are robust, we perform simulations with different initial configurations and random seeds. A typical system consists of N = 100-500 particles, and is equilibrated for $5 - 10 \times 10^5$ time steps until the final structure becomes stable. The natural units of the system are the particle diameter σ, the particle mass, the particle dipole magnitude μ and the magnetic field strength B. In our simulations, the experimental data corresponds to a set of simulation parameters of $k = 10$, $m = 1 - 10$, $g_B = 10 - 100$, $\varepsilon_{WCA} = 50.0$, $\gamma_{sim} = 500.0\gamma^*$ and τ = 0.2s.

In certain cases, we also perform energy minimization to verify if the final structures are the ground states with the given values of m and g_B. For this purpose, we employ the energy minimizer for rigid bodies implemented in HOOMD-blue as mentioned in Chapter 3.

6.3.3 Results and discussion

We perform simulations in the cases where the field is uniform ($g_B = 0$) and perpendicular to the x-y plane to ascertain that our model reproduces experiment. For the cases where the gradient strength is non-zero and perpendicular to the x-y plane, our simulations reveal the alignment of the particles with respect to the wall and their local density can be controlled by varying the field gradient and their repulsion strength.

Uniform field and in-plane field

With no field gradient, the assembly of Janus particles is identical to magnetized particles previously studied in the literature[231, 239]. Our simulations are in excellent agreement with experiments, confirming that the model is sufficient to capture the behavior of the system in the presence of a uniform magnetic field. When the field is perpendicular to the x-y plane, the particles do not aggregate because their induced magnetic dipoles are all perpendicular to the plane and their interaction is purely repulsive (Figure 6.19(a)). When the field is parallel to the x-y plane, the induced magnetic dipoles are parallel to the field vector, leading to the formation of chain-like structures (Figure 6.19(b)). Because of their anisotropic geometry, the dipole vector is not coincident with the particle center of mass; the particles align in a staggered pattern so that the dipole vectors can line up.

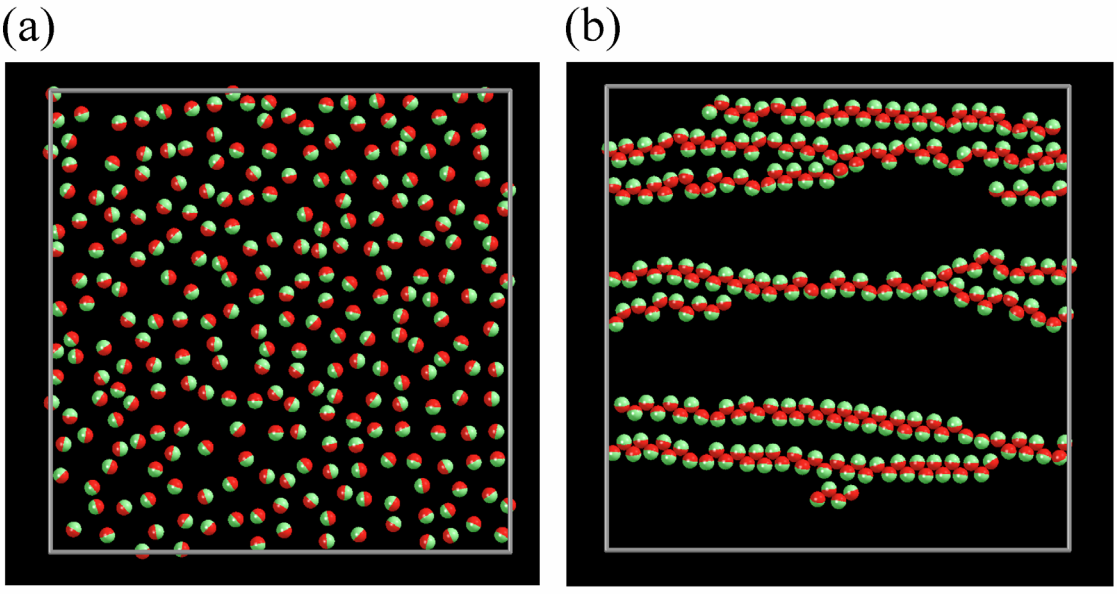

Figure 6.19 Assembled structures with a uniform field and an in-plane field. Janus particles (a) disperse when the uniform field is perpendicular to the x-y plane; or (b) form staggered chains when the uniform field is parallel to the x-y plane (right).

Gradient field

In the presence of a gradient field (nonzero g_B), our simulations also reproduce experimental findings. For small g_B, the particles are spatially disordered but tend to align facing the wall. As g_B increases, the particles start aggregating towards the wall with the magnetic hemispheres facing the wall. The particles stack into rows with their relative spacing increasing with the distance from the wall. The ability to align Janus hemispheres and to tune the particle density by just varying the gradient field has never been reported in the literature.

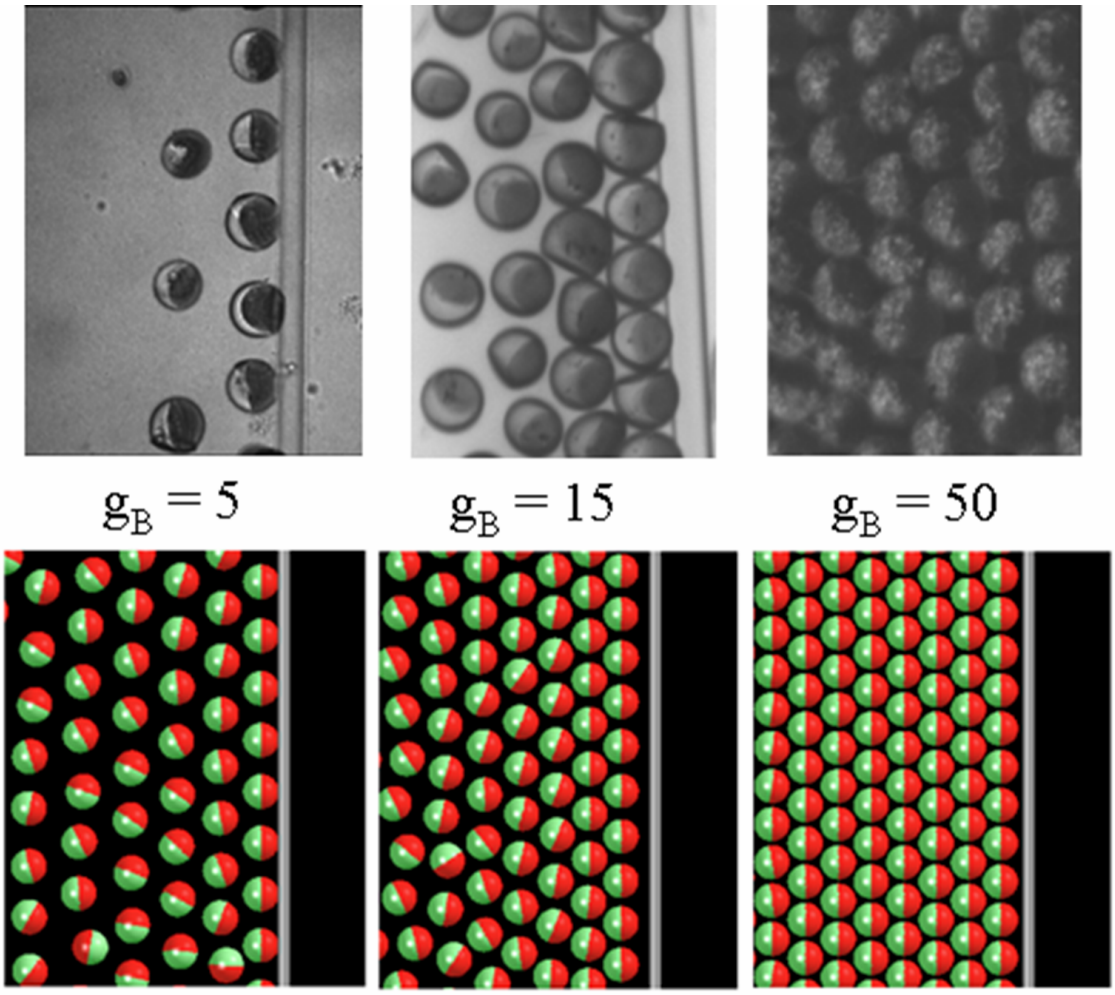

Figure 6.20 Experiment (top row) and simulation (bottom) snapshots when increasing the gradient strength g_B for m = 10. Experimental results are produced by Lahann group.

We further investigate the alignment of the magnetic hemisphere with respect to the field gradient. Let us define the alignment order parameter:

$$S = \left\langle \frac{1}{N} \sum_{i=1}^{N} \mathbf{u}_i \cdot \mathbf{x} \right\rangle \tag{6.12}$$

where $\mathbf{u}_i$ is the unit vector characterizing the particle orientation (Figure 6.18, right), $\mathbf{x}$ is the unit vector of the x axis and the average is performed over independent runs. S varies from zero to unity, corresponding to a random distribution of the alignment vector to a perfect alignment, respectively. Figure 6.21(a) shows the dependence of S on the gradient strength (g_B) and the repulsion between the particles (m). For small values of g_B and large values of m, $S < 0.6$ with a substantial fluctuation indicates that the particles exhibit a poor alignment, and that the resulting structures are uncorrelated from run to run. It is reasonable to expect that the higher g_B the better the particles align with the gradient field. However, as m increases, the value of g_B required to align the particles also increases. We should note that if g_B is too big relative to m, the kinetic effects due to the large magnetic force will cause a significant decrease in the alignment order parameter; the energy minimizing structures are kinetically inaccessible in this regime.

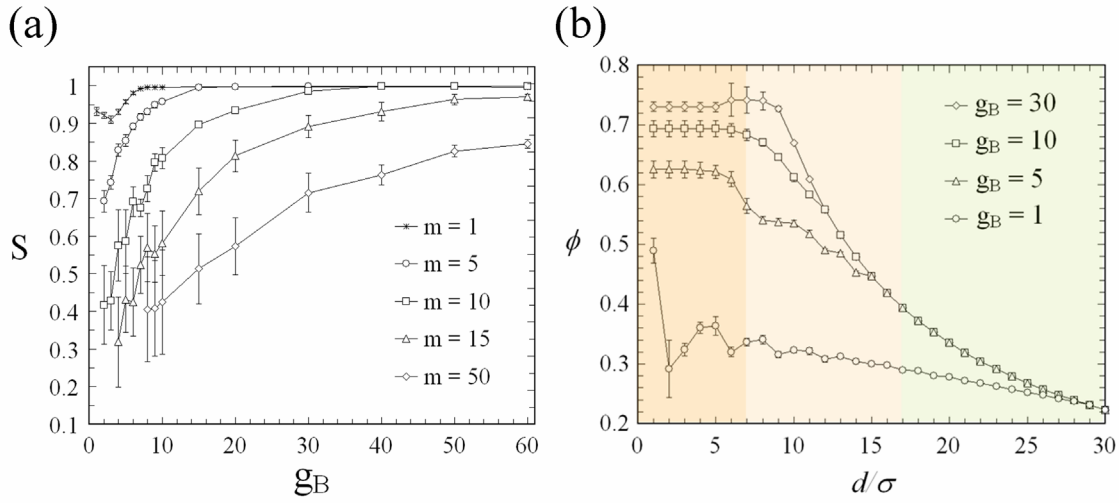

Figure 6.21 (a) Alignment order parameter S as a function of gradient strength (g_B) for different values of dipole repulsion (m). Error bars are obtained from 12 independent runs. (b) Density profile for different values of gradient strength (g_B) where d is the distance from the right wall. The curves correspond to the state points from the curve of $m = 10$ in (a). Error bars are obtained from 10 independent runs. The boundaries are sketched to help the eye.

The local density of the particles as a function of the distance from the wall is shown in Figure 6.21(b). Depending on the gradient strength, the particle density varies differently from the wall. For small g_B, the particle density is relatively homogeneous except for the first row. As g_B increases, the density profile exhibits three distinct regions as color coded in Figure 6.21(b). The dark region on the left corresponds to the region where the gradient field dominates the packing of the particles, leading to a plateau particle density. The intermediate region is where the competition between the gradient strength and particle repulsion strength leads to a gradient particle density. The green region on the right corresponds to the region

where the gradient field becomes weaker than the strong dipole-dipole repulsion. In this low-field region, the particles are located at the vertices of a regular triangular lattice. As shown in Figure 6.21(b), as we increase g_B, the flat region is broadened and shifted to higher densities and the slope of the particle density in the intermediate region becomes steeper.

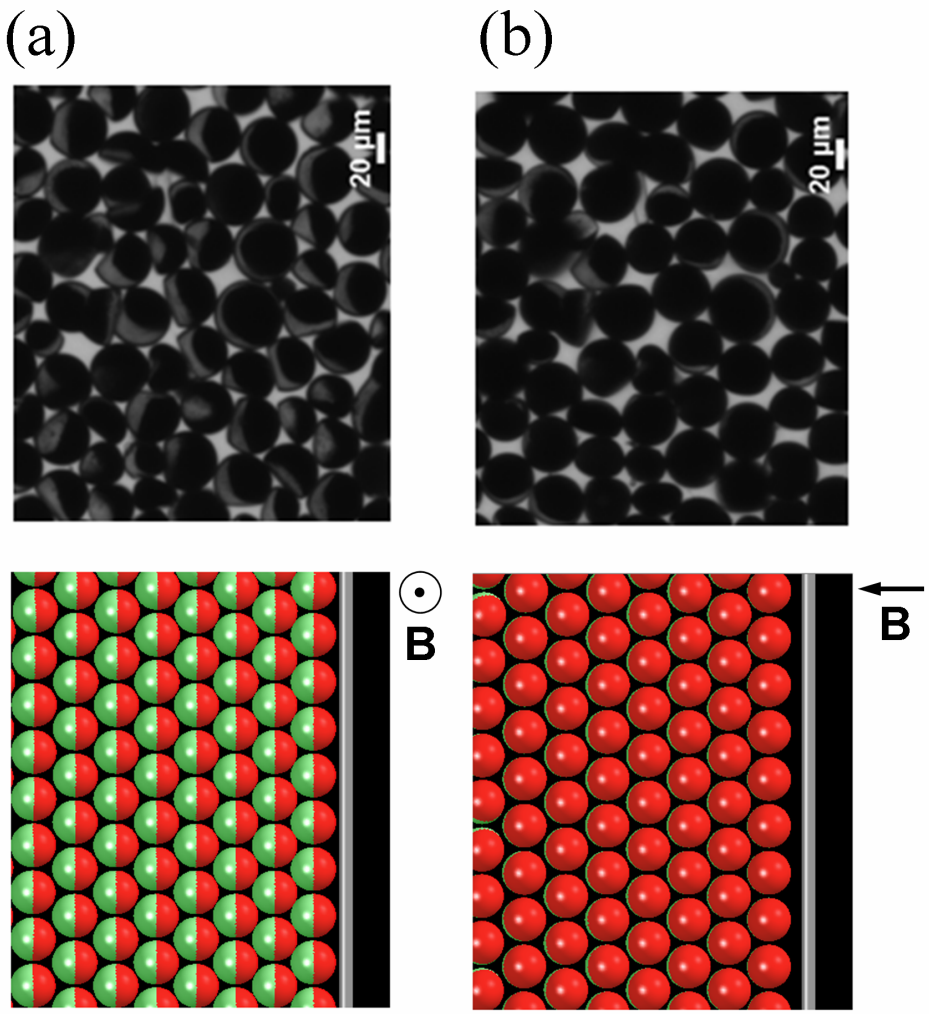

Figure 6.22 Reconfigurability of assembled structures. (a) The gradient field is perpendicular to the x-y plane. (b) The gradient field is rotated vector 90 degrees after the particles form a close packing assembly in (a). The magnetic hemispheres facing inward the plane.

Coupled with the alignment of the magnetic hemispheres, the tunable gradient density of the particles in the intermediate region can be used as metamaterials, which possess interesting cloaking properties depending on the particle size. It follows that if the gradient is radial from a point source, the particle density will vary radially from the point source. Since the aligning particles consist of two materials with different permittivity and permeability constants, it is likely that the structure would exhibit properties that are unattainable for assemblies of isotropic particles.

The assembled structure in which the particles are well-aligned can be reconfigured by changing the field direction. Figure 6.22(a) shows the initial assembled structure with the field perpendicular to the x-y plane ($g_B = 10$, $m = 5$). When the field vector **B** is rotated 90 degrees, the particles all rotate so that the induced magnetic dipoles align with the field. As a result, the whole structure switches to another state and remains stable during the rest of the simulation (10×10^6 time steps) (Figure 6.22(b)). We note that this is not the ground state with the in-plane field but rather a metastable state, kinetically favored by the initial configuration and the gradient field. (The ground state of the in-plane field is the staggered chains in Figure 6.19(b)). In our simulation, with a step change in the direction of **B**, the system completes the switching almost immediately in the order of 100 steps.

Beyond Janus particles

We extend our model (Figure 6.18) to study two possible biphasic particles that can be synthesized via electrohydrodynamic co-jetting with different flow channel geometries: quarter and di-quarter biphasic particles. The former is made with a quarter-sphere is loaded with magnetite particles, the latter with two separate quarters between two non-magnetic compartments. These biphasic particles can be synthesized via the electric co-jetting method[9]. As before, we argue that the induced dipole moment vector(s) are located at the center of mass of each quarter and parallel to the field direction. For this argument to be valid, two magnetic quarters of the di-quarter biphasic particles should be totally separate from each other. We follow the simulation procedure mentioned above and observe the assembled structures as shown in Figure 6.23.

Preliminary experiments on quarter biphasic particles show the agreement with our simulation results at low density. The particles are pulled towards the high field region with the magnetic quarter facing the wall in a similar way to biphasic particles. As a result, our simulations predict that quarter biphasic particles assemble into structures similar to that of Janus particles (Figure 6.23(a)). The alignment order parameter and particle density behave in a similar way to Janus particles because the difference between these two types of particles is only the distance from the dipole vector to the particle center of mass, i.e. 0.265σ versus 0.1875σ. The results are in agreement with preliminary experiments, once again confirming that our model is applicable to simulate this class of biphasic particles. Meanwhile, since the di-quarter biphasic particles possess two induced dipole vectors each locating in a quarter-sphere, the assembly is more strongly influenced by the repulsion between these dipoles (Figure 6.23(b)) especially when the particles closely pack. The final structure results from the interplay between the magnetic force, the repulsion between the

dipole pairs, and the spherical geometry of the particles. While the magnetic force aligns the particles in the first row and pulls all particles towards to wall, the repulsion between the particles caused by closely located dipole pairs influences the packing of the next rows.

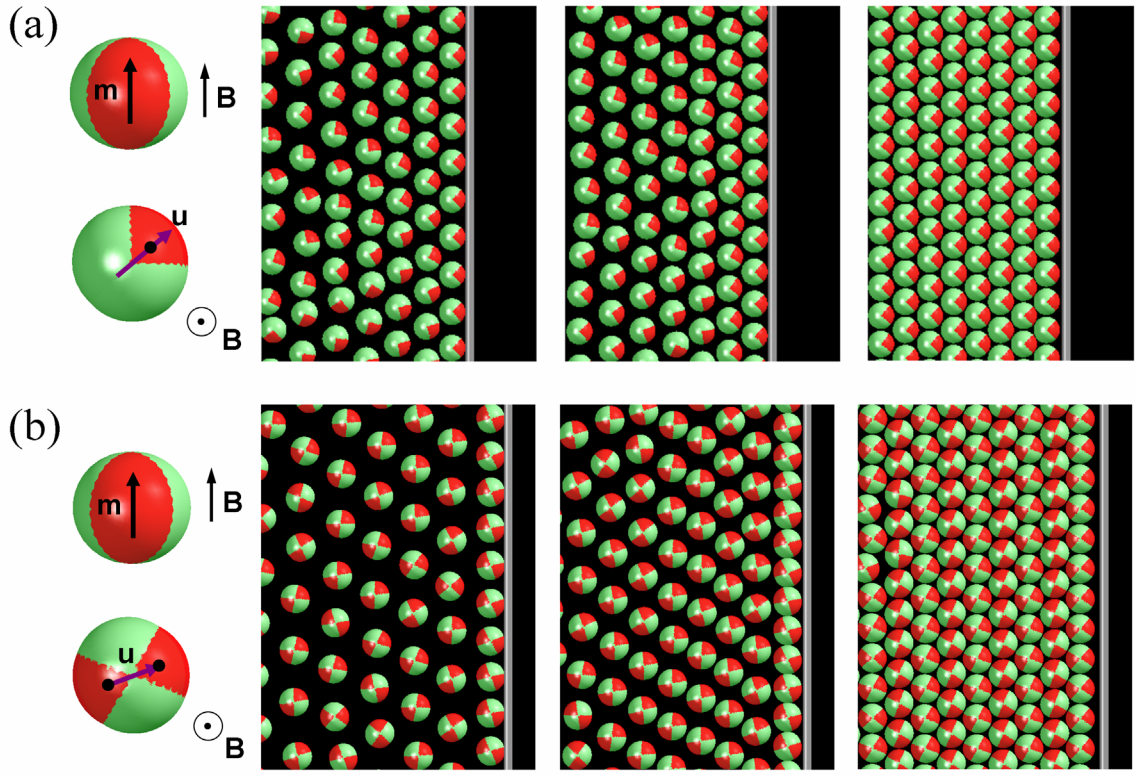

Figure 6.23 Assemblies of (a) quarter biphasic particles and (b) di-quarter biphasic particles using a similar simulation model. The model particle for each case is depicted on the left with m being the dipole vector(s), u being the orientation unit vector. The black dots are the location of the dipole vector(s).

For small values of the gradient strength the particles disperse and there is no orientational ordering (Figure 6.23(b, left)). As the gradient strength increases, the particles are closer to the wall and repel each other stronger. Within each row the particles ”tilt” to minimize the potential energy between the dipole pairs. When the particles do not touch (Figure 6.23(b, middle)), they tend to align in the same direction to maximize their orientational entropy, a behavior similar to a system of repulsive rods at high pressure. For strong gradient field the particles closely pack (Figure 6.23(b, right)). Interestingly, the particle orientation alternates from row to row as to both minimize the potential energy and maximize the orientational entropy. The alternating direction of the particles between rows breaks the structure's symmetry in an unexpected way. To ensure that the assembled structures are at local energy minima, we performed additional energy minimization on these selected cases, and observed a good agreement with simulation results.

6.3.4 Conclusion

The most striking finding of this study is that by using a simple ”knob”, a gradient magnetic field, we can tune the orientational order and density profile of magnetic Janus particle assemblies. While a non-uniform density can be expected when applying a gradient field to magnetic particles, the unique anisotropy of biphasic particles allows a symmetry breaking process that is not available for homogeneous particles in previous studies. We have shown the Janus particles exhibit a uniform alignment of the magnetic hemispheres towards the strong field region with a sufficient gradient strength compared to their magnetization. The particle density can be further tuned by varying the gradient strength and particle magnetic dipole moments. Once the particles align, they can be rotated with the field direction, allowing for interesting switching effects that are unatttainable without the initial alignment. Our minimal model can not only reproduce and extrapolate experimental results but also is applicable to other multi-compartmental colloidal particles.

Chapter 7
Conclusion and outlook

7.1 Conclusion

Our ambitious goal is to develop a generic and systematic design framework for engineering functional nanostructures via bottom-up approaches such as self- and directed-assembly. Although such a framework is far from being achieved we believe that the findings from this thesis positively contribute to its future realization. Equally importantly, through our studies we are convinced that computer simulation, in favor of experiment and theory, can be utilized as a powerful designing tool, providing not only further insights into the nature of various assembling processes in reality, but also guidance to the fabrication of desirable target structures.

Our primary focus is on soft matter building blocks such as polymer-tethered nanoparticles, nanoparticles and colloidal particles, which themselves possess many interesting optical and mechanical properties. Even more interesting is that they are able to spontaneously assemble into ordered structures under suitable conditions. These conditions include thermodynamic parameters (i.e. temperature, density and pressure), building block geometry, composition and polydispersity, interactions between building blocks and applied field. Specifically, we showed that V-shaped particles assemble into structures with a local packing of the particles completely different from those formed with tethered nanorods. The number and attachment location of the tethers also substantially alter the phase behavior of the particles. End tethered V-shaped particles form a chiral smectic phase, reminiscent of that by bent-core molecules, which was not observed for tethered rod systems (Section 4.1).

The vital role of the effective interactions between assembling building blocks in the formation of final structures is demonstrated throughout this thesis. We showed that the balance between van der Waals attraction and Coulombic repulsion limits the particle aggregation, a mechanism generic for nanoparticles made from various materials as well as proteins (Section 4.2). The mechanism helps obtain supraparticles or assemblies with a uniform geometry without rigorous efforts in building block preparation. We have developed

a spatially dependent electrostatic interaction to incorporate the many-body effects into the pair-wise interaction between the particles. This extended interaction allowed us to explain the self-limiting aggregation, which cannot be reproduced by previous models. Another intriguing finding from our simulations is that a remarkable particle size polydispersity (i.e. 20-30%) in fact helps stabilize a core-shell morphology of the spherical supraparticles.

Examples of how effective interactions between building blocks influence the morphology of assembled structures were also discussed when we investigated the hierarchical assembly of laterally tethered rods (Chapter 5). We found that a bilayer sheet pre-assembled by tethered rods relaxed at constant temperature and pressure folds into spiral scrolls (5.1) and helical structures (5.2) depending on the local packing pattern of the rods within the sheet, which is governed by the bulkiness of the tethers. The helices and scrolls are able to adopt different morphologies upon changes in the effective interaction between the rods and the tethers. While the emergence of helical structures and spiral scrolls from inorganic materials is fascinating by itself, we would emphasize the possibility of engineering target structures from reconfiguring certain pre-assembled structures by varying the environmental condition, e.g. by means of pH, salt concentration or light density.

The reconfigurability of assembled structures was investigated in depth in Chapter 6. We modeled an abrupt change in the rod aspect ratio, finding that the square grid structure formed by the short rods can transform into a bilayer sheet when the rods are lengthened, and vice versa (Section 6.1). The transformation process is remarkably faster than self-assembly due to the presence of the bilayer ribbons, a favorable motif common to both structures. The idea of shape-shifting particles is further extended in Section 6.2. We demonstrated that by judiciously shifting the particle geometry we can transform initially ordered structures into various unique structures that are inaccessible otherwise. Of practical importance with regards to engineering functional structures is the possibility to concatenate reversible transformations into robust pathways that connect an easily obtained structure to any specific target structures.

An alternative to achieve structural reconfigurability is to couple building block anisotropy with the application of an external potential. We showed that the directed assembly of biphasic particles in the presence of a gradient magnetic field (Section 6.3). The unique anisotropy of biphasic particles such as Janus particles, quarter and di-quarter particles results in the symmetry breaking of assembled structures as the magnetic compartments are aligned and pulled towards the high-field region. Using a single parameter, i.e. the field gradient strength, we can tune the particle alignment and gradient density simultaneously. Interestingly, we showed that the aligning particles are able to adapt quickly in response to the change in the field direction, mimicking a switching effect that would not be present

without the driving gradient.

Finally, we implemented rigid body dynamics and energy minimization into HOOMD-blue (see Chapter 3), an open-source general purpose molecular dynamics (MD) package on graphics processing units (GPUs) hosted by Glotzer's group. The performance of the GPU version reaches approximately 2000 time steps per second for a system consisting of 60000 atoms, a typical system size for our studies. This is roughly 3 times faster than LAMMPS run on 64 Intel® Xeon® E5540 CPU cores. To our knowledge, the energy minimizer for rigid bodies is the first implemented and available in an open-source MD code.

7.2 Outlook

The inspiring results with various soft matter systems suggest various promising directions towards the design and fabrication of functional nanostructures. In addition to traditional approaches include tailoring building block anisotropy in terms of shape, composition, interaction specificity and directionality, and varying thermodynamic variables (e.g. temperature, pressure and density), we have introduced as proofs of concept a number of promising approaches including self-limiting aggregation, structural transformation via shape shifting particles and hierarchical assembly. There remain many interesting yet challenging problems needing to be investigated so that these approaches become worth pursuing by experiments and are theoretically reliable. In particular, our future work will be devoted to address several topics as follows.

7.2.1 Directional self-limiting aggregation

As mentioned in Section 4.2, the self-limiting aggregation occurs due to the balance between attractive and repulsive forces between assembling building blocks. Key to this process is that the repulsive force should increase monotonically with the aggregate size to prevent further aggregation at the terminal size. We hypothesize that if the repulsive force is directional, for example, charge-dipole and dipole-dipole interactions, the self-limiting aggregation will result in anisotropic aggregates also with a uniform geometry. If this hypothesis is true, we can explain the formation of various uniform shape assemblies, for example, the twisted ribbons with a fixed width formed by CdTe tetrahedra in the work of Srivastava et al.[14] or a bilayer sheet of CdSe tetradedra in the work of Tang et al.[24] Furthermore, we can generalize self-limiting aggregation as a generic recipe for synthesizing monodisperse terminal nanostructures.

7.2.2 Pathway search for shape-shifting particles

In Section 6.2, we demonstrated that by shifting the particle shape following specific pathways we can transform an ordered structure to one another. One of the most challenging issues is to find robust pathways that ensure the formation of the target structure with a tolerable amount of defects. Since the similarity of a given structure to a reference structure can be quantified by a shape-matching order parameter, we can state the problem in the optimization perspective: to find shape-shifting pathways that maximize the shape-matching order parameter of the final structure with respect to a reference structure. Or in other words, the shape matching order parameter can be regarded as a ”potential” and the search for the pathways corresponds to performing an ”potential minimization” in the particle shape space. In this context, the ”trajectories” would correspond to the desired shape shifting pathways.

Assuming that the initial and final shapes and target structure are known or restricted by experimental constraints, our goal is to find intermediate shapes such that the particles in the final shape stabilize the target structure. In future work, we are going to test if the following procedure would work. First, we will use the Bottom-Up Building Block Assembly (BUBBA) algorithm[228] and our preliminary results in Section 6.2 to narrow the search space down to a small number of promising intermediate shapes. For each intermediate shape, we find thermodynamically stable assembled structures, i.e. intermediate structures, via self-assembly simulations and energy minimization. Subsequently, we sample an ensemble of shape shifting pathways that connect the initial and final structures with the stable structures formed by intermediate shapes. By sampling we mean to use the minimization scheme with the shape matching order parameter as the objective function. The desired pathway is one that gives the best match with a given reference structure. If the shape shifting transformation from two ends have at least one intermediate structure in common, this means there exists a pathway between the initial and final structures.

We note that if only the morphology of the final structure is of interest, e.g., structures with specific tiling patterns or ordered pores – BUBBA can be used to identify the target shapes that have a good assembly propensity with regards to the target structure.

7.2.3 Hierarchical assembly

As shown in Chapter 5, hierarchical assembly offers us more flexibility to achieve structures with a higher degree of complexity beyond the length scale of individual building blocks. By introducing permanent bonds to mimic the strong binding between the particles within the pre-assembled structures, we can use another (weaker) energy length scale to drive

the evolution of these structures into fascinating higher-order structures such as helical structures and spiral scrolls. In previous computational studies, it has been shown that the formation of a complicated structure, e.g. a diamond network[241] or a sigma phase[242], are often enhanced in the presence of several seeds. The work of Srivastava et al.[14] also confirmed the hierarchical assembly of ligand-coated nanoparticles into twisted helical ribbons. Another excellent example of hierarchical assembly is recently demonstrated in the work of Iacovella et al.[242] where the authors showed that micelles formed by tethered nanospheres and block copolymers assemble into quasi-crystalline superstructures. Not only are these findings reminiscent of many naturally occurring sophisticated biomolecules but also they are likely related to the mechanism of the spontaneous formation of inorganic crystalline structures with a long-range order with very few defects. A promising next step for future work would be to reason the self-assembly of several nanoparticles in different shapes into fascinating crystalline structures without kinetic traps. If successful, we believe that our results will provide further insights into the nature of these systems, and moreover, open the opportunities to fabricate sophisticated functional structures crossing multiple length scales via bottom-up approaches.